University of Padova

Department of Physics and Astronomy "Galileo Galilei"

Master Thesis in Physics of Data

Study of the energy reconstruction in Super-Kamiokande and optimization of the T2K oscillation analysis

Supervisor
Andrea Longhin
University of Padova

Master Candidate
Ema Baci

Student ID
2050726

Academic Year
2023-2024

To my beloved cat, Lily.

Abstract

The T2K experiment (Tokai to Kamioka) is a long-baseline neutrino experiment that investigates neutrino oscillations by producing a beam of muon neutrinos at the J-PARC facility in Tokai, Japan, and detecting them at the Super-Kamiokande detector, located 295 km away in Kamioka. Its primary objectives include measuring the oscillation parameters related to the disappearance of muon neutrinos and the appearance of electron neutrinos. The experiment aims to understand the fundamental properties of neutrinos, including CP violation, which may help explain the observed predominance of matter over antimatter in the universe.

In this thesis, I have studied the resolution of the Super-Kamiokande detector in the reconstructed neutrino energy and the lepton angle using simulated data employed by the T2K collaboration to measure oscillation properties.

In particular, I considered the interplay between resolution and binning and searched for possible areas of improvement.

The presence of biases has been checked as well as the relation between the bin widths and the resolution in the bins, to prevent the occurrence of undesirable large migration effects. These studies have been conducted in two dimensions, taking into account both angle and momenta. The effectiveness of the two-body formula for neutrino energy has also been verified by analyzing it in the p-θ plane in bins of the true neutrino energy.

A proposal for binning improvement is put forward and it will be checked against its effectiveness in improving the uncertainty on the fitted oscillation parameters.

Contents

Listing of figures

Listing of tables

Listing of acronyms

e ..... electron

μ ..... muon

τ ..... tau

ν_e ..... electron neutrino

ν_μ ..... muon neutrino

ν_τ ..... tau neutrino

$\bar{\nu}_e$ ..... electron antineutrino

$\bar{\nu}_\mu$ ..... muon antineutrino

$\bar{\nu}_\tau$ ..... tau antineutrino

2p2h ..... 2 particles 2 holes

CC ..... Charged Current

FHC ..... Forward Horn Current

CCQE ..... Charged Current Quasi Elastic

DIS ..... Deep Inelastic Scattering.

FGD ..... Fine Grain Detector: a subdetector of ND280, typically used as a target mass for most analyses.

FHC ..... Forward Horn Current.

FSI ..... Final State Interactions: interactions that a pion or nucleon undergoes before exiting the nucleus (e.g., a charged pion created within the nucleus may be reabsorbed and thus not detected).

GUT ..... Grand Unified Theory.

INGRID ..... Interactive Neutrino GRID: the neutrino detector located 280 m from the target on the near side, primarily designed to measure the beam center.

J-PARC ..... Japan Proton Accelerator Research Complex: the facility used to generate the T2K neutrino beam in Tokai.

K2K ..... Neutrino oscillation experiment in Japan, conducted from KEK to Kamioka.

LINAC ..... LINear ACcelerator at J-PARC.

MaCh3 ..... Markov-Chain 3: software for fitting neutrino oscillation parameters used in T2K analyses, based on a Markov Chain Monte Carlo (MCMC) method.

MC ..... Monte Carlo: a statistical method used for simulations.

MCMC ..... Markov-Chain Monte Carlo: a sampling method employed by MaCh3 to explore the allowed parameter space and obtain a posterior likelihood distribution based on observed data and a parameterization.

MPPC ..... Multi-Pixel Photon Counter: a photon detection device utilized in the T2K experiment for all scintillator detectors at the near site.

MR ..... Main Ring: the component of the J-PARC facility responsible for accelerating protons to 30 GeV.

NC ..... Neutral Current.

ND280 ..... Near Detector at 280 metres: the off-axis neutrino detector located near the target, used for near detector fits and cross-section measurements.

PØD ..... Pi-zero Detector: a detector within ND280 designed specifically for measuring neutral pions.

PID ..... Particle IDentification.

PMNS ..... Pontecorvo-Maki-Nakagawa-Sakata: refers to the matrix describing neutrino mass mixing.

PMT ..... Photo-Multiplier Tube: a device that collects Cherenkov light from the walls of Super-Kamiokande.

POT ..... Protons On Target.

p-theta ..... Neutrino oscillation parameter fitting software used for T2K oscillation analyses.

RCS ..... Rapid Cycling Synchrotron: the second stage of proton acceleration following the LINAC, which boosts protons to 3 GeV.

RES ..... Resonant: a process in which a boson interacts with a nucleon to produce a nuclear resonance.

RHC ..... Reverse Horn Current.

SK ..... Super-Kamiokande: a 22 kTon water Cherenkov detector in Japan, serving as the far detector for the T2K experiment.

SM ..... Standard Model.

SNO ..... Sudbury Neutrino Observatory.

T2K ..... Tokai to Kamioka: the neutrino oscillation experiment that is the framework for this work.

TPC ..... Time Projection Chamber: a subdetector of ND280 that provides precise particle identification (PID), charge, and momentum measurements for charged particles.

1

Neutrino Physics

Despite being the most abundant known massive particle in the universe, neutrinos pose a remarkable challenge for detection and study due to their extraordinarily small mass and lack of electric charge, which make them interact with matter only weakly. Their minimal interaction with matter entails that neutrinos preserve their direction and momentum and can therefore be exploited in the study of distant astrophysical sources. Besides, neutrinos undergo flavor oscillations during their journey, meaning they change their flavor as they propagate. This property, known as neutrino oscillation, enables the investigation of CP-violation. Neutrinos are also involved in numerous other phenomena, including cosmic ray showers and various nuclear processes. All these implications make neutrino physics a paramount field of research.

1.1 Discovery

Neutrinos are neutral fermions first predicted by Wolfgang Pauli [13] in 1930 to explain the apparent non-conservation of energy and momentum observed in beta decay, particularly due to the continuous spectrum of emitted electrons. This prediction addressed the need for a missing energy component in the decay process, which was later identified as the neutrino [14] [15] [16].

Following the theorization, the first neutrino detection took a while, mainly because, as neutrinos interact only through the weak force and have very small interaction cross sections, neutrino detectors must operate over extended periods to accumulate a statistically significant dataset or, alternatively, must have a large mass. This constraint complicates neutrino research by obscuring neutrino interactions within the effects of nuclear potentials. Therefore, for accurate predictions of neutrino behavior, nuclear theory must be considered in addition to standard quantum field theories.

The first detection occurred in the Cowan-Reines experiment on June 14, 1953, through the observation of the inverse β-decay process: $\bar{\nu}_e + p \rightarrow e^+ + n$, using the Savannah nuclear reactor anti-neutrinos on cadmium-doped water at the Savannah River Plant in South Carolina, USA [17].

The hypothesis that neutrinos were leptonic flavor-characterized was confirmed instead in 1962 with the first ever accelerator beam neutrino experiment leading to the detection of the first muonic neutrino ν_μ [18]. The same results were confirmed at CERN in 1964 [19].

The ν_τ was detected by the DONUT collaboration at Fermilab in 2000 [20], following the production of the first τ lepton in 1975, achieved using an electron-positron collider at the Stanford Linear Accelerator Center (SLAC) laboratory [21].

1.2 Neutrinos in the Standard Model

In the framework of the Standard Model (SM) of particle physics, neutrinos are fundamental particles that belong to the lepton family, together with electrons e, muons μ, and tau τ particles. There are three neutrinos, each associated with a different lepton flavor. Therefore the SM describes three generations of fermions, each consisting of a charged lepton (e, μ, or τ) and its corresponding neutrino (electron neutrino ν_e, muon neutrino ν_μ, or tau neutrino ν_τ).

Neutrinos are electrically neutral with a lepton number of +1, which makes them distinct from their antiparticles, which have a lepton number of -1.

One of the key features of neutrinos, according to the SM, is their left-handed chirality, which means they predominantly interact with left-handed particles and right-handed antiparticles. Unlike charged particles, neutrinos do not interact via

the electromagnetic force or the strong nuclear force, making the weak nuclear force their primary mode of interaction.

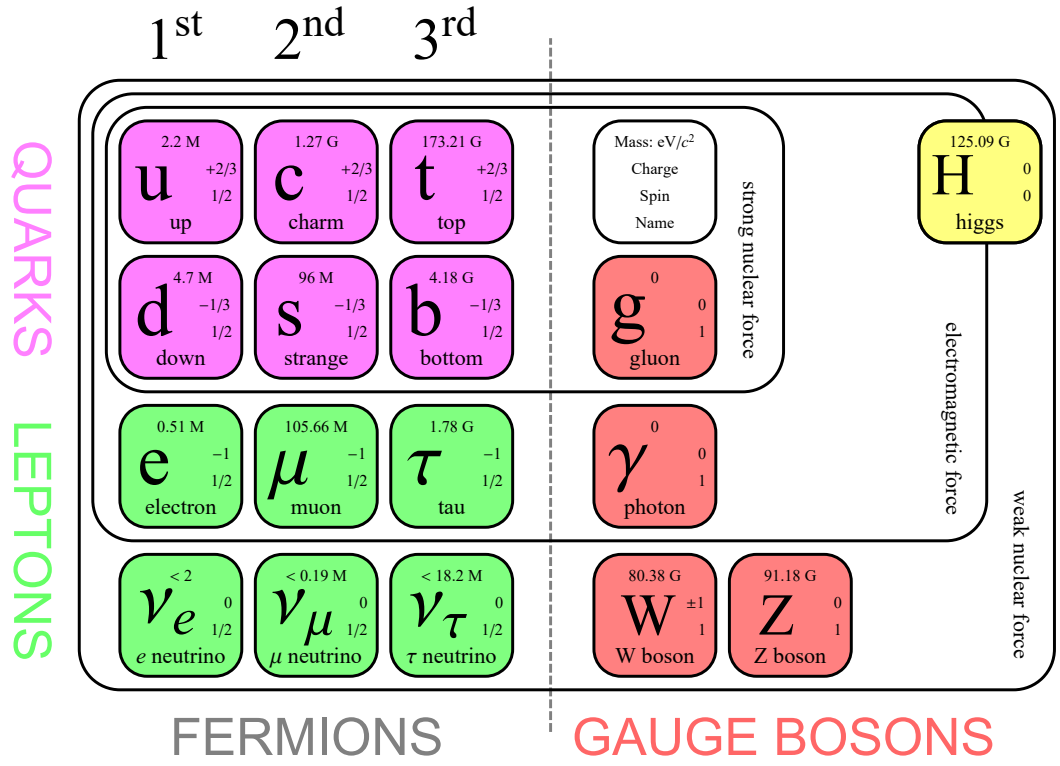

Figure 1.1: Schematic overview of the Standard Model (SM). The particles in the SM are categorized based on their interactions, flavor, charge, and spin. The spin-1/2 fermions, including quarks and leptons, come in three generations, with each generation ordered by mass (except for the neutrinos, whose masses are much smaller and still not precisely determined). The spin-1 gauge bosons, such as the photon, W and Z bosons, and gluons, mediate the electromagnetic, weak, and strong nuclear forces, respectively. Additionally, the SM includes a spin-0 scalar boson known as the Higgs boson, which mediates the coupling of the massive particles with the Higgs field, giving them their mass. Image taken from [1].

Neutrinos were initially assumed to be massless in the SM, however they were later found to have tiny but non-zero masses, as evidenced by neutrino oscillation experiments reported in Section 1.3.1.

Studying neutrino oscillations is paramount since it is a tool to understand why in the universe seems to be more matter than antimatter. This issue is called the Charge-Parity (CP) symmetry violation. In most interactions, CP-symmetry is conserved, suggesting that the universe began in a symmetric state with equal amounts of matter and antimatter. However, the observed matter dominance implies a violation of CP-symmetry. In 1966, Andrei Sakharov [22] proposed three

conditions necessary for baryogenesis, the process by which matter predominates over antimatter.

- Departure from thermal equilibrium: matter must exit thermal equilibrium with the hot plasma which existed at the beginning of the universe;
- violation of C and CP conservation: both C and CP conservation must be violated
- non-conservation of baryon number: baryon number conservation must be broken.

The CP-violation measured in the quark sector alone is insufficient to satisfy the second condition for baryogenesis.

However, if neutrinos can violate CP-conservation, and if this violation is significant, it could contribute to meeting the condition. Minimal extensions of the SM that incorporate massive neutrinos with CP-violating oscillations are prerequisites for models such as leptogenesis, which aim to explain the matter-antimatter asymmetry observed in the universe today. Furthermore, these extensions may also contribute to the development of a Grand Unified Theory (GUT), potentially contributing to the understanding of fundamental forces in the future.

1.3 Neutrino Oscillation

1.3.1 Evidences

The late 1990s marked a significant breakthrough in understanding neutrinos, as Super-Kamiokande (SK) [23] experimentally demonstrated that neutrino survival probabilities vary depending on both their flavor and the distance they travel. In particular, by studying neutrinos originating from cosmic rays in the atmosphere, SK observed that muon neutrinos disappeared after traversing the Earth, while electron neutrinos remained unchanged.

Further advancements came with the Sudbury Neutrino Observatory (SNO) [24], which provided additional evidence supporting the notion of neutrino flavor change. SNO's observations revealed a deficit in the number of electron neutrinos compared to predictions based on solar models, suggesting that neutrinos were changing their flavor during their journey from the Sun to the Earth.

The phenomenon of neutrino flavor change was later confirmed by experiments such as KamLAND [25], a long-baseline reactor experiment, which detected the disappearance of electron neutrinos (ν_e) using artificial neutrino sources, and the accelerator experiments K2K [26], and MINOS [27], which measured the disappearance of muon neutrinos (ν_μ) and their antiparticles ($\overline{\nu}_\mu$).

In addition to the confirmation of the neutrino flavor-changing behavior, these experiments provided important informations on the oscillation neutrino probability, leading to the conclusion that it depends on the ratio of the distance traveled to the neutrino energy ($\frac{L}{E}$).

More recently, the long-baseline accelerator experiments T2K [28][7][9] and NOvA [29] have yielded significant results about neutrino oscillations, constraining the parameters of the PMNS matrix and sheding some light on the neutrino mass hierarchy, as briefly discussed in Sections 1.3.2 and 1.3.3, respectively.

1.3.2 Theoretical Frame

Neutrino oscillations are formally described within a framework involving three-flavored neutrinos, where at least two of them have non-zero masses.

The survival probability is governed by the Pontecorvo-Maki-Nakagawa-Sakata (PMNS) matrix U, a 3×3 unitary matrix, often referred to as the MNS mixing matrix [30] [31]. The MNS matrix provides a framework to describe the transformation between the three flavor eigenstates $|\nu_e\rangle$, $|\nu_\mu\rangle$, $|\nu_\tau\rangle$ and the three mass eigenstates $|\nu_1\rangle$, $|\nu_2\rangle$, $|\nu_3\rangle$ of neutrinos. In particular it is possible to write each flavour states as a superposition of all the mass eigenstates as

$$|\nu_\alpha\rangle = \sum_{i=1}^{3} U_{\alpha i} |\nu_i\rangle \tag{1.1}$$

where $\alpha = \{e, \mu, \tau\}$, and i = {1, 2, 3}. This relationship can be expressed in matrix form as:

$$\begin{pmatrix} \nu_e \\ \nu_\mu \\ \nu_\tau \end{pmatrix} = \begin{pmatrix} U_{e1} & U_{e2} & U_{e3} \\ U_{\mu 1} & U_{\mu 2} & U_{\mu 3} \\ U_{\tau 1} & U_{\tau 2} & U_{\tau 3} \end{pmatrix} \begin{pmatrix} \nu_1 \\ \nu_2 \\ \nu_3 \end{pmatrix}$$

The MNS mixing matrix U is often decomposed into four separate matrices, parametrized by the mixing angles, θ_{12}, θ_{13}, θ_{23}, the CP-violating phase, δ_{CP}, and two mass-squared differences, typically Δm^2_{21} and $|\Delta m^2_{31}|$. Additionally two phase factors α_1 and α_1 are considered. Therefore U can be expressed as:

$$
\begin{aligned}
U = &\begin{pmatrix} U_{e1} & U_{e2} & U_{e3} \\ U_{\mu 1} & U_{\mu 2} & U_{\mu 3} \\ U_{\tau 1} & U_{\tau 2} & U_{\tau 3} \end{pmatrix} = \\
= &\begin{pmatrix} 1 & 0 & 0 \\ 0 & c_{23} & s_{23} \\ 0 & -s_{23} & c_{23} \end{pmatrix} \begin{pmatrix} c_{13} & 0 & s_{13}e^{-i\delta_{CP}} \\ 0 & 1 & 0 \\ -s_{13}e^{i\delta_{CP}} & 0 & c_{13} \end{pmatrix} \begin{pmatrix} c_{12} & s_{12} & 0 \\ -s_{12} & c_{12} & 0 \\ 0 & 0 & 1 \end{pmatrix} \begin{pmatrix} e^{i\frac{\alpha_1}{2}} & 0 & 0 \\ 0 & e^{i\frac{\alpha_2}{2}} & 0 \\ 0 & 0 & 1 \end{pmatrix} = \\
= &\begin{pmatrix} c_{12}c_{13} & s_{12}c_{13} & s_{13}e^{-i\delta_{CP}} \\ -s_{12}c_{23} - c_{12}s_{23}s_{13}e^{i\delta_{CP}} & -c_{12}c_{23} - s_{12}s_{23}s_{13}e^{i\delta_{CP}} & s_{23}c_{13} \\ s_{12}s_{23} - c_{12}c_{23}s_{13}e^{i\delta_{CP}} & -c_{12}s_{23} - s_{12}c_{23}s_{13}e^{i\delta_{CP}} & c_{23}c_{13} \end{pmatrix} \begin{pmatrix} e^{i\frac{\alpha_1}{2}} & 0 & 0 \\ 0 & e^{i\frac{\alpha_2}{2}} & 0 \\ 0 & 0 & 1 \end{pmatrix}
\end{aligned}
$$

Where $c_{ij} = \cos\theta_{ij}$, $s_{ij} = \sin\theta_{ij}$, and δ_{CP} is the CP-violating phase, which is non-zero only if neutrino oscillation violates CP symmetry.

The phase factors α_1 and α_1 are physically meaningful only if neutrinos are Majorana particles, for example if the neutrino is identical to its antineutrino, consequently do not enter into oscillation phenomena.

Propagation

Since U is unitary (i.e., $U^\dagger U = UU^\dagger = \mathbf{1}$, where $U^\dagger$ is the conjugate transpose),it follows from Equation 1.1 that the three mass eigenstates can be expressed as a superposition of the three flavor eigenstates using the complex conjugate of U:

$$|\nu_i\rangle = \sum_\alpha U^*_{\alpha i}|\nu_\alpha\rangle \tag{1.2}$$

The probability of flavor-changing over time can be determined by expressing the time evolution of Equation 1.2 in terms of a plane wave, which represents a solution

to the time-dependent Schrödinger equation–in natural units:

$$|\nu_i(t)\rangle = e^{-i(E_i t - \vec{p}_i \cdot \vec{x})}|\nu_i(t=0)\rangle = \sum_\alpha U^*_{\alpha i} e^{-i(E_i t - \vec{p}_i \cdot \vec{x})}|\nu_\alpha\rangle \tag{1.3}$$

where

- t is the time from the start of the propagation;
- $|\nu_i(t)\rangle$ denotes the neutrino mass state at time t;
- E_i represents the energy of the mass eigenstate;
- $\vec{p}_i$ represents the momentum of the mass eigenstate ν_i;
- $\vec{x}$ indicates the position relative to its starting position.

In all currently observed neutrinos, given that neutrino masses are experimentally measured to be less than 1 eV and their energies are at least 1 MeV, the Lorentz factor, γ, exceeds 10^6 in all cases. Therefore, it is valid to assume that a neutrino is a relativistic particle, and to adopt the ultrarelativistic limit $|\vec{p}_i| \gg m_i$, where m_i is the neutrino mass. As a result, the energy can be approximated as:

$$E_i = \sqrt{p_i^2 + m_i^2} \simeq p_i + \frac{m_i^2}{2p_i} \simeq E + \frac{m_i^2}{2E} \tag{1.4}$$

where E is the energy of the wavepacket (particle) to be detected.

By employing also the approximation $t \approx L$ (c ≈ 1), where L represents the distance traveled, and neglecting the phase factors, Equation 1.3 simplifies to:

$$|\nu_i(t)\rangle = e^{-i(\frac{m_i^2 L}{2E})}|\nu_i(t=0)\rangle \tag{1.5}$$

From Equation 1.5, it becomes evident that the oscillation frequency $\frac{m_i^2 L}{2E}$ in the exponent depends on the mass, therefore eigenstates with distinct masses propagate with different frequencies. This means that neutrinos travel through space as mixtures of different mass eigenstates, each with its own oscillation frequency. In particular heavier mass eigenstates oscillate more rapidly between different flavor states compared to lighter ones. This difference in oscillation frequencies leads to interference between the flavor components of each mass eigenstate. Constructive

interference between these components allows a neutrino initially created with a particular flavor to transition to a different flavor during its propagation.

Finally, the probability to detect a neutrino originally of flavor α with flavor β is

$$P(\nu_\beta \to \nu_\alpha) = |\langle \nu_\beta | \nu_\alpha(L) \rangle|^2 = \left| \sum_{i=1}^{3} U^*_{\alpha i} U_{\beta i} e^{-i(\frac{m_i^2 L}{2E})} \right|^2 \tag{1.6}$$

Expanding as follows:

$$\begin{aligned} P(\nu_\alpha \to \nu_\beta) =& \delta_{\alpha\beta} - 4 \sum_{i>j} \mathrm{Re}\left(U^*_{\alpha i} U_{\beta i} U_{\alpha j} U^*_{\beta j}\right) \sin^2\left(\frac{\Delta m^2_{ij} L}{4E}\right) + \\ &+ 2 \sum_{i>j} \mathrm{Im}\left(U^*_{\alpha i} U_{\beta i} U_{\alpha j} U^*_{\beta j}\right) \sin\left(\frac{\Delta m^2_{ij} L}{2E}\right) \end{aligned} \tag{1.7}$$

where $\Delta m^2_{ij} = m^2_i - m^2_j$ and the $\delta_{\alpha\beta}$ term represents the Kronecker delta, which is equal to 1 if $\alpha = \beta$ and 0 otherwise.

In Equation 1.7 the imaginary part is retained for the neutrino case, while it is removed for the antineutrino case.

Considering for example the emergence of electron neutrinos (electron antineutrinos) from a muon neutrino (antineutrino) beam, $P(\overset{(-)}{\nu}_\mu \to \overset{(-)}{\nu}_e)$, Equation 1.11 became:

$$\begin{aligned} P(\overset{(-)}{\nu}_\mu \to \overset{(-)}{\nu}_e) \simeq & \sin^2\theta_{23} \sin^2 2\theta_{13} \sin^2\left(\frac{\Delta m^2_{32} L}{4E}\right) + \sin^2 2\theta_{13} \cos^2\theta_{23} \sin^2\left(\frac{\Delta m^2_{21} L}{4E}\right) + \\ & \overset{(+)}{-} J_0 \sin\left(\frac{\Delta m^2_{32} L}{4E}\right) \sin\left(\frac{\Delta m^2_{21} L}{4E}\right) \sin\left(\frac{\Delta m^2_{32} L}{4E}\right) \sin\delta_{CP} + \\ & + J_0 \sin\left(\frac{\Delta m^2_{32} L}{4E}\right) \sin\left(\frac{\Delta m^2_{21} L}{4E}\right) \cos\left(\frac{\Delta m^2_{32} L}{4E}\right) \cos\delta_{CP} + \\ & + \text{solar and matter effect terms} \end{aligned} \tag{1.8}$$

where $J_0 = \cos\theta_{13} \sin 2\theta_{12} \sin 2\theta_{23} \sin 2\theta_{13}$, while the solar term correspond to the contributions from the smaller mass-splitting, Δm^2_{21}, which dominate the long-baseline oscillations driven by the mixing angle θ_{12}.

The survival probability of $\overset{(-)}{\nu}_\mu$ is expressed as:

$$\begin{aligned} P(\overset{(-)}{\nu}_\mu \to \overset{(-)}{\nu}_\mu) \simeq & 1 - 4\sin^2\theta_{23}\cos^2\theta_{13}\cos^2\theta_{23}\sin^2\left(\frac{\Delta m^2_{32}L}{4E}\right) \\ & - 4\sin^2\theta_{23}\cos^2\theta_{13}\sin^2\theta_{23}\sin^2\theta_{13}\sin^2\left(\frac{\Delta m^2_{32}L}{4E}\right) \\ & + \text{solar and matter effect terms} \end{aligned} \tag{1.9}$$

Moving back from natural units to SI units, which are more convenient for the construction of experiments, in the formulas above, the term $\frac{\Delta_{ij}m^2L}{2E}$ has to be multiplied for the constant 1.27.

Two-neutrino case

Equation 1.7 holds for any number of neutrino generations. However, expressing it in terms of mixing angles becomes excessively complex when more than two neutrinos are involved in mixing, as obtained in Equations 1.8 and 1.9. Conversely, in the two-flavour neutrino framewok, it's much simpler to express the oscillation probability. In such case, the mixing matrix U reduces to:

$$U = \begin{pmatrix} U_{\alpha 1} & U_{\alpha 2} \\ U_{\beta 1} & U_{\beta 2} \end{pmatrix} = \begin{pmatrix} \cos\theta & \sin\theta \\ -\sin\theta & \cos\theta \end{pmatrix} \tag{1.10}$$

and the probability of a neutrino changing its flavor is (in SI units) is given by:

$$P(\nu_\alpha \to \nu_\beta) = \sin^2 2\theta \, \sin^2\left(\frac{1.27\Delta m^2 L}{2E}\right) \tag{1.11}$$

and the survival probability is expressed as:

$$P(\nu_\alpha \to \nu_\alpha) = 1 - P(\nu_\alpha \to \nu_\beta) \tag{1.12}$$

Figure 1.2 shows the evolution of neutrino flavor states along the propagation path for the case $\nu_\mu \to \nu_e$ oscillation.

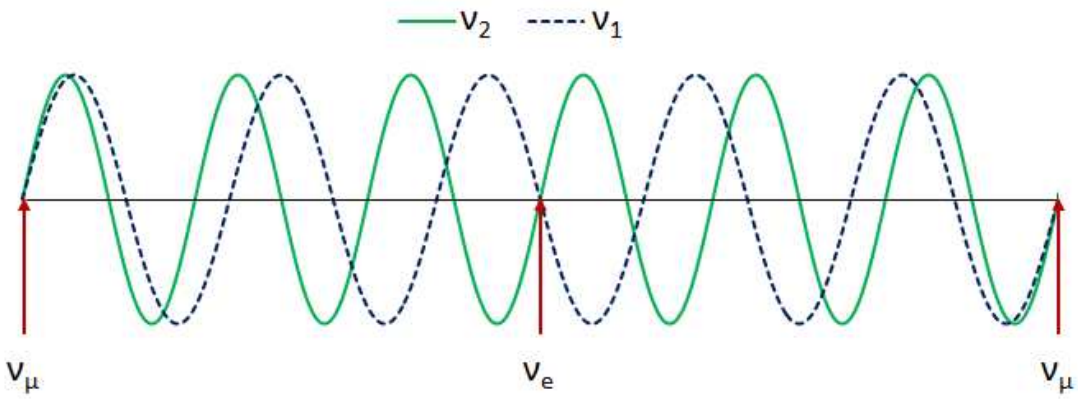

Figure 1.2: Evolution of neutrino flavor states along the propagation path. Beginning with a pure muon neutrino (ν_μ) beam on the left, the probability waves evolve, causing the neutrino flavor to transition into an electron neutrino (ν_e) in the middle region, before reverting to a muon neutrino (ν_μ) as the beam progresses to the right. Image taken from [2].

1.3.3 Mass ordering

Experimentally, it has been determined that at least two neutrino masses are non-zero and that Δm_{12} (also called Δm_{sol}) is greater than zero. Additionally, $|\Delta m^2_{32}|$ (sometimes called Δm_{atm}) $\approx |\Delta m^2_{31}|$ [3]. Therefore, there are two different possible Mass Orderings (MOs):

- Normal Ordering (also known as Normal Hierarchy): in this scenario, ν_1 is the lightest neutrino mass eigenstate, ν_2 is heavier than ν_1, and ν_3 is the heaviest.

- Inverted Ordering (also known as Inverted Hierarchy): here, ν_3 is the lightest neutrino mass eigenstate, followed by ν_1, and ν_2 is the heaviest.

The two MO are summarized in Figure 1.3.

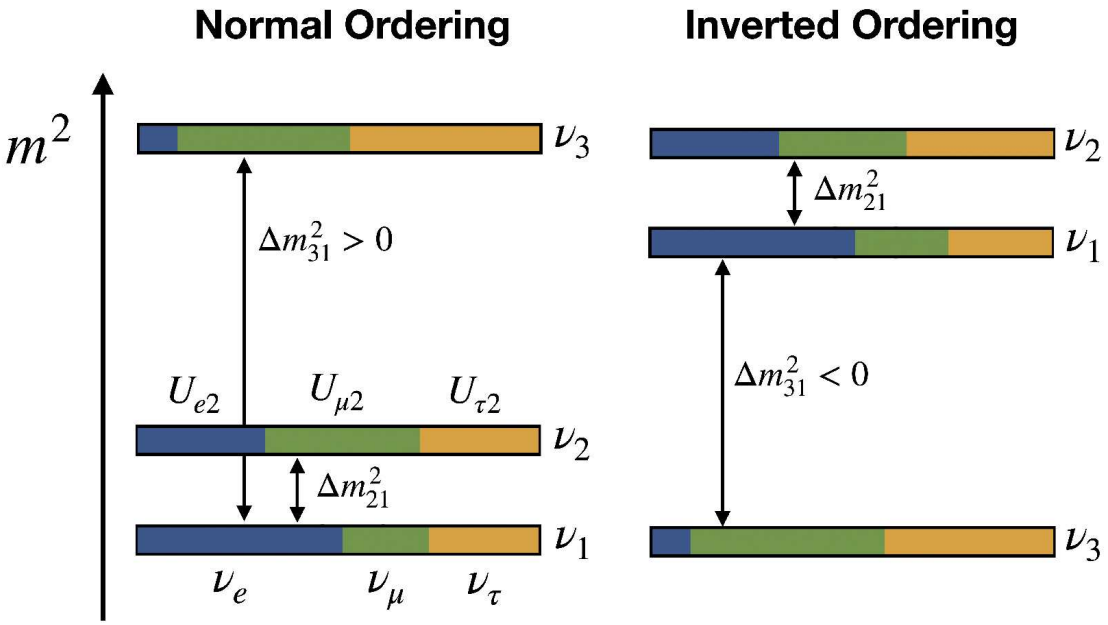

Figure 1.3: This figure illustrates the two possible MOs of neutrinos: Normal Ordering (NO) and Inverted Ordering (IO). In the Normal Ordering scenario, neutrino mass eigenstates are arranged such that $m_1 < m_2 < m_3$. Conversely, in the Inverted Ordering scenario, $m3 < m1 < m2$. Figure taken from [3].

1.3.4 Current Oscillation Parameters

The current knowledge of the oscillation paramters is summarized in the following Table [11] :

Oscillation Parameter	**Value (2024)**
Solar Mixing Angle $\sin^2(\theta_{12})$	0.307 ± 0.013
Mass Squared Difference Δm^2_{21}	$(7.53 \pm 0.18) \times 10^{-5}$ eV^2
Atmospheric Mixing Angle (NO) $\sin^2(\theta_{23})$	$0.558^{+0.015}_{-0.021}$
Atmospheric Mixing Angle (IO) $\sin^2(\theta_{23})$	$0.553^{+0.016}_{-0.024}$
Mass Squared Difference (NO) Δm^2_{32}	$(2.455 \pm 0.028) \times 10^{-3}$ eV^2
Mass Squared Difference (IO) Δm^2_{32}	$(-2.529 \pm 0.029) \times 10^{-3}$ eV^2
Reactor Mixing Angle $\sin^2(\theta_{13})$	$(2.19 \pm 0.07) \times 10^{-2}$
CP-Violating Phase δ_{CP}	$(1.19 \pm 0.22)\ \pi$ rad

Difference in Mass Squared $(\Delta m^2_{21} - \Delta m^2_{12})$	$< 1.1 \times 10^{-4}$ eV^2 (CL = 99.7%)
Difference in Mass Squared $(\Delta m^2_{32} - \Delta m^2_{23})$	$(-0.12 \pm 0.25) \times 10^{-3}$ eV^2

Table 1.1: Summary of the most recent values for neutrino oscillation parameters as of 2024. The uncertainties are given at the 1σ confidence level. The atmospheric mixing angle and mass squared differences are provided for both normal and inverted mass hierarchies. Additional parameters include the reactor mixing angle, CP-violating phase, and the differences in mass squared values. The values are taken from [11].

1.4 Neutrino interaction model

There are two primary types of neutrino interactions: charged-current (CC) and neutral-current (NC). In charged-current interactions, a neutrino exchanges a ±W boson with nucleons, while in neutral-current interactions, a neutrino exchanges a Z boson with nucleons. In Figure 1.4, the Feynman diagrams for the neutral current interaction (a) and the charged current for the case of a muon neutrino (b) and an electron neutrino (c) are shown.

Additionally, neutrino interactions can be classified based on the final state of the nucleon. If the nucleon's final state remains unchanged after neutrino scattering, the interaction is called "elastic". Conversely, if the final state of the nucleon changes, it is called "inelastic". In the case of CC interactions, a specific subtype is known as "quasi-elastic" (CCQE), where the nucleon undergoes a change but remains bound within the nucleus.

The interaction of neutrinos with matter is highly dependent on their energies.

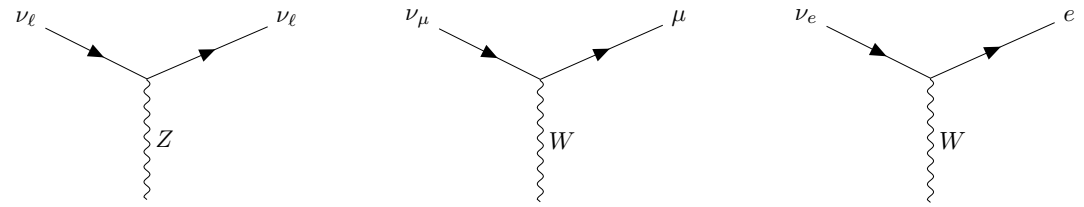

Figure 1.4: Feynman diagrams illustrating different neutrino interaction processes. (a) Neutral current (NC) interaction, where a neutrino interacts with a target nucleus via the exchange of a neutral weak boson (Z). (b) Charged current (CC) interaction involving a muon neutrino (ν_μ), where the neutrino interacts with a target nucleus through the exchange of a charged weak boson (W), resulting in the production of a muon. (c) Charged current (CC) interaction involving an electron neutrino (ν_e), where the neutrino interacts with a target nucleus through the exchange of a charged Weak boson (W), resulting in the production of an electron.

At lower neutrino energies, elastic or quasielastic scattering processes dominate. In elastic scattering, neutrinos interact with individual nucleons within atomic nuclei, transferring momentum but not changing the nature of the target particle. In quasielastic scattering, a single charged lepton of the same flavor as the incident neutrino is produced, together with the scattered neutrino. On the other hand, at higher neutrino energies, Deep Inelastic Scattering (DIS) becomes the main channel of interaction. In DIS, the neutrino interacts with individual quarks within nucleons, leading to the disruption of nucleons within the nucleus. This process results in the constituent quarks undergoing hadronization, producing a large multiplicity of bound hadronic states.

In addition, resonant processes, in which the energy of the target nucleon is raised to an excited baryonic state, occur as well. In particular, single resonant pion production dominates at neutrino energies between the (quasi)elastic and DIS regimes.

Finally, Final-State Interactions (FSI) must also be considered. These interactions occur after the primary collision process and involve the particles produced in the initial collision interacting with each other and with the surrounding medium.

In the following the processes introduced above are described with more details.

1.4.1 Neutral-and charged-current interactions

Neutral current (NC) and charged current (CC) neutrino interactions become significant at energies of above a few hundred MeV. Therefore, for the T2K experiment, which operates with a narrow-band muon neutrino beam with energies around 0.5 GeV to 1 GeV, both NC and CC interactions are important.

At these energies, neutrinos are energetic enough to undergo both types of interactions with the target nuclei in the detector material. In particular for CC interactions the neutrino must be energetic enough to produce the mass of the charged lepton in the final state, consequently the cross-section depends on the neutrino flavour. Conversely, NC interactions contribute to background processes due to their inability to produce flavor-identifiable charged leptons.

For CC interactions, two processes are distinguished with respect to the production of zero or one pion in the final state, respectively CC0π and the CC1π^+. These interactions are important because they provide important selection criteria for the

T2K oscillation analysis,

1.4.2 Charged-Current Quasi-Elastic process

CCQE interactions occur when a neutrino interacts with a target nucleon, either a free nucleon such as hydrogen or a nucleon within a nuclear target like carbon or oxygen, if the neutrino has sufficient energy to produce a charged lepton.

The term "quasielastic" refers to a process that resembles elastic scattering, in which the target nucleon is excited but remains intact after the interaction, with no mesons produced in the final state. These interactions contribute to the CC0π+ cross section. In contrast, when the nucleon is ejected from the target nucleus, leaving a hole, the process is called one-particle one-hole (1p1h).

CCQE processes are important since the CCQE cross section is largely dominant around 600 MeV, which is also the T2K peak energy. In CCQE interactions, a (anti-)neutrino interacts with a target nucleon in a nucleus, resulting in the production of a negatively (positively) charged lepton of the same flavour and a corresponding nucleon. The lepton typically carries most of the energy of the incident neutrino.

The interaction occurs via the exchange of a W-boson. As a two-body process, CCQE interactions follow momentum and energy conservation laws, allowing the reconstruction of the neutrino's energy, as will be done in Section 4.2. CCQE interactions usually produce single-ring electron-like or muon- like events.

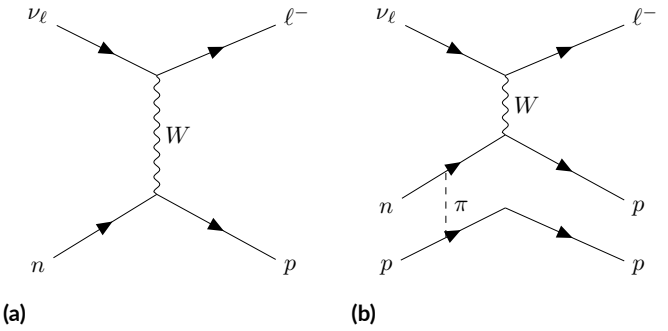

Figure 1.5: Feynman diagrams illustrating (a) the Charged-Current Quasielastic (CCQE) interaction and (b) a multi-nucleon process. Although the two processes are very similar, in (a), a neutrino interacts with a single nucleon, resulting in the production of a charged lepton while in (b), the neutrino interacts with a correlated pair of nucleons within a target nucleus (2p2h).

1.4.3 Multi-nucleon processes

Multi-nucleon processes, also known as "np-nh" (n-particles n-holes), refer to interactions where the incoming neutrino interacts with a correlated pair or a cluster of nucleons within a target nucleus, leading to the emission of more than one nucleon in addition to the corresponding lepton. Since they are not two body processes, multi-nucleon processes are considerably more complex to calculate and measure.

The cross-section for these events is generally smaller than that for CCQE processes. However, due to their similarity with pure CCQE events, these interactions increase the total number of expected CC0π events.

An example of a "two-proton two-hole" (2p2h) interaction, in which two nucleons are ejected from the nucleus, is shown in Figure 1.5 (b).

np-nh events are inherently nuclear processes that can only be investigated by modern neutrino experiments using a nuclear target.

1.4.4 Single pion production

Single pion production (SPP) is the dominant interaction in the 1 to 10 GeV range, whereas it is the second most dominant process after CCQE at energies just above 0.5 GeV. In SPP processes, reconstructing the neutrino energy is more complex than in QE interactions due to the higher momentum transfer to the nucleon.

There are two primary SPP interaction processes: resonant pion production and CC coherent pion production, which are described below.

Resonant pion production

The largest contribution to SPP comes from resonant pion production, where the neutrino excites the incident nucleon to a delta baryon state, which subsequently decays into a meson or a photon and a baryon.

Low-momentum positively-charged pions decay into a muon and a muon neutrino, which further decays into a Michel electron (or positron) and an electron neutrino. This process can also produce photons or, when the de-excitation energy is enogh, heavier mesons, such as kaons and etas. The Feynman diagram of this interaction is shown in Figure 1.6 (a).

CC coherent pion production

In addition to the resonant production mode, coherent production, where the neutrino interacts with the nucleus as a whole, and diffractive production, can produce pions without exciting the nucleus. In these cases, the nucleon is not treated independently of the nucleus. The Feynman diagram of this interaction is shown in Figure 1.6 (b).

1.4.5 Deep Inelastic Scattering processes

At high neutrino energies and momentum transfers, the nucleon can be excited to much higher energies, leading to the production of multiple hadrons during deexcitation if sufficient energy is available. In deep inelastic scattering (DIS), when the energy is sufficiently high, the neutrino can probe the internal structure of the nucleon, causing quarks to become unbound, as shown in Figure 1.6 (c). This process disrupts the nucleus, leaving constituent quarks and gluons to undergo hadronization. As the momentum transfer increases into the inelastic regime, the interaction cross section becomes dependent on the nucleon's internal structure, described by Parton Distribution Functions (PDFs). Hadronization of the constituent quarks typically results in a final state with multiple pions or mesons.

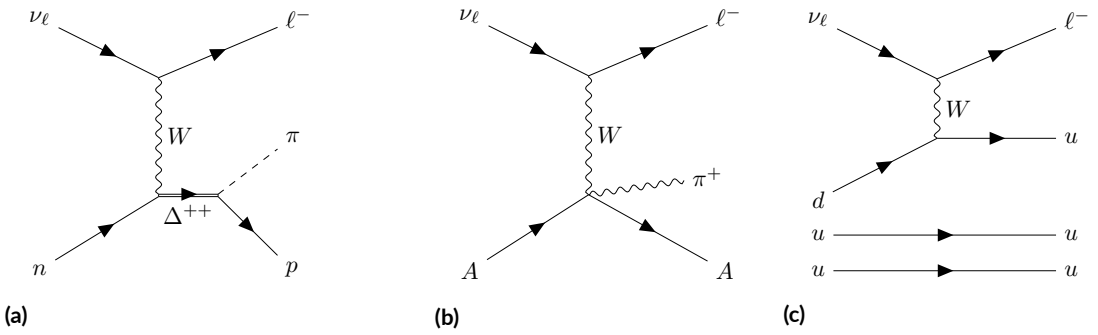

Figure 1.6: Feynman diagrams illustrating charged-current pion production processes: (a) charged-current resonant pion production, where the neutrino excites a nucleon to a Δ^{++} baryon state that decays into a pion and a baryon; (b) charged-current coherent pion production, where the neutrino interacts with the nucleus as a whole, producing a pion without exciting the nucleus; (c) charged-current deep inelastic scattering (DIS), where the neutrino interacts with a nucleon, resulting in the breakup of the nucleon and production of multiple hadrons.

2

The T2K experiment

The Tokai to Kamioka (T2K) [7][6][28] experiment is a significant undertaking in the field of neutrino physics. It began in the mid-2000s, with construction beginning in 2004 and data collection starting in 2009. This experiment is a collaboration involving 500 physicists and engineers from 60 international research institutions across 12 countries in Europe, Asia, and North America. It is jointly hosted by the High Energy Accelerator Research Organization (KEK) [32] and the University of Tokyo's Institute for Cosmic Ray Research (ICRR) [33]. The primary objective of T2K is to measure the parameters of neutrino oscillation.

The T2K experiment has provided the world's most precise measurement of the oscillation parameter θ_{23} and has provided valuable insights into the matter-antimatter asymmetry in neutrino oscillations. Additionally, it was the first experiment to observe the appearance of electron neutrinos in a muon neutrino beam.

The T2K experiment generates a beam of predominantly muon neutrinos with a peak energy of $E_\nu \approx 0.6\,\text{GeV}$. This is achieved by directing protons from an accelerator onto a target, where magnetic horns are employed to focus the resulting collision products, which subsequently decay into the neutrinos that constitute the beam. A suite of near detectors, located 280 meters downstream from the production target, characterize the neutrinos before long-baseline oscillations occur. A far detector, situated 295 kilometers away, measures these long-baseline oscillations. Figure 2.1 illustrates a schematic layout of the T2K experiment.

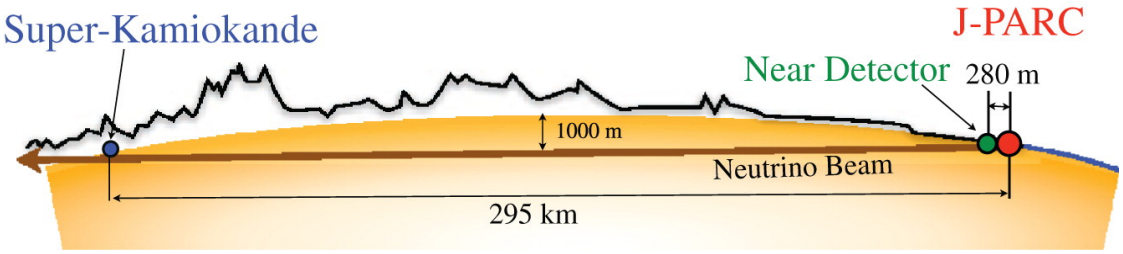

Figure 2.1: Diagram of the T2K experiment setup: neutrinos are produced at the Japan Proton Accelerator Research Complex (J-PARC) in Tokai, then travel 295 km through the Earth's crust to the Super-Kamiokande detector in Kamioka. A Near Detector positioned 280 meters from the proton target measures the neutrino beam's initial properties. Image taken from [4].

2.1 The J-PARC accelerator

The T2K experiment employs advanced accelerator physics to generate and investigate neutrinos. This process begins at the Japan Proton Accelerator Research Complex (J-PARC) in Tokai [6].

The J-PARC facility comprises three accelerators: a 300-meter-long linear accelerator (LINAC), a rapid-cycling synchrotron (RCS), and the main ring (MR) synchrotron.

The LINAC is used to accelerate an H^- beam to 400 MeV. Subsequently, the H^- beam is converted into an H^+ beam through charge-stripping foils during the injection into the rapid cycling synchrotron (RCS). Within the RCS, the beam is further accelerated to 3 GeV at a frequency of 25 Hz.

From the RCS, the proton beam is injected into the MR and accelerated to 30 GeV. Protons are grouped into eight bunches, each containing approximately 3×10^{14} protons. These can be extracted using either fast extraction for the hadron beamline or slow extraction for the neutrino beamline.

In fast extraction mode, eight bunches are extracted within a single turn using a set of five kicker magnets and directed toward the proton beamline. The beam can be aborted by utilizing the fast extraction kicker magnets to redirect it to a beam dump.

In slow extraction, a ribbon is employed to split the bunch while a kicker magnet directs a portion of each bunch to the hadron experiment beamline over multiple turns. An illustration of the setup is presented in Figure 2.2 (a).

The neutrino beamline consists of two sequential sections: the primary and sec-

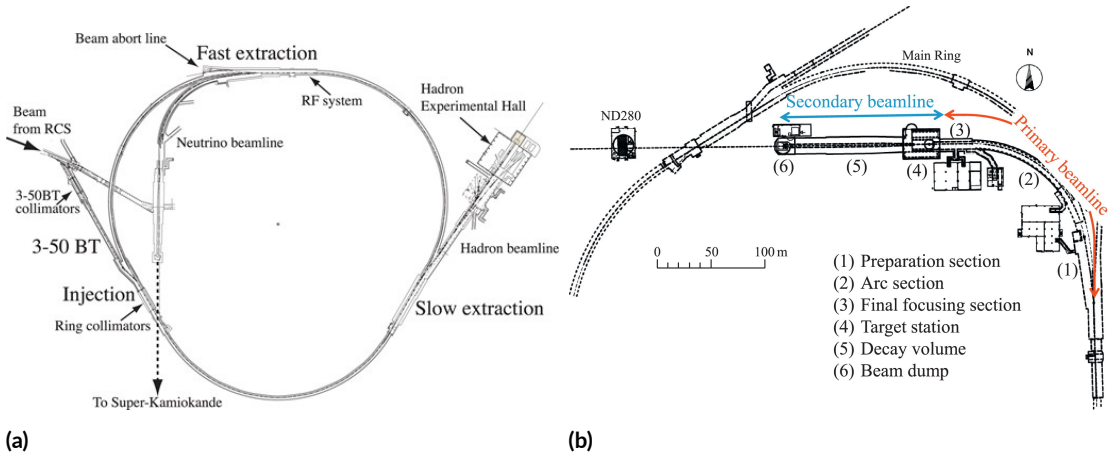

Figure 2.2: (a) Layout of the MR and the associated experimental facilities, the hadron experimental hall, and the neutrino beam line. Image taken from [5]. (b) Overview of the T2K neutrino beamline at-J PARC. Images taken from [6].

ondary beamlines. In the primary beamline, the extracted proton beam is monitored and directed toward Kamioka. In the secondary beamline, the proton beam strikes a target to produce secondary hadrons, which are focused by magnetic horns and subsequently decay into neutrinos. An overview of the neutrino beamline is presented in Figure 2.2 (b).

The primary proton beamline directs protons towards a 90 cm long and 2 cm diameter graphite target, resulting in collisions that produce various hadrons, including charged pions and kaons. To select specific charged pions ($\pi^{\pm}$), three electromagnetic horns are employed, with the Forward Horn Current (FHC) mode selecting π^{+} and the Reverse Horn Current (RHC) mode selecting π^{-}. However, complete separation of charged particles is not achievable, leading to contamination from other particles, particularly kaons and wrong sign pions, which is more pronounced in RHC mode due to the nature of pion production. The produced pions can decay into muons and neutrinos over a 100-meter decay volume. Since the number of neutrinos cannot be directly measured, the total expected neutrino quantity during a run is assessed using the number of protons on target (POT), based on the assumption that the neutrino production rate remains stable relative to the proton rate over time.

The data accumulated and measured in POT up to the present is presented in Figure 2.3, totaling 3.6×10^{21} POT.

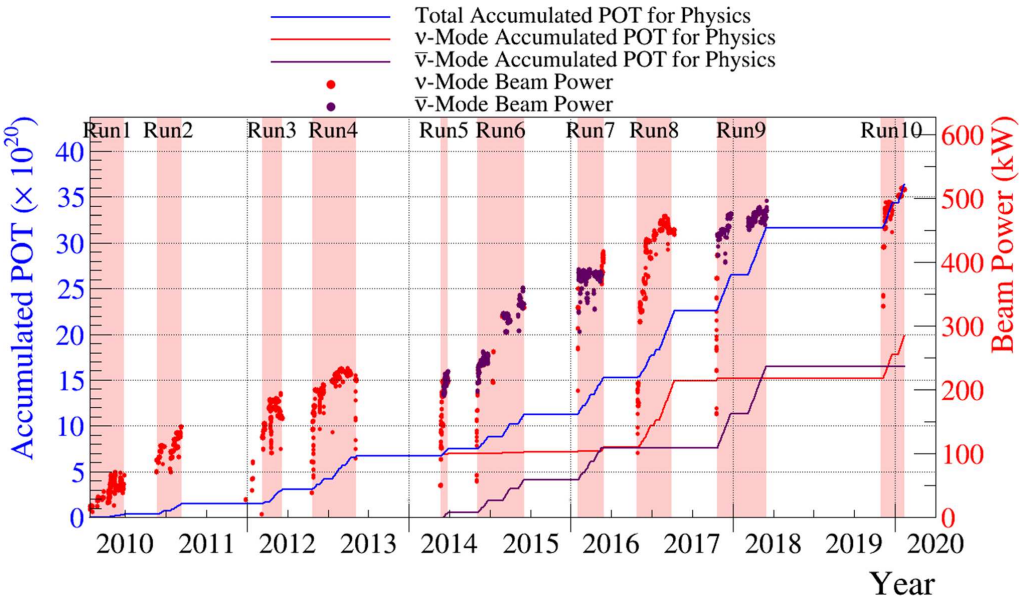

Figure 2.3: The protons on target (POT) delivered to T2K by the MR over time, with the beam intensity overlaid. The blue line refers to FHC mode while the violet line refers to RHC mode. Image taken from [7].

In the decay volume, charged pions decay into muons and muon neutrinos through the process $\pi^+ \rightarrow \mu^+ + \nu_\mu$. To capture as many muons as possible before they decay into electrons via $\mu^+ \rightarrow e^+ + \nu_e + \bar{\nu}_\mu$, a beam dump is employed. This decay can contribute to an electron neutrino background. Additionally, kaons contribute to the electron neutrino background as well, decaying through $K^+ \rightarrow \pi^0 + e^+ + \nu_e$. Kaons can also decay into muons, complicating the modeling of muon neutrino flux, especially at higher energies where kaon decays become more significant. A summary of the various contributions to neutrino production considered in the flux simulation is presented in Table 2.1. The decay modes for the antineutrinos $\bar{\nu}_\mu$ and $\bar{\nu}_e$ can be derived by applying charge conjugation to the decay modes of π^-, K^-, and μ^-.

2.2 Near detector complex

The T2K experiment utilizes a complex near detector system to measure neutrino interaction properties close to the source. Located 280 meters from the neutrino production target, the near detector complex comprises two main components: the off-axis near detector (ND280) and the Interactive Neutrino GRID (INGRID).

Table 2.1: The decay modes that generate neutrinos which are taken into account in the flux simulation of T2K, along with their corresponding branching ratios expressed as percentages [12].

Decay Mode	Branching Ratios (%)
$\pi^+ \to \mu^+ + \nu_\mu$	99.9877
$\pi^+ \to e^+ + \nu_e$	1.23×10^{-4}
$K^+ \to \mu^+ + \nu_\mu$	63.55
$K^+ \to \pi^0 + \mu^+ + \nu_\mu$	3.353
$K^+ \to \pi^0 + e^+ + \nu_e$	5.07
$K^0_L \to \pi^- + \mu^+ + \nu_\mu$	27.04
$K^0_L \to \pi^- + e^+ + \nu_e$	40.55
$\mu^+ \to e^+ + \bar{\nu}_\mu + \nu_e$	100

The ND280 detector, positioned off the neutrino beam axis, is specifically designed to measure the flux, energy spectrum, and interaction rates of neutrinos prior to oscillation. It consists of several sub-detectors, including a π^0 detector, a tracker system with fine-grained detectors (FGDs) and time projection chambers (TPCs), an electromagnetic calorimeter (ECal), and a side muon range detector (SMRD). This configuration allows for precise reconstruction of neutrino interaction events, providing essential data to improve the understanding of neutrino properties and enhance the accuracy of oscillation measurements.

On the other hand, the INGRID detector is situated on-axis and comprises a grid of iron and scintillator modules arranged in a cross pattern. Its primary purpose is to monitor the direction and intensity of the neutrino beam, ensuring both stability and alignment. The INGRID detector continuously measures the neutrino interaction rate, allowing for real-time monitoring and adjustments to the beam, thus ensuring the accuracy and reliability of the experimental results.

Together, these near detectors provide paramount information about the initial neutrino flux and interactions. This information is utilized to constrain the uncertainties on the neutrino oscillation parameters.

The near detector complex is shown in Figure 2.4.

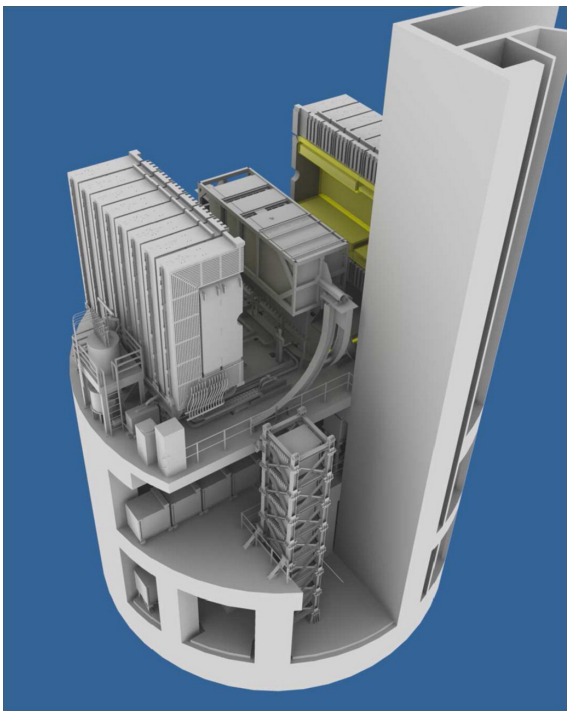

Figure 2.4: Near detector complex of the T2K experiment. Both the off-axis near detector at 280 metres (ND280) and the Interactive Neutrino GRID detector (INGRID) detector are housed in the same pit underground, with the centres at approximately 24 m and 33 m, respectively, below the surface. The ND280 can be seen in open configuration at the top, while the INGRID is shown at the bottom. Image taken from [6].

2.2.1 The INGRID on-axis detector

The on-axis neutrino Near Detector, INGRID [6], measures the rate and directional stability of the neutrino beam. Positioned along the axis of the neutrino beam, this detector is specifically designed to directly monitor the direction and intensity of the beam through interactions within iron, providing sufficient statistical data for daily measurements at the nominal beam intensity. By analyzing the number of neutrino events detected in each module, the beam center can be determined with a precision of 0.4 mrad at the ND280 complex.

The INGRID detector is composed of 14 identical modules arranged in a cross structure, divided into two identical groups, as shown in Figure 2.5 (a). It covers a transverse area of 10 m × 10 m, with its center aligned at 0° with respect to the primary proton beam.

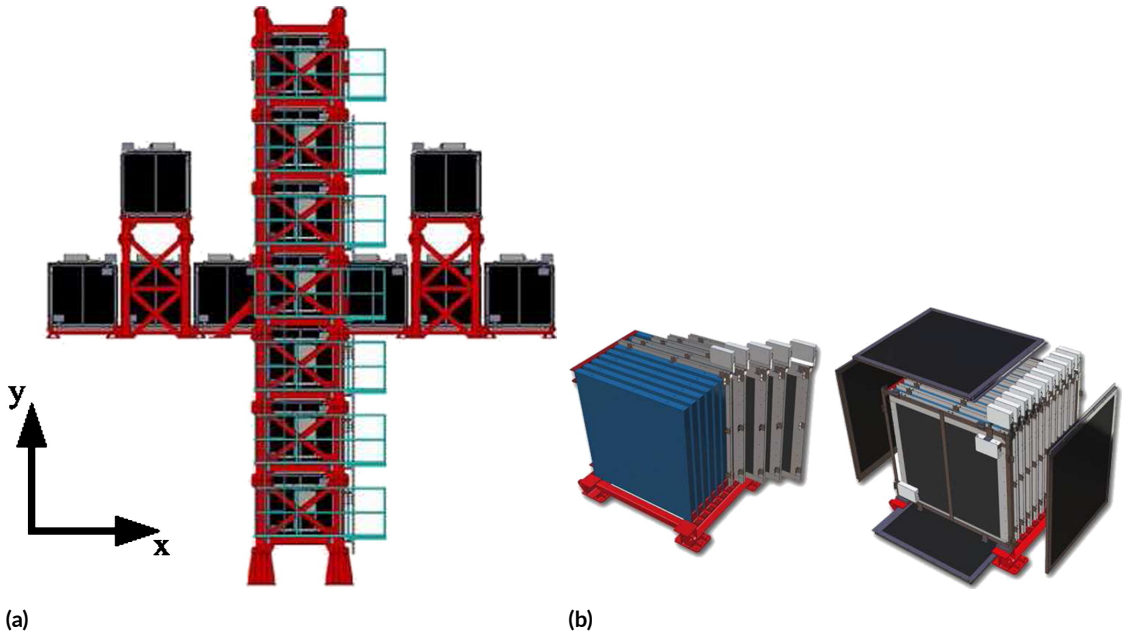

Figure 2.5: (a) The INGRID on-axis detector. (b) An INGRID module. On the left the tracking planes (blue) and iron plates. On the right the veto planes (black). Images taken from [6].

Each of the 14 modules consists of 11 scintillator planes interleaved with 9 iron plates, targeting a mass of 7.1 tonnes. Surrounding these modules are scintillator veto plates that assist in rejecting charged particles originating from outside the modules. The scintillator planes are composed of 24 vertical scintillating bars at-

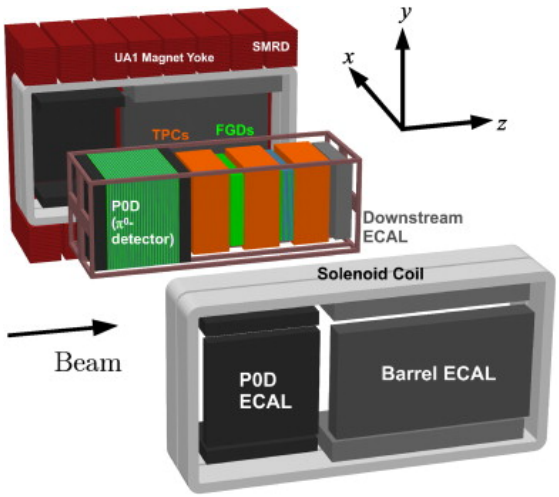

Figure 2.6: Exploded view of the ND280 off-axis detector. Image taken from [6].

tached to 24 horizontal scintillating bars. Figure 2.5 (b) presents an exploded view of the INGRID module.

2.2.2 The Off-Axis Near Detector

The ND280 detector, located 280 meters from the neutrino production target, is positioned 2.5° off-axis with respect to the proton beam that produces the neutrino flux as the far detector Super-Kamiokande (SK). This off-axis placement allows the detectors to sample a narrower neutrino energy distribution, peaking near the maximum of the ν_e appearance spectrum.

ND280 is a magnetized off-axis tracking detector, serving as the primary detector at the 280-meter site. The entire detector setup is contained within a magnet recycled from the UA1 and NOMAD experiments at CERN [34], which provides a magnetic field of 0.2 T. The dimensions of the detector are 5.6 m in width, 6.1 m in height, and 7.6 m in length. The coordinate system is established such that the z-axis aligns with the nominal neutrino beam direction, while the x and y axes correspond to the horizontal and vertical orientations, respectively [7].

The ND280 detector is equipped with three principal target subdetectors: a π^0 detector (PØD) and two Fine-Grained Detectors (FGDs). These components serve to provide both the mass of the target material—comprising plastic scintillator, water, and brass—and facilitate three-dimensional tracking through the detection

of scintillation light. Positioned downstream of each target subdetector is a gaseous argon time projection chamber (TPC), which offers detailed information regarding track curvature for particles that exit the target subdetectors and enter the TPC.

The FGDs and TPCs collectively constitute the tracker region of the detector, located downstream of the PØD within the T2K beamline. Surrounding each of these detectors and situated downstream of the tracker region are thirteen modules of the electromagnetic calorimeter (ECal). The ECal is designed as a lead-scintillator sandwich calorimeter, which facilitates electromagnetic showering from photons and electrons while also enabling the identification of exiting muons as minimum ionizing particles (MIPs), which produce a single track without generating a shower.

Since 2023, the PØD has been replaced by a Super Fine-Grained Detector (SuperFGD) and High-Angle Time Projection Chambers (HATPCs).

The SuperFGD features highly segmented target material, enhancing the ability to reconstruct neutrons and low-momentum protons. The HATPCs improve momentum measurement, charge identification, and particle identification with better angular acceptance than previous detectors. Additionally, the system includes Time-of-Flight (ToF) capabilities, providing precise timing information to reject backgrounds and enhance reconstruction accuracy.

2.3 Far Detector

The Super-Kamiokande (SK) detector is the far detector for the T2K experiment and is situated within the Mozumi mine, near Hida in Gifu Prefecture, Japan, at a distance of 295.3 kilometers from the neutrino production target. This facility is a water Cherenkov detector, and is protected by a 2.7-kilometer water-equivalent overburden, being located 1,000 meters underground in the Kamioka Mine to mitigate the effects of cosmic rays and other forms of background radiation.

The detector consists of a large cylindrical tank that contains 50 000 metric tons of ultra-pure water, with dimensions of 39 meters in diameter and 41.4 meters in height. The tank is partitioned into two distinct regions:

- **The Inner Detector (ID)**: This region is responsible for the detection of neutrino interactions and is equipped with 11 146 photomultiplier tubes (PMTs), each with a diameter of 50 centimeters. These PMTs are highly sensitive to

light and are utilized to detect the Cherenkov radiation generated by neutrino interactions.

- **The outer detector (OD)**: A surrounding layer used to identify incoming cosmic rays or particles that enter from outside. This region contains 1,885 20-inch PMTs and helps distinguish neutrino signals from background events. The structure is displaced 2 m from the OD wall and there is a 55 cm dead region between the ID and OD surfaces.

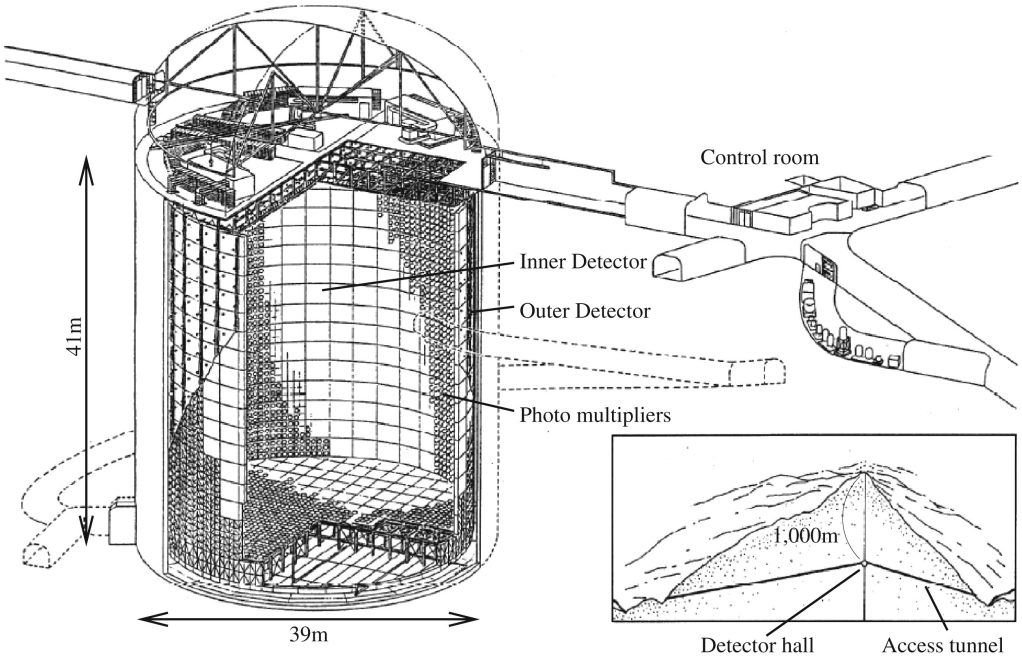

Figure 2.7: Diagram of the Super-Kamiokande Detector. Image taken from [6].

2.3.1 The Cherenkov rings

When neutrinos interact with water molecules inside the tank, they can produce charged particles (such as electrons or muons). If these particles move faster than the speed of light in water (approximately 0.75c), they emit Cherenkov light. This Cherenkov light forms a cone that spreads out from the particle's path. Since the angle of the Cherenkov radiation cone is constant for a given speed of the particle, a circular pattern of light, also known as Cherenkov ring, is detected from the PMTs.

Events are classified based on several criteria, including the number of primary Cherenkov rings produced, the specific ring patterns for each ring, and the presence

of time-delayed electron rings. The time-delayed electron rings arise from the decay of muons, as a muon can decay into a positron or electron (and neutrinos) after coming to rest in the detector. The resulting electron, which produces a Cherenkov ring after the muon decays, is known as a Michel electron. These Michel electrons serve as a signature for identifying muons that have decayed within the detector.

Several types of events can be identified: 1Rμ events feature a single sharp Cherenkov ring, indicative of a muon produced in a charged-current muon neutrino interaction. 1Re events show a single diffuse Cherenkov ring, corresponding to an electron produced in a charged-current electron neutrino interaction. In the case of 1Re+1de events, the primary electron ring is accompanied by a time-delayed ring caused by a Michel electron, indicating that the initial interaction produced a muon which subsequently decayed into an electron. More complex events, such as Multi-Rμ+1 or 2 de, involve multiple primary Cherenkov rings from several particles, likely from multi-particle production in neutrino interactions, with one or two delayed electron rings from muon decays.

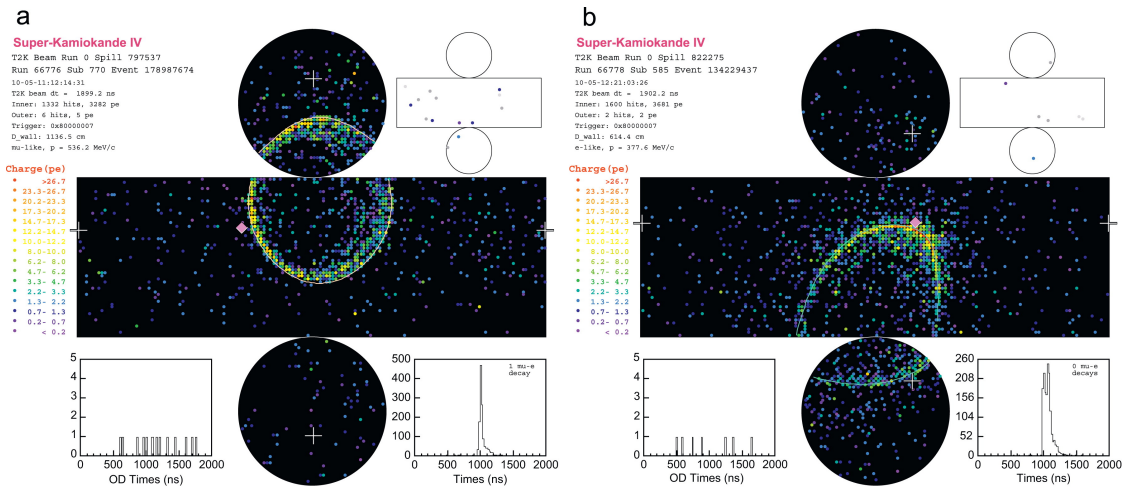

Figure 2.8: Two examples of events detected by the T2K.

A fit to a set of 22 samples at the near detector allows to reduce drastically the uncertaity on the number of expected ν interactions at the far detector. In particular, from $\approx 17\%$ to $\approx 3/5\%$.

2.4 Neutrino flux model

The neutrino flux model is paramount for T2K oscillation analysis. Accurately predicting the T2K neutrino beam flux requires an understanding of the contributions and kinematics of neutrino parents. The modeling of hadron production in the graphite target is complex due to limited data on proton-carbon interactions in the 30 GeV range. Therefore, there is a necessity for measurements of hadron production from a graphite target. Given that direct measurements of hadron kinematics are not operable within the T2K target hall, external data from the NA61/SHINE experiment [35] are employed to refine these models. Predictions for pions leaving the target are adjusted to match the π^+ and π^- yields recorded by NA61/SHINE, based on 2009 data from a replica of the T2K production target.

Prior to the 2020 results, T2K relied on "thin target" data and secondary interactions within the target were simulated through Monte Carlo simulations and the FLUKA package [36]. In the 2020 analysis, hadron production was measured in a T2K-replica target. The FLUKA 2011.2x software simulates interactions within the target, while particles emerging from the target and decaying into neutrinos are tracked through the horn field using the JNUBEAM package, based on GEANT3 [12].

Pions that leave the target and are within the phase space covered by the replica target data, which is about 90% of the neutrinos at the flux peak, are given the weight

$$w(p, , z, i) = \frac{dn^{NA6}(p, \theta, z, i)}{dn^{MC}(p, \theta, z, i)}$$

which is calculated as the ratio of the number of pions observed in the NA61/SHINE experiment (dn^{NA61}) to the number of pions predicted by the Monte Carlo simulation (dn^{MC}) for a given set of momentum, angle, position, and particle of type i = $\{\pi^+ , \pi^- \}$.

Simulations for particles that are not covered by the replica target data, and interactions occurring outside the target, are tuned to NA61/SHINE data on $\pi\pm$, K $\pm$, K0, Λ, and p yields from a thin target taken in 2009.

Overall, tuning with the NA61/SHINE 2009 replica target data reduces the uncertainty from 9 to 5% near the flux peak.

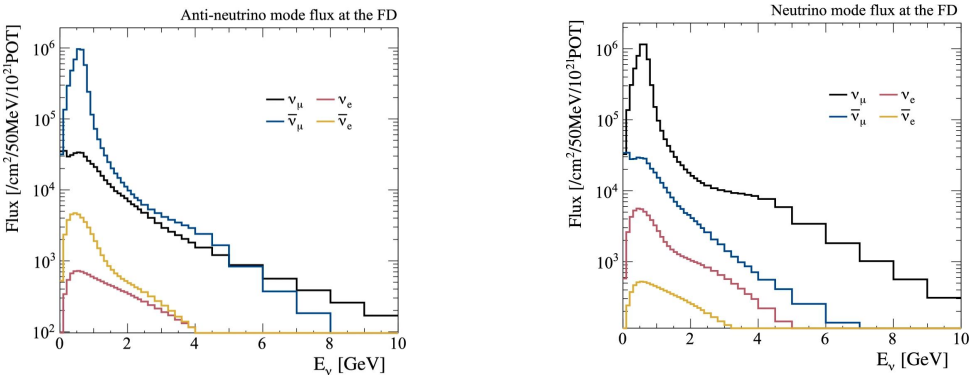

Figure 2.9: The predicted unoscillated neutrino fluxes at the FD in ν-mode (top) and $\bar{\nu}$-mode (bottom) in logarithmic scale with an extended range, after the tuning to NA61/SHINE data on the T2K replica target. Image taken from [7].

3

The T2K oscillation analysis

The primary objective of the T2K Oscillation Analysis (OA) is to extract the key neutrino oscillation parameters θ_{13}, θ_{23}, δ_{CP}, and Δm^2_{32} (NO)/$|\Delta m^2_{31}|$ (IO) (the mass splitting) by comparing the unoscillated and oscillated energy spectra of the T2K neutrino beam. This analysis is highly multi-dimensional and demands careful management of systematic uncertainties, relying on numerous neutrino interaction samples.

The oscillation parameters are extracted from the T2K data by varying both the oscillation parameters and the nuisance parameters (such as flux, cross-section, and detector response) within the Monte Carlo simulations. The optimal combination that best matches the observed data is identified. After marginalizing over the nuisance parameters, Bayesian credible intervals and contours or frequentist confidence intervals and contours for the oscillation parameters are then derived.

The effect of adjusting the oscillation parameters on the survival probability of muon (anti)neutrinos over the T2K baseline and energy range can be combined with the T2K flux to predict the beam composition at Super-Kamiokande (SK) [8].

Table 3.1: Comparison of the BANFF and MaCh3 fitting methods.

BANFF	**MaCh3**
MINUIT minimizer	Markov Chain Monte Carlo Fitter
Frequentist approach	Bayesian approach
Gives postfit covariance matrix to FD fitters	Used in MaCh3 ND+FD joint fit

3.1 The T2K analysis streams

T2K follows two main analysis approaches. The first approach involves a frequentist sequential analysis stream through the BANFF and P-Theta framework. This approach involves two sequential analyses, where data is fitted first at the near detector and then at the far detector (Figure 3.1(a)). The second approach is a Bayesian analysis perfomed within the Markov Chain 3 flavour (MaCh3) framework, which performs a simultaneous fit to data from both the near and far detectors (Figure 3.1(b)).

The diagrams illustrating the two different approaches are shown in Figure 3.1.

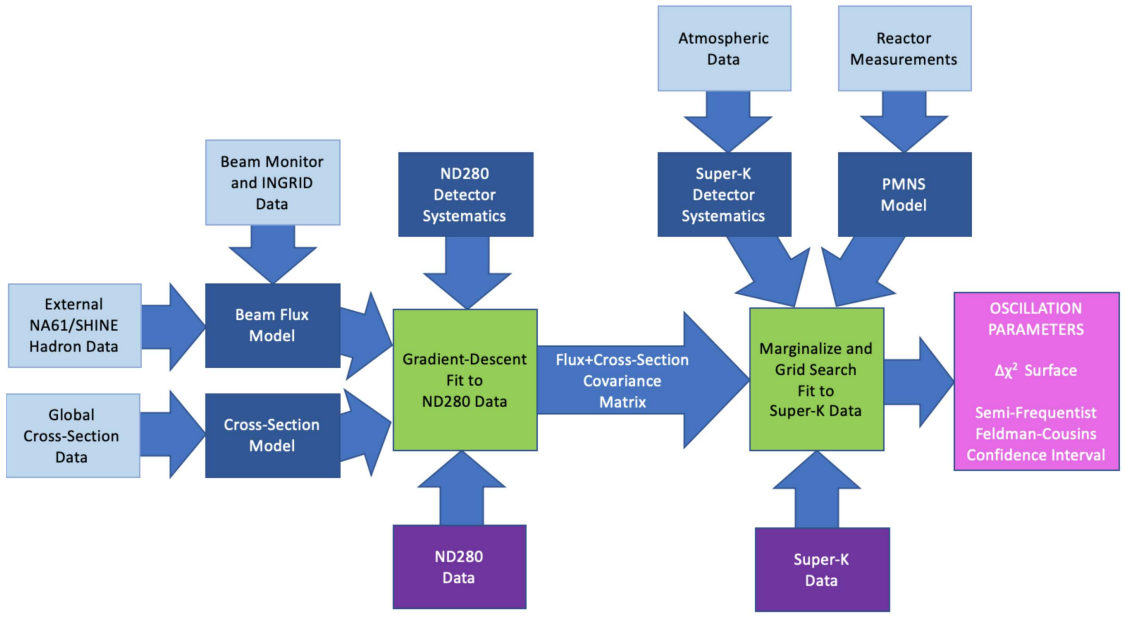

(a)

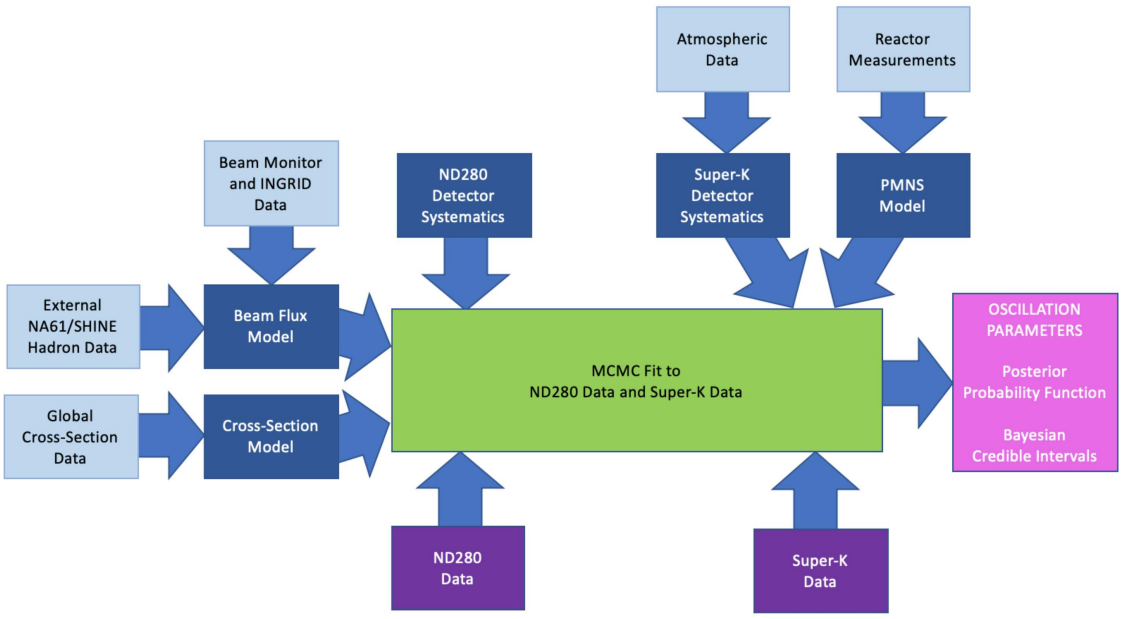

(b)

Figure 3.1: Flow diagram illustrating the two parallel analysis approaches in the T2K oscillation analysis. Both streams use the same input data from ND280 and Super-Kamiokande (SK), derived from internal and external measurements. Beyond the difference between sequential and simultaneous fitting, the fitting methods and the interpretation of the results also vary. In the sequential fit stream, the BANFF gradient descent fit generates a best-fit set of parameters and their covariance matrix, which serve as priors for the P-Theta analysis. The P-Theta fit then marginalizes over flux, cross-section, and SK detector systematics, allowing for a computationally feasible grid search over the remaining oscillation parameters, producing a $\Delta\chi^2$ surface interpreted using frequentist methods. In the simultaneous fit stream, the MaCh3 MCMC fitter marginalizes over all nuisance parameters from both detector likelihoods and samples the oscillation parameter space to construct a posterior probability density function, which is interpreted using Bayesian methods. Images taken from [8].

In the first approach, the BANFF near detector utilizes two different fitters: GUNDAM for the near detector data and P-Theta for the far-detector data. Firstly, GUNDAM minimizes a χ^2 by following the gradient (exploiting the gradient descent algorithm depicted in Figure 3.2(a)) to find the parameter set that best predicts the data in the Monte Carlo simulation. Once the minimum is located, the covariance matrix for the ND280 parameters is computed from the inverse of the Hessian matrix, as explained in section 3.3. After marginalizing over the ND280 parameters, this covariance matrix is passed to the far-detector fitter P-theta, which marginalizes over all parameters except the oscillation parameters and perform a grid search over the reduced likelihood surface to determine the best-fit values of the parameters of interest.

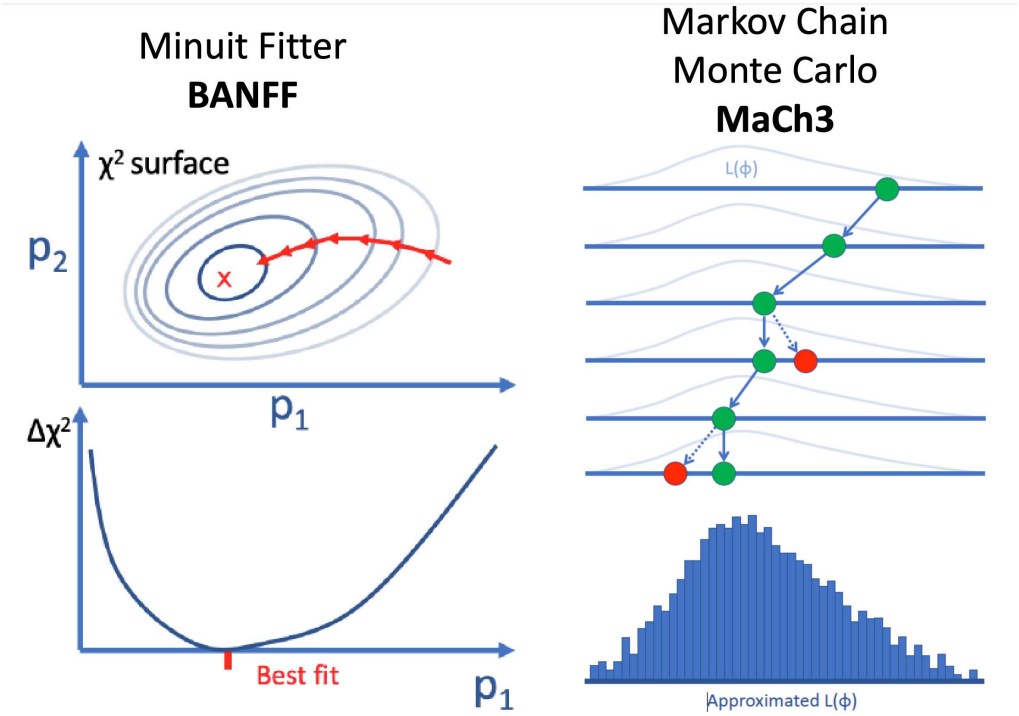

Figure 3.2: Two simplified diagrams illustrating the workings of gradient descent and MCMC methods in navigating the likelihood surface and parameter space. (a) The gradient descent algorithm incrementally moves across the likelihood surface, reducing χ^2 values as it seeks the minimum. By normalizing the likelihood and subtracting the minimum χ^2, $\Delta\chi^2$ contours are shown for two parameters, p_1 and p_2. These contours can be profiled or marginalized to yield a one-dimensional $\Delta\chi^2$ for each parameter. The best-fit point is the lowest value found, and uncertainties are either derived from the Hessian or from identifying the parameter values corresponding to a $\Delta\chi^2$ equal to the 68% or 1σ interval. (b) The MCMC method steps through the parameter space based on the likelihood, gradually constructing a posterior probability distribution by sampling parameter ϕ while marginalizing over other parameters. Green dots represent accepted values of ϕ, and red dots indicate rejected values. Images taken from [8].

In the second approach, the MaCh3 fitter uses a Markov Chain Monte Carlo (MCMC) method (depicted in the illustation in Figure 3.2(b)) to step semi-randomly through the entire parameter space of both the ND280 and Super-Kamiokande likelihoods. This generates a posterior probability density function, from which the posterior probabilities of the oscillation parameters are derived through marginalization. The main difference with respect to is that MaCh3 provides a joint fit of both near and far detector data.

3.2 Bayesian vs Frequentist approach

Statistics can be categorized into two main approaches: Bayesian and frequentist. Each approach addresses different inquiries, and while they yield similar metrics and values, it is crucial to grasp the distinctions in their interpretations to fully understand the results.

Bayesian statistics focuses on quantifying degrees of belief regarding a system based on prior information. For example, if a coin is assumed to be fair, the probability of landing heads or tails would be considered equal, up to a certain level of confidence. This belief is represented by a prior probability distribution that encapsulates the uncertainty about the coin's fairness. After observing outcomes, the prior distribution is updated, producing a posterior probability distribution that reflects both the initial belief and the new data. As more data is gathered, the posterior distribution adjusts, possibly shifting away from the initial assumption. In the context of the T2K oscillation analysis, the Bayesian analysis is perfomed by MaCh3, therefore, it is essential to assess possible dependencies of the result from the choice of the prior.

In contrast, frequentist statistics defines probabilities based on the frequency of events over a large number of trials. For instance, the probability of landing heads would be determined by flipping the coin multiple times and calculating the fraction of heads observed. This approach does not incorporate prior beliefs or assumptions about the outcome and instead relies solely on experimental data. The frequentist method is empirical, and probabilities emerge from the relative frequencies of outcomes over repeated trials. In the T2K oscillation analysis, the BANFF framework adopts this frequentist approach, where the oscillation parameters are inferred directly from the data without incorporating prior distributions.

3.3 The likelihood function

The likelihood function can be visualized as a multi-dimensional surface with the number of dimensions given by the number of model parameters. The likelihood quantifies how well a model's predictions align with the observed data for various parameter combinations. This function is often derived by comparing the model's

predictions to the data, with a commonly used metric being the chi-squared per degree of freedom (χ^2/DoF).

In particle physics, experiments frequently involve counting discrete events, where each event behaves as an independent random variable. For a basic counting experiment, the Poisson distribution describes the probability of observing k events, given that the model predicts λ events:

$$p(k|\lambda) = \frac{\lambda^k e^{-\lambda}}{k!}$$

Here, λ represents the expected number of events according to the model, which depends on a set of parameters θ. In practice, most physical experiments involve more intricate datasets that cannot be fully represented by a single value. To address this, the likelihood function is generalized to account for a series of observations, such as binned data from a measured variable or observable. These bins may correspond to continuous quantities, like an energy spectrum, or distinct categories, such as different topological classifications within the experiment, divided into N observable bins.

For a set of N bins, the likelihood L for observing k_i events in the i-th bin, given an expected number of events λ_i, is given by the product of Poisson probabilities across all bins:

$$L = \prod_{i=1}^{N} \frac{\lambda_i^{k_i} e^{-\lambda_i}}{k_i!}$$

Here, the event predictions λ_i are functions of a shared set of parameters, denoted as θ.

Although this likelihood is unnormalized, certain terms cancel out when it is divided by the likelihood corresponding to the nominal parameter set. This yields the expression for the relative likelihood, also known as the likelihood ratio:

$$\mathcal{L}_{\text{ratio}} = \prod_{i=1}^{N} \frac{\lambda_i^{k_i} e^{-\lambda_i} \times k_i!}{k_i^{k_i} e^{-k_i} \times \lambda_i!}$$

From the relation between the Poisson likelihood and the chi-squared statistic, $-2\ln\mathcal{L} = \chi^2$, the difference in χ^2 between a general parameter set and the nominal one can be expressed as:

$$\Delta\chi^2 = \sum_{i=1}^{N} 2\left(\lambda_i - k_i + k_i \ln \frac{k_i}{\lambda_i}\right)$$

This formulation can be easily computed in the context of binned likelihood analyses.

In some situations, particularly with limited statistics, it may be preferable to use an unbinned likelihood approach. In such cases, a function is used to estimate the probability distribution and normalize the data. While a frequentist approach typically does not consider prior uncertainties, additional constraints on parameters, $p(\theta)$, can be included as penalty terms in the likelihood ratio, resulting in:

$$\mathcal{L}_{\text{ratio}} = \frac{\pi(\vec{\theta})}{\pi(\vec{\theta}_{\text{nom}})} \times \prod_{i=1}^{N} \frac{\lambda_i^{k_i} e^{-\lambda_i} \times k_i!}{k_i^{k_i} e^{-k_i} \times \lambda_i!}$$

If the priors are Gaussian, with Gaussian covariances, they take the form:

$$p(\theta) = \frac{1}{(2\pi)^{k/2}|V_\theta|^{1/2}} \exp\left(-\frac{1}{2}\Delta\theta^T V_\theta^{-1} \Delta\theta\right)$$

where V_θ represents the prior covariance matrix. The inclusion of penalty terms ensures that the minimization of $\Delta\chi^2$ does not lead to parameter values that stray more than a few standard deviations from their nominal or prior central values.

Taking the logarithm of the likelihood ratio results in a more comprehensive expression for $-2\ln\mathcal{L}_{\text{ratio}}$, which is calculated by summing the covariances of the parameters p and q across the total number of parameters N_{pars}:

$$\Delta\chi^2 = 2\sum_{i=1}^{N}\left(\lambda_i(\vec{\theta}) - k_i + k_i \ln \frac{k_i}{\lambda_i(\vec{\theta})}\right) + \sum_{p=1}^{N_{\text{pars}}}\sum_{q=1}^{N_{\text{pars}}} \Delta\theta_p V_\theta^{-1} \Delta\theta_q$$

This formulation holds when the prior distributions of the parameters are roughly Gaussian. When this is the case, the prior distributions can be approximated by quadratic functions near the minimum of the χ^2 surface, referred to as χ^2_{min}. As a result, the likelihood ratio can be redefined concerning the most likely set of parameters, and the variation in χ^2, $\Delta\chi^2$, can be expressed as:

$$\Delta\chi^2 = \sum_{p=1}^{N_{\text{pars}}} \sum_{q=1}^{N_{\text{pars}}} \frac{\partial^2 \Delta\chi^2(\vec{q}_{\text{min}})}{\partial q_p \partial q_q} (q_p - q_{\text{min},p})(q_q - q_{\text{min},q})$$

where $\vec{q}$ represents all of the parameters, and $\vec{q}_{\text{min}}$ are their values at the minimum of the χ^2 surface, χ^2_{min}.

The Hessian matrix, which is defined as:

$$H_{pq} = \frac{\partial^2 \Delta\chi^2}{\partial q_p \partial q_q}$$

can subsequently be inverted to obtain the covariance matrix at the best-fit point.

3.4 Bayesian approach

A brief overview of the Bayesian approach as implemented in the MaCh3 framework is provided.

In Bayesian formalism, probability is interpreted as the degree of confidence in the validity of a hypothesis. This confidence level is informed by both the likelihood of observing the data and the prior knowledge of the model. Accordingly, Bayes' theorem expresses the posterior probability as

$$P(H|\{D\}, I) = \frac{P(\{D\}|H, I) \times P(H|I)}{P(\{D\}|I)} \tag{3.1}$$

where $P(H|\{D\}, I)$ is the posterior probability distribution, representing our belief in the hypothesis H given the data $\{D\}$ and any prior information I. The term $P(\{D\}|H, I)$, is the likelihood, already introduced, which represents the probability of observing the data given the hypothesis. $P(H|I)$ is the prior probability of the hypothesis based on any prior knowledge or information I, and $P(\{D\}|I)$ represents the total probability of the data, which serves as a normalization factor.

Since $P(\{\text{D}\}|I)$ is just a normalizing constant, Bayes' theorem can be rewritten as

$$P(H|\{D\}, I) \propto P(\{D\}|H, I) \times P(H|I) \tag{3.2}$$

In T2K, the hypothesis H is the predicted number of neutrino events observed at the near and far detectors. while the likelihood is often simply written as

$\exp(-\mathrm{X}^2/2)$.

3.4.1 Defining the T2K likelihood

To simplify the computation of the likelihood function, the negative log-likelihood is utilized. In the Bayesian framework, The T2K negative log-likelihood, with the ND280 and SK data split into energy bins, can be expressed as [37]:

$$
\begin{aligned}
-\ln(\mathcal{L}) = & \sum_{i}^{\text{ND280 bins}} N^{\text{ND}}_{\text{MC},i}(\vec{b},\vec{x},\vec{d}) - N^{\text{ND}}_{\text{Data},i} + N^{\text{ND}}_{\text{Data},i} \ln\left(\frac{N^{\text{ND}}_{\text{Data},i}}{N^{\text{ND}}_{\text{MC},i}(\vec{b},\vec{x},\vec{d})}\right) + \frac{(\beta_i - 1)^2}{2\sigma^2_{\beta_i}} \\
& + \sum_{i}^{\text{SK bins}} N^{\text{SK}}_{\text{MC},i}(\vec{b},\vec{x},s\vec{k}d,\vec{o}) - N^{\text{SK}}_{\text{Data},i} + N^{\text{SK}}_{\text{Data},i} \ln\left(\frac{N^{\text{SK}}_{\text{Data},i}}{N^{\text{SK}}_{\text{MC},i}(\vec{b},\vec{x},s\vec{k}d,\vec{o})}\right) \\
& + \frac{1}{2}\sum_{i}^{\text{osc}}\sum_{j}^{\text{osc}} \Delta\mathrm{o}_i (V_o^{-1})_{i.j} \Delta o_j \\
& + \frac{1}{2}\sum_{i}^{E_\nu\text{bins}}\sum_{j}^{E_\nu\text{bins}} \Delta\mathrm{b}_i (V_b^{-1})_{i.j} \Delta b_j \\
& + \frac{1}{2}\sum_{i}^{\text{xsecpars}}\sum_{j}^{\text{xsecpars}} \Delta\mathrm{x}_i (V_x^{-1})_{i.j} \Delta x_j \\
& + \frac{1}{2}\sum_{i}^{\text{ND280det}}\sum_{j}^{\text{ND280det}} \Delta\mathrm{d}_i (V_d^{-1})_{i.j} \Delta d_j \\
& + \frac{1}{2}\sum_{i}^{\text{SKdet}}\sum_{j}^{\text{SKdet}} \Delta\mathrm{skd}_i (V_{skd}^{-1})_{i.j} \Delta skd_j
\end{aligned}
\tag{3.3}
$$

where V_{ij} represents covariance or fractional covariance matrices constraining systematic parameters with Gaussian priors, labeled as follows: b for flux, x for cross section, d for the ND280 detector, skd for the SK detector, and o for oscillation.

Furthermore, $N_{ND,p}$ and $N_{SK,p}$ denote the number of predicted events (from the Monte Carlo simulations) in a specific bin for ND280 and SK, respectively, while $N_{ND,d}$ and $N_{SK,d}$ represent the number of observed data events.

3.4.2 Markov Chain Monte Carlo (MCMC) Technique

A Markov chain [38] is a stochastic process where the probability of transitioning from one state to another depends only on the current state, and not on the sequence of events that preceded it. The behavior of a Markov chain is governed by a transition matrix that defines the probabilities of moving between states.

Over time, if the chain satisfies certain conditions, it reaches a stationary distribution, which means that it that remains unchanged as the system evolves.

For a Markov chain to reach this stationary state, it must be ergodic, meaning that it is both irreducible (every state can be reached from any other state) and aperiodic (the chain does not get trapped in cycles). In an ergodic Markov chain, the long-term behavior is independent of the starting state, and the stationary distribution represents the equilibrium distribution of the system. This ensures that, after a sufficient number of steps, the system will spend a proportion of time in each state according to the stationary distribution. The chain is also reversible if, for any two states, the probability of transitioning from one to the other is equal to the probability of transitioning in the reverse direction, given the stationary distribution. This property, known as detailed balance, guarantees that the system is in equilibrium and that the stationary distribution accurately represents the underlying process.

Building on the Bayesian approach outlined above, the Markov Chain Monte Carlo (MCMC) technique is widely used to sample from the posterior distribution $P(H|\{D\}, I)$. Since computing this distribution analytically is often impractical, MCMC provides an efficient numerical method to explore complex, high-dimensional parameter spaces by generating a sequence of samples from the posterior distribution.

MCMC operates by constructing a Markov chain whose equilibrium distribution corresponds to the desired posterior distribution. The algorithm performs a guided random walk through the parameter space, with each step determined by the likelihood of the current position in the space. The probability of moving in a particular direction depends on how likely different points in the parameter space are, based on the data and the model.

The resulting sequence of steps, or samples, is distributed according to the posterior distribution. These samples are then used to estimate various statistical properties, such as the mean, variance, or credible intervals for the model parame-

ters.

One of the main advantages of MCMC is its ability to efficiently explore complex parameter spaces, automatically accounting for nuisance parameters. This is particularly valuable when dealing with models that have many parameters, where marginalizing over these parameters analytically would be computationally difficult. MCMC is also widely used in Bayesian inference for evaluating the normalization factor $P(\{D\}|I)$ in Bayes' theorem, which often requires solving multi-dimensional integrals that are otherwise intractable.

4 Analysis

4.1 Inputs of the analysis: Minituples Run11

The following analysis aims to study the resolution of several variables of interest, such as neutrino energy, momentum and lepton angle in the Monte Carlo simulations used for the T2K oscillation analysis at the far detector. The input data for this study are the so-called Minituples Run11 [1], which were derived from those provided by the T2K-SK group and separated by sample categories. In particular, the T2K sample selection classifies events based on the number and type of reconstructed Cherenkov rings in the Super-Kamiokande detector. 1Rμ and 1Re events correspond to events with a single reconstructed Cherenkov ring, where 1Rμ indicates a muon-like ring and 1Re represents an electron-like ring. The distinction between muon-like rings and electron-like rings arises from the output of the particle identification (PID) classifier, which analyzes the shape of the rings. Muon-like rings are generally sharper, while electron-like rings tend to appear more diffuse due to multiple scattering effects. The 1Rμ topology is the most aboundant, and it is mainly associated with charged-current quasi-elastic (CCQE) interactions.

In addition to these, more complex event types are identified. 1Re + 1 delayed electron (1Re + de) events contain a primary electron-like ring accompanied by a

[1] Run11 corresponds to the data analyzed by the T2K experiment in 2023.

delayed electron ring, which is typically produced by the decay of a muon (known as a Michel electron). This indicates that a muon was created in the interaction but decayed to an electron before being detected. These events are often used to tag interactions involving the production of a charged pion (π^+) in addition to the electron. The pion decays into a muon ($\pi^+ \to \mu^+ + \nu_\mu$), and the muon subsequently decays into a Michel electron ($\mu^+ \to e^+ + \nu_e + \bar{\nu}_\mu$).

For interactions involving multiple particles, more intricate topologies are observed. Multi-ring $\mu + 1$ delayed electron (multi-Rμ + 1de) events are characterized by multiple Cherenkov rings from muons and other particles, along with a delayed electron ring, signaling the decay of a muon. Similarly, multi-ring $\mu + 2$ delayed electrons (multi-Rμ + 2de) events feature multiple rings and two delayed electron rings, indicating that multiple muons were produced and subsequently decayed to electrons.

These samples are identified by the variable `iclass`, which can take on the values listed in Table 4.1. Appendix A.1 contains a complete list of files used in this analysis, sorted by the `iclass` values and horn current modes.

Table 4.1: Values and descriptions of the variable `iclass`. It identifies the different samples taken into account in the OA (oscillation analysis).

iclass	**sample**
11	1R e-like
13	1R μ-like
14	1R e-like with 1 delayed-e
31	Multi-ring μ-like with 1 delayed-e
32	Multi-ring μ-like with 2 delayed-e

The simulations are categorized by both the current mode and the `iclass` variable, resulting in a total of seven distinct samples: the 1Re-like and 1Rμ-like samples, each in both ν-mode (FHC) and $\bar{\nu}$-mode (RHC). Additionally, there are the categories 1Re + 1de, MultiRμ + 1de, MultiRμ + 2de in ν-mode. These samples, along with all background contributions, are summarized in Table 4.2.

Table 4.2: Summary of the samples categories considered in this analysis: the 1Rμ and 1Re samples are collected in both ν-mode (FHC) and $\bar{\nu}$-mode (RHC), while the remaning samples are only collected in FHC mode.

sample	**mode**	**osc channel**	**background contributions**				
1Rμ	FHC	$\nu_\mu \to \nu_\mu$	$\nu_\mu \to \nu_e$	$\nu_e \to \nu_e$	$\bar{\nu}_\mu \to \bar{\nu}_\mu$	$\bar{\nu}_\mu \to \bar{\nu}_e$	$\bar{\nu}_e \to \bar{\nu}_e$
	RHC	$\bar{\nu}_\mu \to \bar{\nu}_\mu$	$\nu_\mu \to \nu_e$	$\nu_e \to \nu_e$	$\nu_\mu \to \nu_\mu$	$\bar{\nu}_\mu \to \bar{\nu}_e$	$\bar{\nu}_e \to \bar{\nu}_e$
1Re	FHC	$\nu_\mu \to \nu_\mathrm{e}$	$\nu_\mu \to \nu_\mu$	$\nu_e \to \nu_e$	$\bar{\nu}_\mu \to \bar{\nu}_\mu$	$\bar{\nu}_\mu \to \bar{\nu}_e$	$\bar{\nu}_e \to \bar{\nu}_e$
	RHC	$\bar{\nu}_\mu \to \bar{\nu}_e$	$\nu_\mu \to \nu_\mu$	$\nu_e \to \nu_e$	$\bar{\nu}_\mu \to \bar{\nu}_\mu$	$\nu_\mu \to \nu_\mathrm{e}$	$\bar{\nu}_e \to \bar{\nu}_e$
1Re + 1de	FHC	$\nu_\mu \to \nu_\mu$	$\nu_\mu \to \nu_e$	$\nu_e \to \nu_e$	$\bar{\nu}_\mu \to \bar{\nu}_\mu$	$\bar{\nu}_\mu \to \bar{\nu}_e$	$\bar{\nu}_e \to \bar{\nu}_e$
MultiRμ + 1de	FHC	$\nu_\mu \to \nu_\mu$	$\nu_\mu \to \nu_e$	$\nu_e \to \nu_e$	$\bar{\nu}_\mu \to \bar{\nu}_\mu$	$\bar{\nu}_\mu \to \bar{\nu}_e$	$\bar{\nu}_e \to \bar{\nu}_e$
MultiRμ + 2de	FHC	$\nu_\mu \to \nu_\mu$	$\nu_\mu \to \nu_e$	$\nu_e \to \nu_e$	$\bar{\nu}_\mu \to \bar{\nu}_\mu$	$\bar{\nu}_\mu \to \bar{\nu}_e$	$\bar{\nu}_e \to \bar{\nu}_e$

There are a total of 1486742 MC simulations. Table 4.3 provides the amount for each sample and its ratio with respect to the total. The contributions of the background due to the beam contaminations have been included.

Table 4.3: Amount (absolute and relative) of the Minituple run11 samples including the background to the primary contributions.

	1Rμ		**1Re**		**1Re +1de**	**MultiRμ + 1de**	**MultiRμ + 2de**
	FHC	RHC	FHC	RHC	FHC	FHC	FHC
Counts	593745	574871	102917	103088	12295	51989	47837
Ratio to total	0.399	0.387	0.069	0.069	0.008	0.035	0.032

Table 4.4 reports the ratios of the different six contributions to each sample providing a detailed breakdown sorted by sample category.

Table 4.4: Ratios of the different contributions to each sample. The main contribution for each sample is highlighted in green. For 1Rμ samples, the main contributions are from the $\nu_\mu \rightarrow \nu_\mu$ and $\bar{\nu}_\mu \rightarrow \bar{\nu}_\mu$ beams. In the FHC channels (ν mode), the $\bar{\nu}_\mu \rightarrow \bar{\nu}_\mu$ beam is the background, whereas in the RHC channels ($\bar{\nu}$ mode), the background is the $\nu_\mu \rightarrow \nu_\mu$ beam. For electron ring samples, the contributions are more spread across different channels, with the main ones being $\nu_\mu \rightarrow \nu_e$ and $\bar{\nu}_\mu \rightarrow \bar{\nu}_e$.

sample	mode	$\nu_\mu \rightarrow \nu_\mu$	$\nu_\mu \rightarrow \nu_e$	$\nu_e \rightarrow \nu_e$	$\bar{\nu}_\mu \rightarrow \bar{\nu}_\mu$	$\bar{\nu}_\mu \rightarrow \bar{\nu}_e$	$\bar{\nu}_e \rightarrow \bar{\nu}_e$
1Rμ	FHC	0.537	0.001	0.001	0.458	0.001	0.001
	RHC	0.343	0.001	0.001	0.652	0.001	0.001
1Re	FHC	0.017	0.425	0.202	0.020	0.203	0.134
	RHC	0.017	0.199	0.139	0.017	0.425	0.204
1Re + 1de	FHC	0.040	0.568	0.313	0.035	0.024	0.020
MultiRμ + 1de	FHC	0.280	0.704	0.003	0.003	0.005	0.004
MultiRμ + 2de	FHC	0.832	0.159	0.001	0.002	0.003	0.003

The details above can also be observed in Figure 4.1.

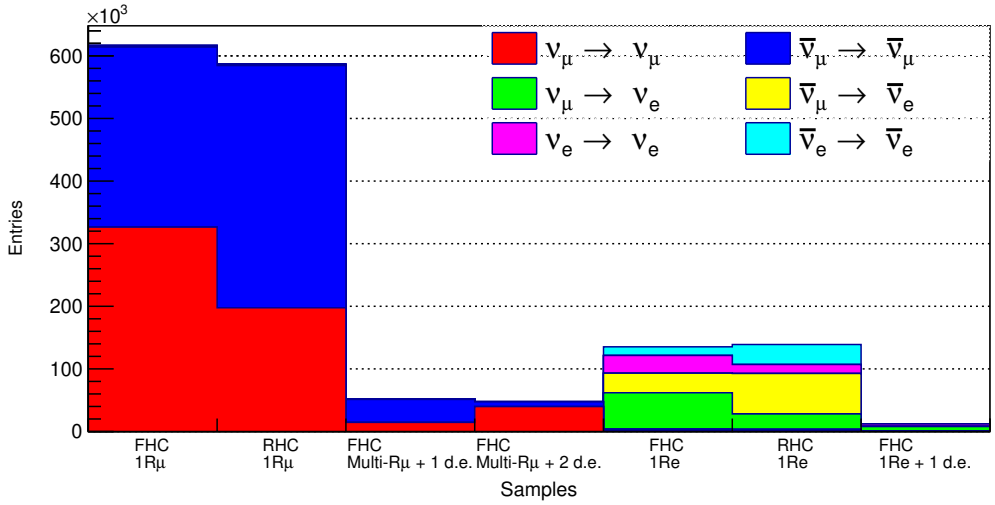

Figure 4.1: Distributions of the different sample selections, with each sample stacked across the six different channels taken into account. In addition to the information described in Table 4.4, it is evident that the amount of unoscillated samples for FHC and RHC 1Rμ are significantly higher than those for the other channels, while the FHC 1Re + 1de channel is the least populated.

4.1.1 Variables of Interest

The neutrino energy, as well as the lepton angle and momentum resolution from the samples described above, was studied in the following analysis to provide insights to the optimal binning for these variables. This was achieved by comparing the true values with the reconstructed values.

Starting from the minituple variables, I performed specific computations to obtain all the necessary quantities, depending on the sample. Table 4.5 lists all the considered variables along with their descriptions, while the procedures for computing the true and reconstructed lepton momentum and angle are detailed in Appendix A.2.

All the analysis was done within the `ROOT CERN` framework [39], as all the MC simulations were stored in `TTree`s, with different variables stored in separate `TBranche`s.

As previously observed in Table 4.1, sample types are categorized by the `iclass` variable. Additionally, the number of rings for each event is in the `nrings` branch, while the interaction modes are stored in the `mode` branch, whereas the `fqwall` and `fqtowall` branches contain respectively the distance from the event vertex to its closest point on the detector walls and the distance from the event vertex to the detector wall along the track direction. Moreover, the true and reconstructed neutrino energy are stored respectively in the branches `pnu[0]` and `erec`, while the true and reconstructed neutrino momentum and lepton angle must be retrieved from other variables following the procedure reported in Appendix A.2.

4.1.2 Cuts and Constraints

The following cuts were applied in the analysis to all the samples with the aim of reproducing the selection performed in [9]:

- `erec` > 0, in order to discard some unwanted output with negative reconstructed energy;
- For the μ-like samples
  - `fqtowall` > 250 cm;
  - `fqwall` > 50 cm;

Table 4.5: Name and description of the TBranches used in this analysis.

TBranch	Description
iclass	sample type
nrings	number of rings of the event
mode	true neutrino interaction mode
fqwall	distance from the event vertex to its closest point on the detector walls (in cm)
fqtowall	distance from the event vertex to the detector wall along the track direction (in cm)
pnu[0]	true neutrino energy in GeV
erec	reconstructed energy in MeV
fq1rmom[0][i]	lepton momenta of a single-ring event, where i = 1 for muons and i = 2 for electrons
fq1rdir[0][i]	lepton direction of a single-ring event, where i = 1 for muons and i = 2 for electrons
fqmrmom[fit_index][ith_ring]	lepton momenta assuming a particular multi-ring fit denoted by fit_index and assuming ith_ring is the lepton

- for the e-like samples without a delayed electron
  - fqtowall > 170 cm;
  - fqwall > 80 cm;

- for e-like samples with one delayed electron
  - fqtowall > 270 cm;
  - fqwall > 50 cm.

The cuts listed above are illustrated in Figure 4.2.

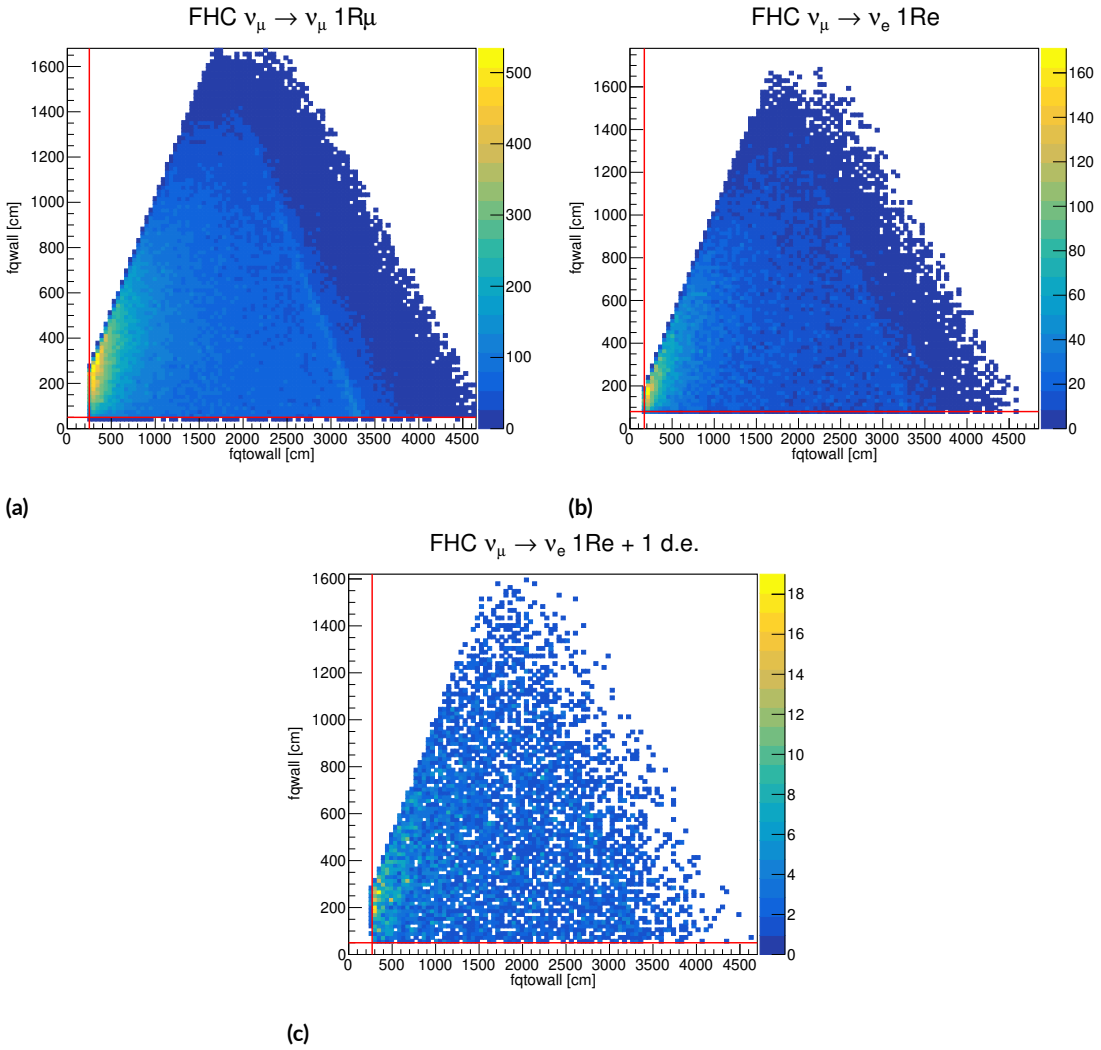

Figure 4.2: Scatter plots for `fqwall` versus `fqtowall`. The former is the distance to the detector wall while the latter is the detector's nearest boundary along the track direction. For the μ-like samples, a minimum distance of 50 cm for `fqwall` and 250 cm for `fqtowall` is required (a). For the e-like samples without a decay electron, the cuts were set to `fqwall` > 80 cm and `fqtowall` > 170 cm (b). In contrast, for e-like samples with one delayed electron, the requirements were `fqwall` > 50 cm and `fqtowall` > 270 cm (c). The constrains are highlighed in red.

4.2 Reconstructed energy E_ν^{rec}

The reconstructed neutrino energy E_ν^{rec} is estimated from final-state charged-lepton kinematics as

$$\mathrm{E}_\nu^{rec}(p_l, \theta_l) = \frac{2M_{N,i}E_l - M_l^2 + M_{N,f}^2 - M_{N,i}^2}{2(M_{N,i} - E_l + p_l \cos(\theta_l))} \tag{4.1}$$

where $M_{N,i}$, $M_{N,f}$, and M_l are the mass of the initial-state nucleon, final-state nucleon, and final-state charged lepton, respectively; E_l, p_l, and θ_l are the energy, three-momentum, and angle of the final-state charged lepton, respectively [9].

For the CC-0π samples (i.e. the FHC and RHC 1Rμ and 1Re) it is assumed that the event was a CCQE interaction on a stationary bound nucleon (assumed to be a neutron). Therefore 4.1 becomes [37]

$$\mathrm{E}_\nu^{rec}(p_l, \theta_l) = \frac{(m_n - E_b)E_l - m_l^2/2 + m_n E_b - E_b^2/2 + (m_p^2 - m_n^2)/2}{m_n - E_b - E_l + p_l \cos(\theta_l)} \tag{4.2}$$

where m_p, m_n, and m_l are the proton, neutron, and lepton masses respectively,

For the CC-1π+ samples the quasi-elastic assumption is not valid. In this case it is assumed that the outgoing baryon is a Δ^{++} resonance instead of a proton. The formula for the reconstructed neutrino energy becomes

$$\mathrm{E}_\nu^{rec}(p_l, \theta_l) = \frac{2m_p E_l - m_l^2 + m_{\Delta^{++}}^2 - m_p^2}{2(m_p - E_l + p_l \cos(\theta_l))} \tag{4.3}$$

where $m_{\Delta^{++}}$ is the Δ^{++} resonance mass.

The assumptions made are consistent with the fact that in the CC-0π samples, the majority of events are CCQE interactions, while in the CC-1π+ samples, the majority of events are Δ^{++} resonances.

Some examples are shown in 4.3 where the energy reconstructed spectra of different samples are plotted, highlighting the contribution of each interaction. It is evident that for the 1Rμ and 1Re samples, there is a predominance of CCQE events (in blue), whereas for the 1Re + 1de and for the multiRing-μ examples, the main contribution is the Δ^{++} resonance (in green).

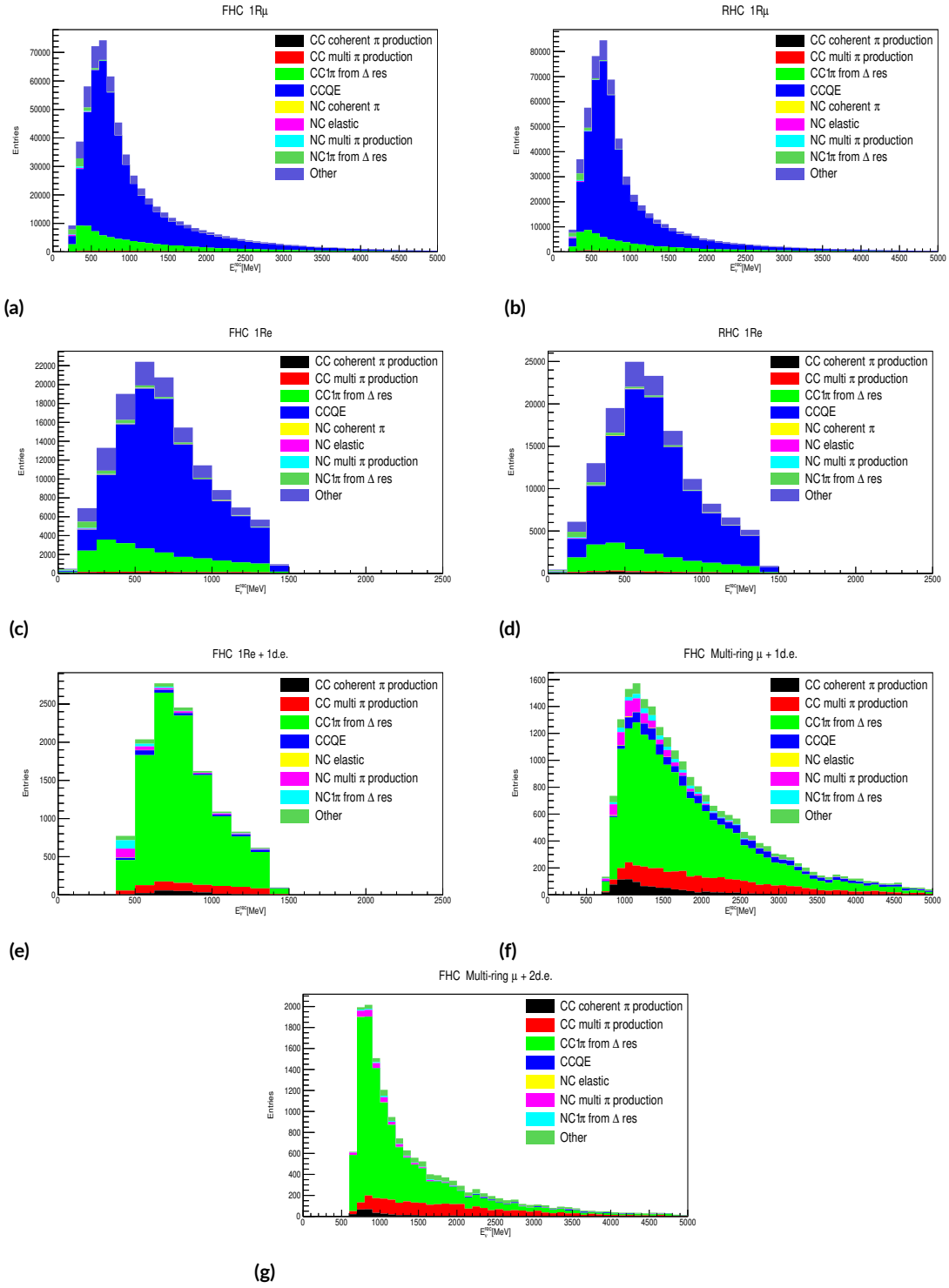

Figure 4.3: Stacked histograms of `erec` spectra, where the contribution of different interaction modes has been highlighted. It's evident that for CC-0π samples (a, b, c, d), the main contribution is from the CCQE interaction, while for CC-0π samples, the main contribution is from the Δ^{++} interaction.

In the plot above it also visible that two different binning were used for the electron and muon rings events. The binning choice is the one used in [9]:

- **Binning for μ rings events**: 0, 100, 200, 300, 400, 500, 600, 700, 800, 900, 1000, 1100, 1200, 1300, 1400, 1500, 1600, 1700, 1800, 1900, 2000, 2100, 2200, 2300, 2400, 2500, 2600, 2700, 2800, 2900, 3000.
- **Binning for electron rings events**: 0, 125, 250, 375, 500, 625, 750, 875, 1000, 1125, 1250.

4.2.1 Cross-check on the implementation of the formula

It was verified that using the variable `erec` or plugging the reconstructed momentum and angle in the previous formulas gave the same results.

In the histograms in Figure 4.4, the `erec` spectra were overlaid with those obtained through the formulas for the FHC 1Rμ (a) and FHC 1Re (b) samples, presented as examples. The ranges were extended to compare the hole spectra.

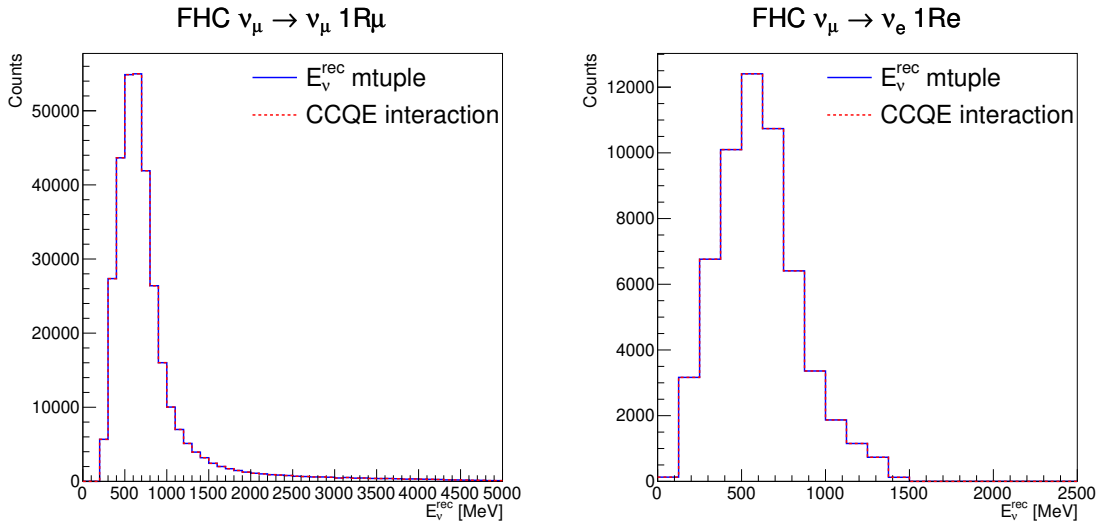

(a) (b)

Figure 4.4: Reconstructed neutrino energy for FHC 1Rμ (a) and FHC 1Re (b) samples. The spectra of the other samples, which are not reported, show a perfect match aswell.

The plots in Figures 4.4 show that there is a perfect match, this is true for all the other samples.

4.3 iso-E_ν^{rec} curves in the p_l and θ_l plane

The formula 4.1 shows that the reconstructed neutrino energy, E_ν^{rec}, is a function of the lepton angle, θ_l, and momentum, p_l. Consequently, E_ν^{rec} was analyzed in the p_l-θ_l plane. In particular, the iso-E_ν^{rec} curves were compared to the (p_l^{rec}, θ_l^{rec}) distribution. By superimposing the iso-E_ν^{rec} curves onto the (p_l^{rec}, θ_l^{rec}) distribution, one can observe how E_ν^{rec} varies across the (p_μ, θ_μ) plane, therefore visualizing the relationship between lepton kinematics and reconstructed neutrino energy.

This analysis considered both the complete (p_l^{rec}, $\theta_l{}^{rec}$) distribution and the grouping of data into bins of E_ν^{true}.

4.3.1 Overall (p_l, θ_l) distribution

Figure 4.5 shows an example for the FHC 1Rμ samples of the fact that $E_\nu^{\text{rec}}(p_\mu^{\text{rec}}$, $\theta_\mu^{\text{rec}})$ can be visualized in the (p_μ, θ_μ) space by plotting the iso-E_ν^{rec} curves over the (p_μ, θ_μ) distribution.

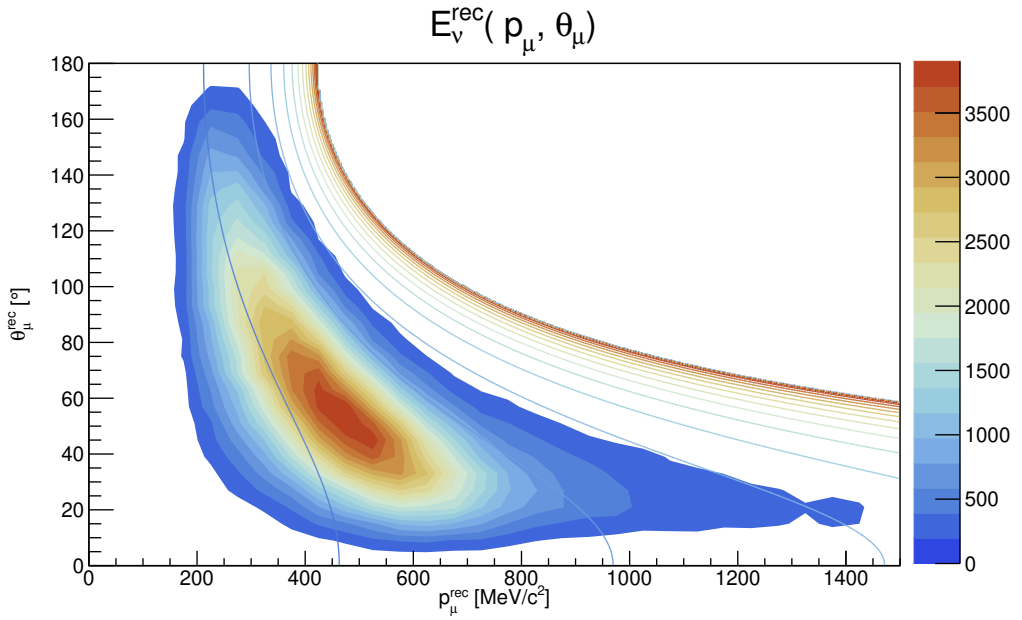

Figure 4.5: Lepton momentum and angle distribution overlaid with the iso-reconstructed neutrino energy (iso-E_ν^{rec}) curves for FHC 1R$_\mu$ samples. The color scale represents the density of events in the (p_μ^{rec}, θ_μ^{rec}) plane. The lines depict the iso-E_ν^{rec} curves, which divide the energy range from 0 to 7000 MeV into 14 intervals of 500 MeV each, with the color pattern indicating the corresponding energy value. E_ν^{rec} is computed using the formula 4.2.

It is visible how at a fixed E_ν^{rec} the angles and momenta of the lepton are very anti correlated, showing an hyperbolic curve.

The position on the simulated lepton variables with respect to isolines is determined basically by the T2K spectrum of the neutrino CC-interactions.

4.3.2 (p_l, θ_l) in bins of E_ν^{true}

For the FHC 1Rμ samples, true neutrino energy (E_ν^{true}) was divided into 30 equal bins, and the distribution of reconstructed muon momentum (p_μ^{rec}) and reconstructed muon angle (θ_μ^{rec}) was plotted. Overlaid on this distribution are the iso-E_ν^{rec} contours, which represent the reconstructed neutrino energy calculated from the kinematics of the outgoing muon.

It was observed that the points $(p_\mu^{\text{rec}}, \theta_\mu^{\text{rec}})$ closely follow the iso-E_ν^{rec} curves, with the agreement improving when analyzing only the CCQE sample, as expected. This is because for 1Rμ samples, the interaction is assumed to be a charged-current quasi-elastic (CCQE) interaction on a stationary bound nucleon, and the CCQE approximation formula (4.2) is used to compute the reconstructed neutrino energy.

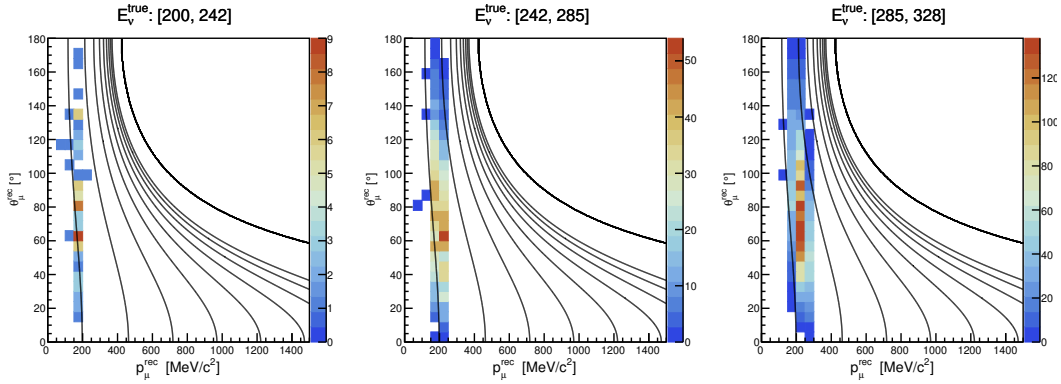

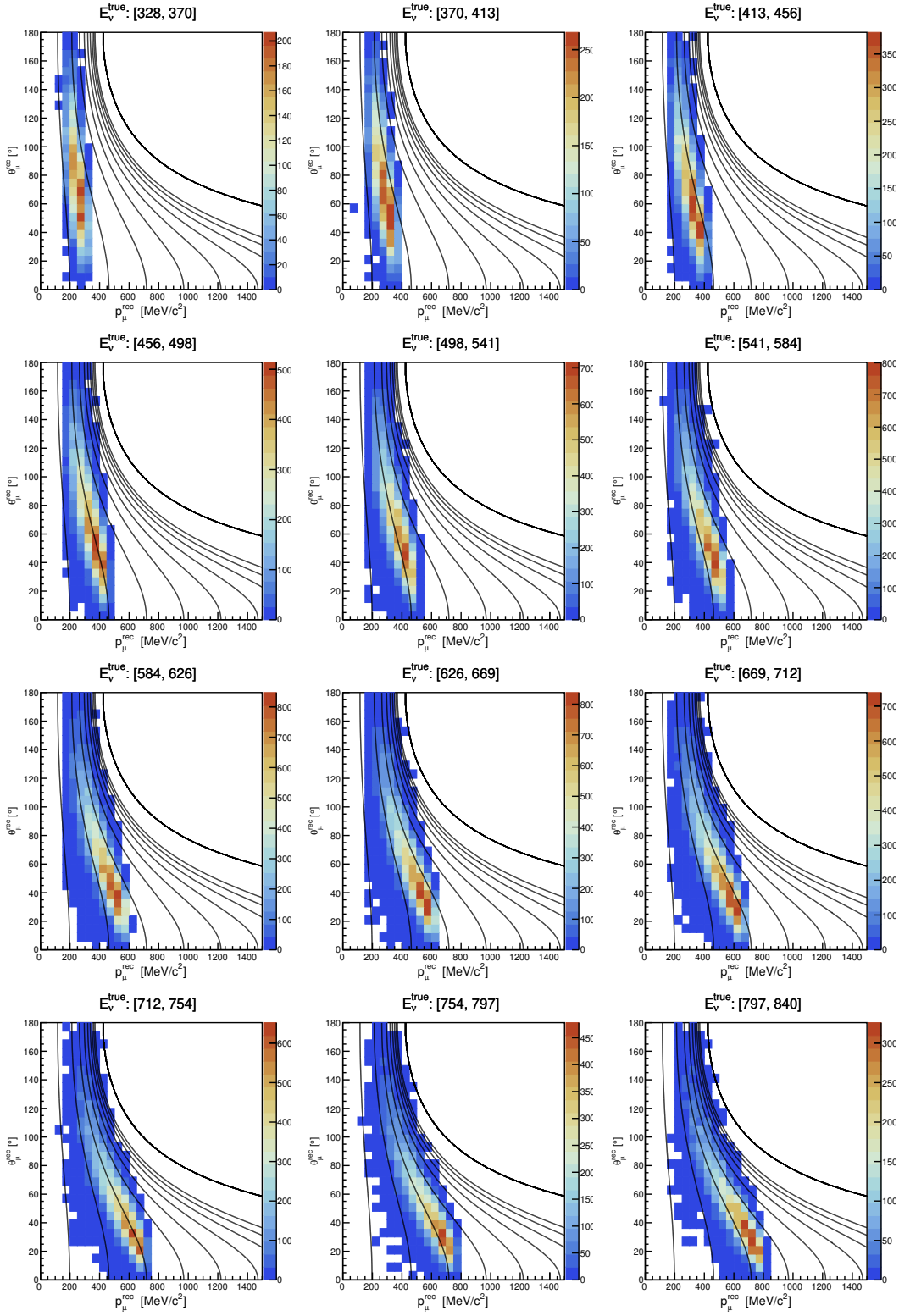
E_ν^{true}: [328, 370]
E_ν^{true}: [370, 413]
E_ν^{true}: [413, 456]
E_ν^{true}: [456, 498]
E_ν^{true}: [498, 541]
E_ν^{true}: [541, 584]
E_ν^{true}: [584, 626]
E_ν^{true}: [626, 669]
E_ν^{true}: [669, 712]
E_ν^{true}: [712, 754]
E_ν^{true}: [754, 797]
E_ν^{true}: [797, 840]
θ_μ^{rec} [°]
p_μ^{rec} [MeV/c^2]

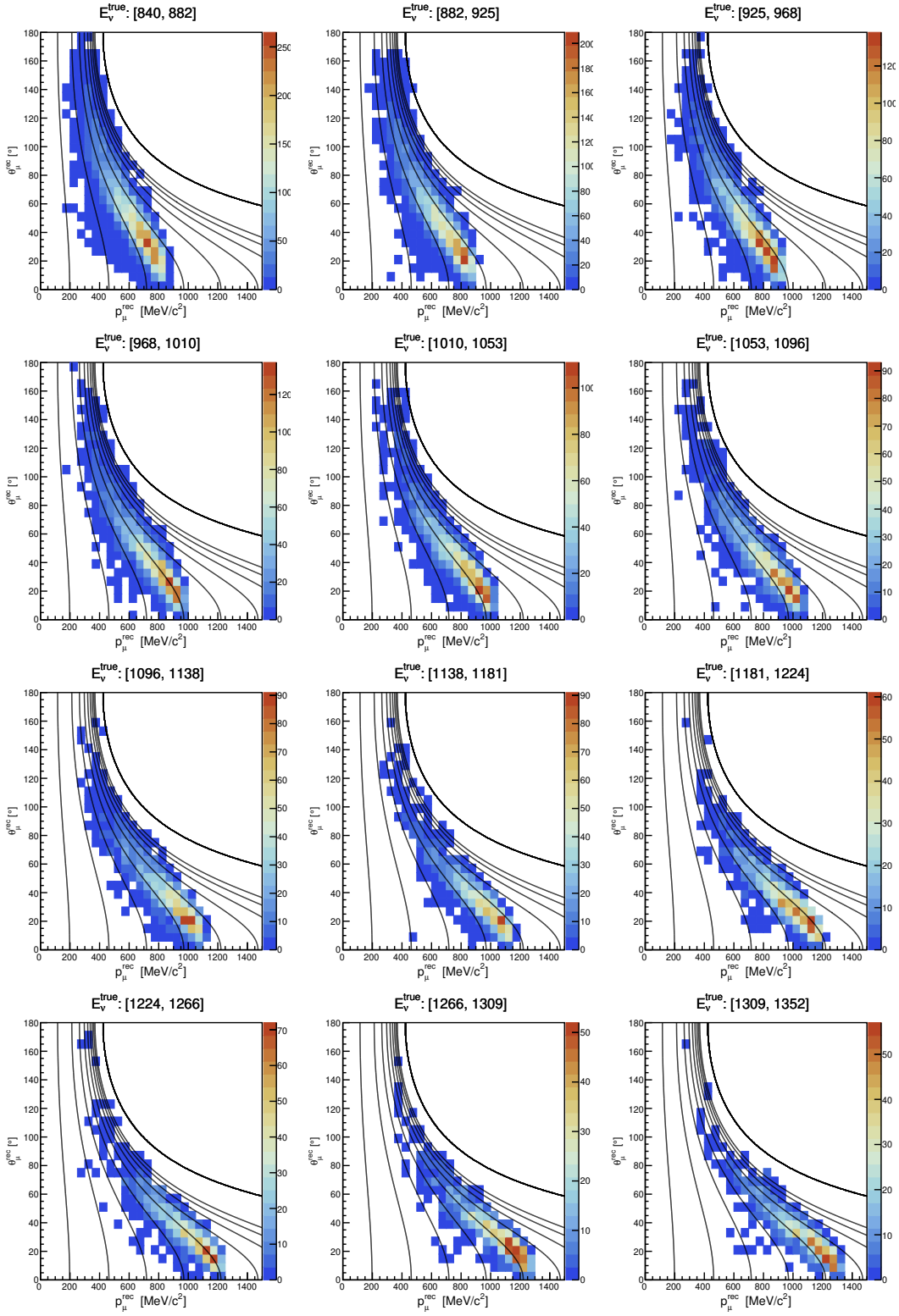
E_ν^{true}: [840, 882]
E_ν^{true}: [882, 925]
E_ν^{true}: [925, 968]
E_ν^{true}: [968, 1010]
E_ν^{true}: [1010, 1053]
E_ν^{true}: [1053, 1096]
E_ν^{true}: [1096, 1138]
E_ν^{true}: [1138, 1181]
E_ν^{true}: [1181, 1224]
E_ν^{true}: [1224, 1266]
E_ν^{true}: [1266, 1309]
E_ν^{true}: [1309, 1352]
θ_μ^{rec} [°]
p_μ^{rec} [MeV/c^2]

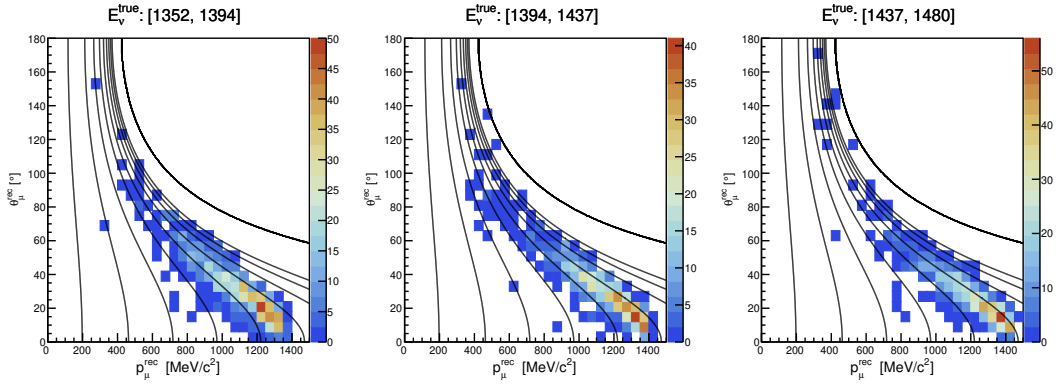

Figure 4.6: Event distribution in the $(p_\mu^{rec}, \theta_\mu^{rec})$ plane. The lines show iso-E_ν^{rec} curves, which were calculated using the CCQE approximation formula 4.2. The distribution of $(p_\mu^{rec}, \theta_\mu^{rec})$ points aligns well with these iso-E_ν^{rec} curves. In the figure only the FHC 1Rμ CCQE samples are selected.

In the selected sample, the events tend to align with the constant reconstructed energy curves, as anticipated. However, deviations and the broadening of these distributions arise also due to the fact that 4.2 is applied using the reconstructed values of p_μ and θ_μ, without accounting for nucleon motion within the nucleus, namely, the Fermi motion. This kinematic effect causes some smearing in the reconstructed energy, when considering p_μ and θ_μ at the true level and a monocromatic true neutrino energy. A final effect of broadening is due to the fact that it has been considered an interval in true neutrino energy for each plot. Overall, no evident problems or anomalies are observed relative to expectations.

4.4 Resolution and Bias study on p_l and θ_l in 2D

This section presents a resolution and bias study on p_l and θ_l.

- Points in an equispaced grid pattern from the p_l^{true} vs θ_l^{true} distribution were selected.
- For θ_l^{true}, the grid covers the range between 0 and 180°.
- For p_l^{true}, the range is 0 to 5000 MeV/c^2 for 1Rμ samples, and 0 to 1500 MeV/c^2 for 1Re samples.
- For 1Rμ samples, an interval equal to 1/10 of the distance between the grid points was used for sampling $(p_l^{rec}, \theta_l^{rec})$.

- For 1Re samples, a larger interval equal to 2/10 of the distance between the grid points was considered.

- The points $(p_l^{rec}, \theta_l^{rec})$ were then plotted in the p-θ plane to observe how scattered they were relative to the chosen intervals.

- A scan on the grid pattern size was perfomed, starting form 5×5 up to 50×50.

The results obtained are shown in Figure 4.7 and 4.12, for respectively the FHC 1Rμ and 1Re samples. In the plots, the bias is highlighed as a (rescaled) red arrow in the "island" plots.

4.4.1 Example for FHC 1Rμ

Only the results for the 5×5, 10×10, 20×20, and 40×40 grids are reported, respectively in Figure 4.8, 4.9, 4.10 and 4.11.

For islands with a size greater than 12 samples, the dispersion estimated as the RMS and the bias-calculated as the difference between the true value of the grid pattern and the mean of each island—are evaluated and displayed as a color bar on the z-axis.

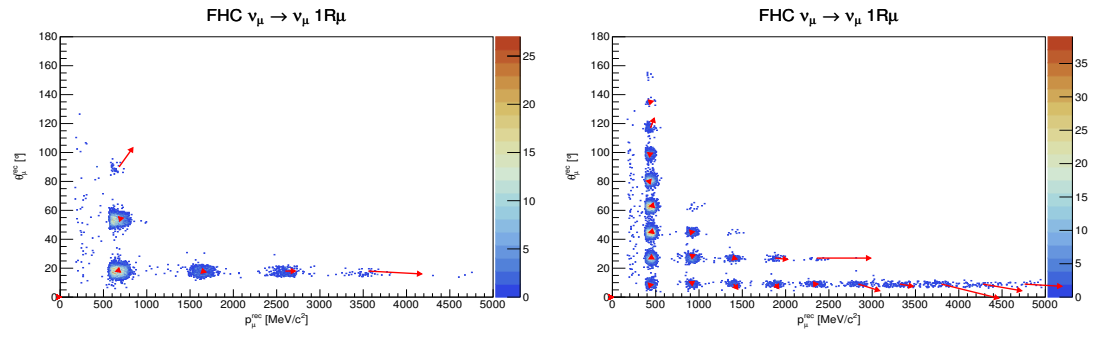

(a) (b)

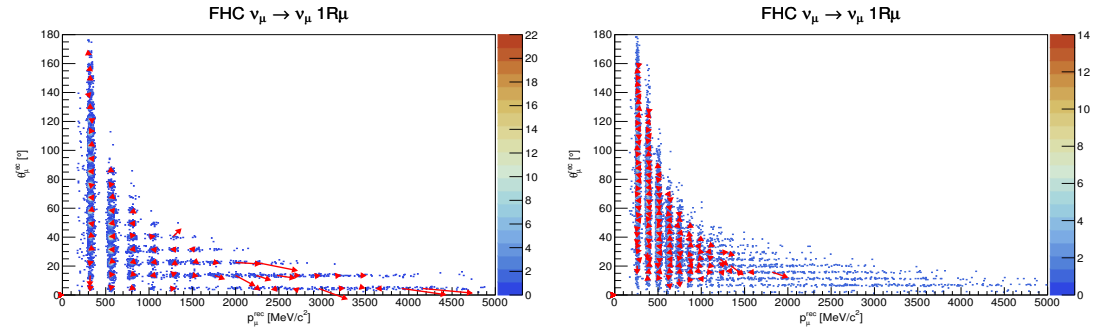

Figure 4.7: Resolution and bias study on p_l and θ_l for FHC 1Rμ. The plots illustrate the scattering of points $(p_l^{rec}, \theta_l^{rec})$ relative to selected intervals based on grid patterns from the θ_l^{true} vs p_l^{true} distribution, with a rescaled red arrow indicating the bias. The grid sizes reported are: (a) 5×5, (b) 10×10, (c) 20×20, and (d) 40×40 grids.

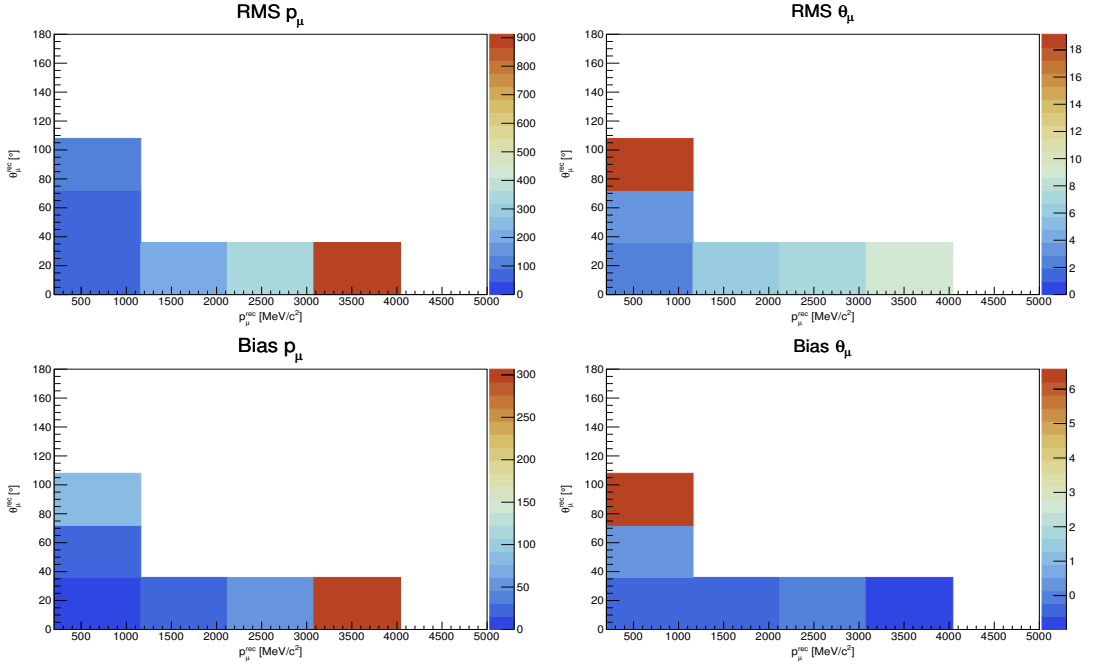

Figure 4.8: The dispersions (RMSs), and the biases for the lepton momenta and angle obtained with the 5×5 grid.

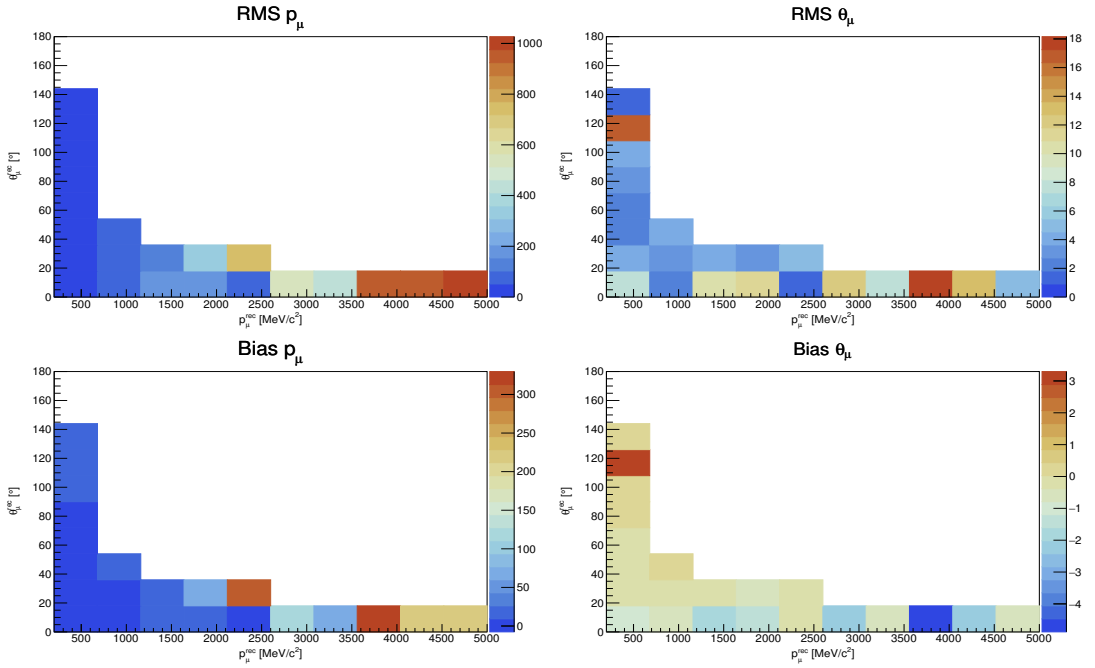

Figure 4.9: The dispersions (RMSs), and the biases for the lepton momenta and angle obtained with the 10×10 grid.

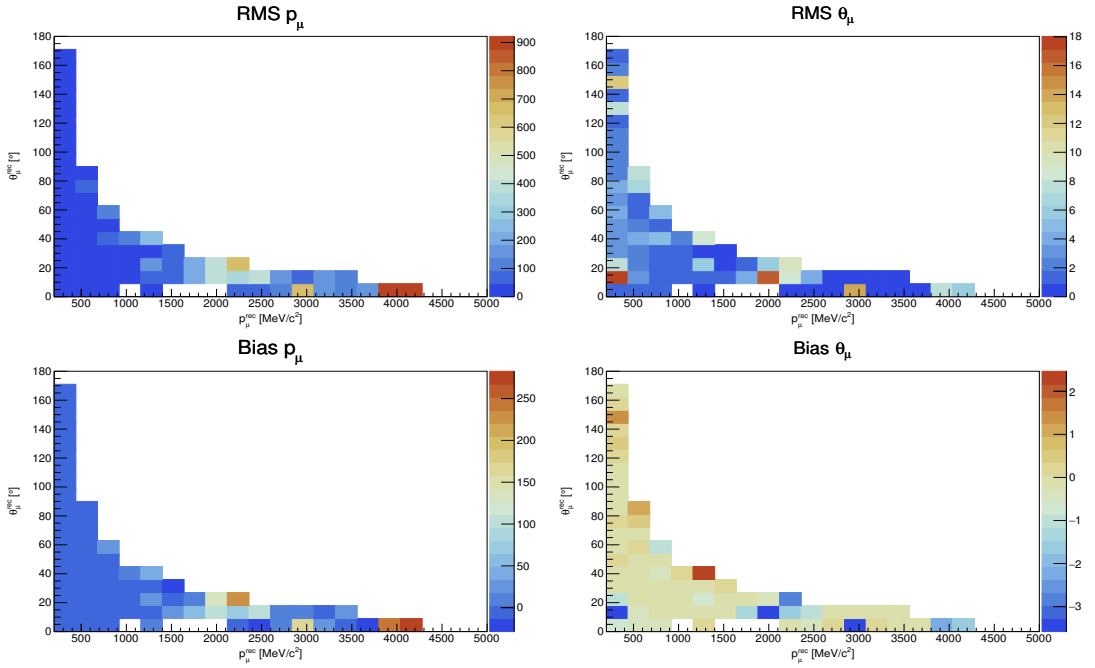

Figure 4.10: The dispersions (RMSs), and the biases for the lepton momenta and angle obtained with the 20×20 grid.

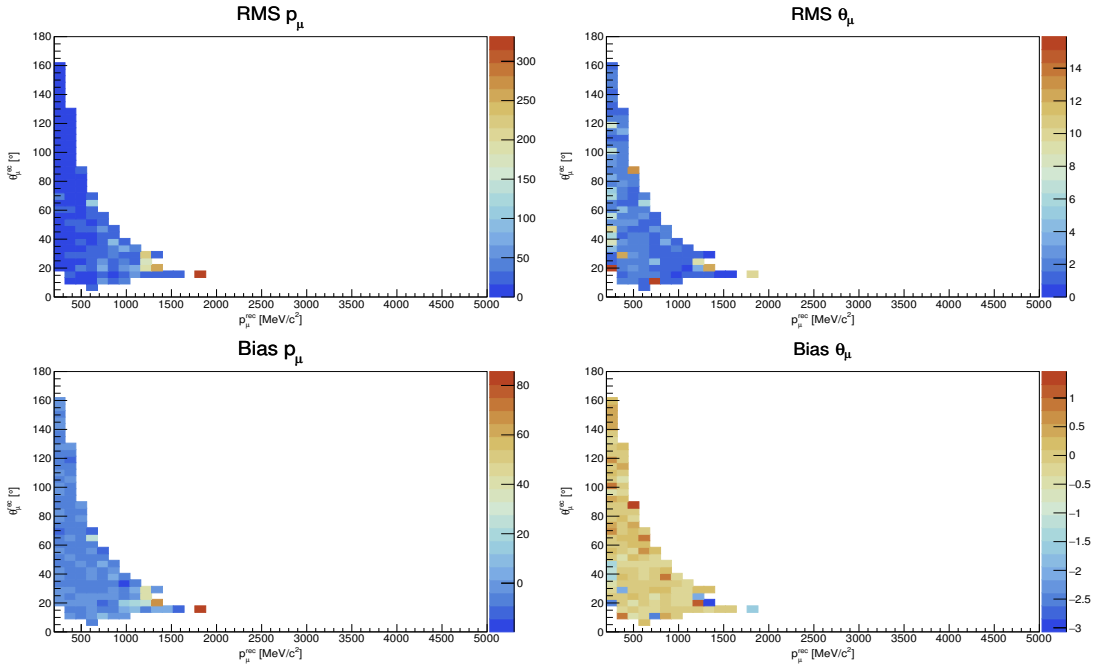

Figure 4.11: The dispersions (RMSs), and the biases for the lepton momenta and angle obtained with the 40×40 grid.

4.4.2 Example for FHC 1Re

Analogously with what was done for 1Rμ samples, below are reported the results for the FHC 1Re samples. The results are provided according to the same grid pattern for a better comparison.

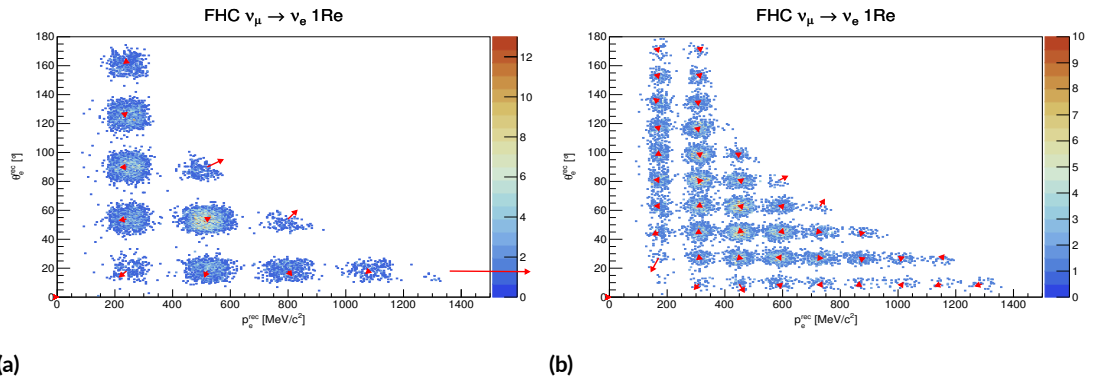

(a) (b)

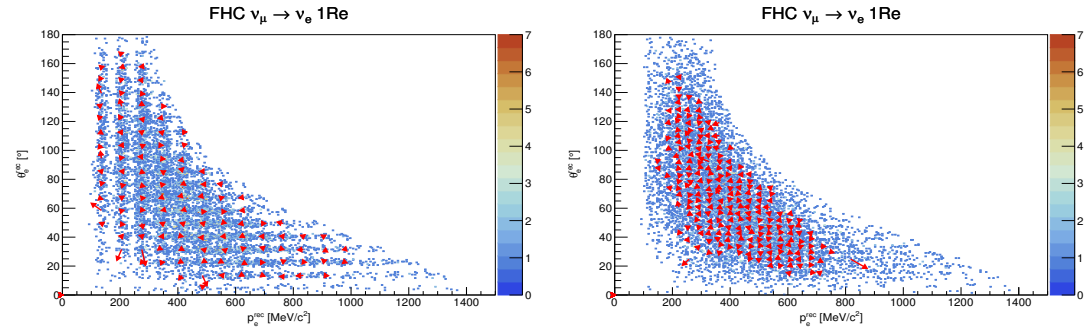

(c) (d)

Figure 4.12: Resolution and bias study on p_l and θ_l for FHC 1Re. The plots illustrate the scattering of points $(p_l^{rec}, \theta_l^{rec})$ relative to selected intervals based on grid patterns from the θ_l^{true} vs p_l^{true} distribution, with a rescaled red arrow indicating the bias. The grid sizes reported are: (a) 5×5, (b) 10×10, (c) 20×20, and (d) 40×40 grids.

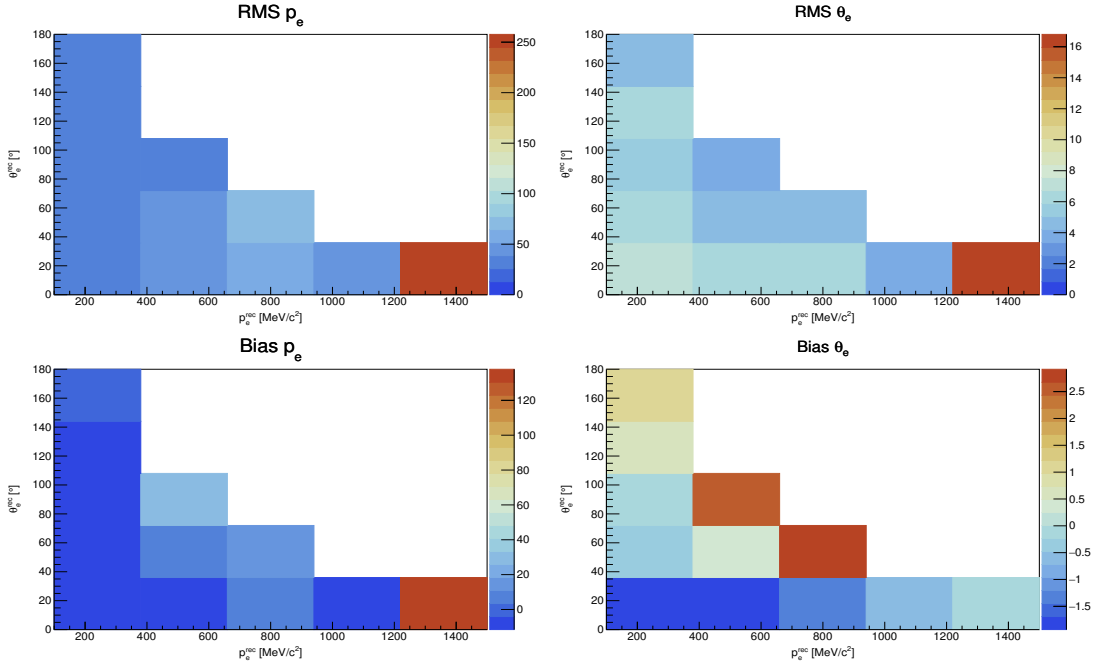

Figure 4.13: The RMS, representing the dispersion, and the bias for the lepton momenta and angle obtained with the 5×5 grid.

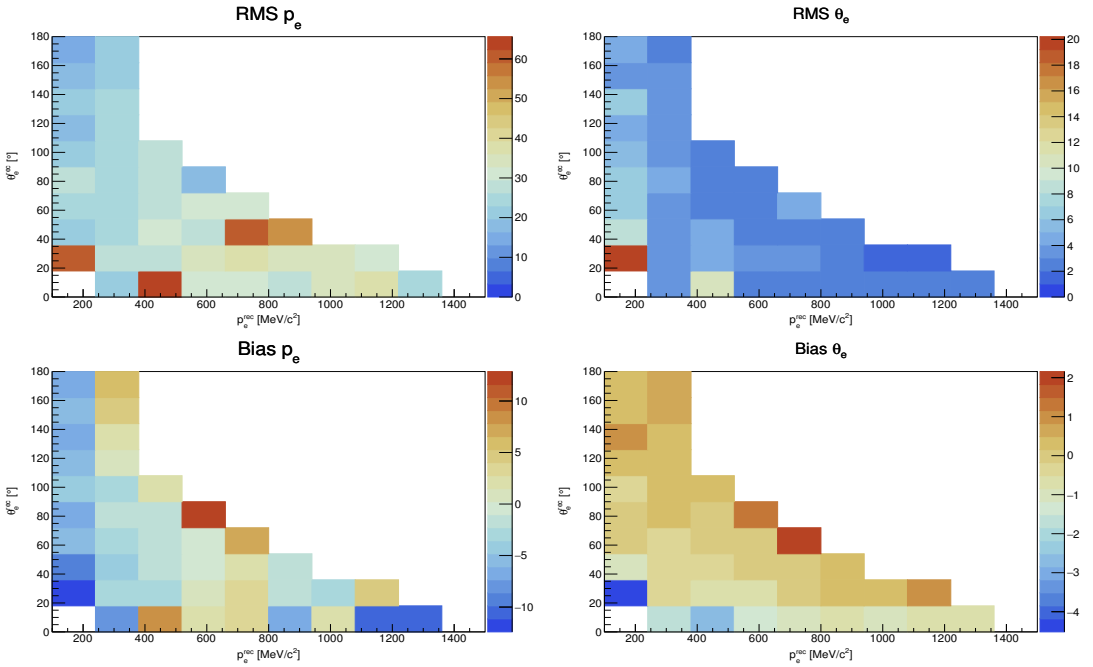

Figure 4.14: The dispersions (RMSs), and the biases for the lepton momenta and angle obtained with the 10×10 grid.

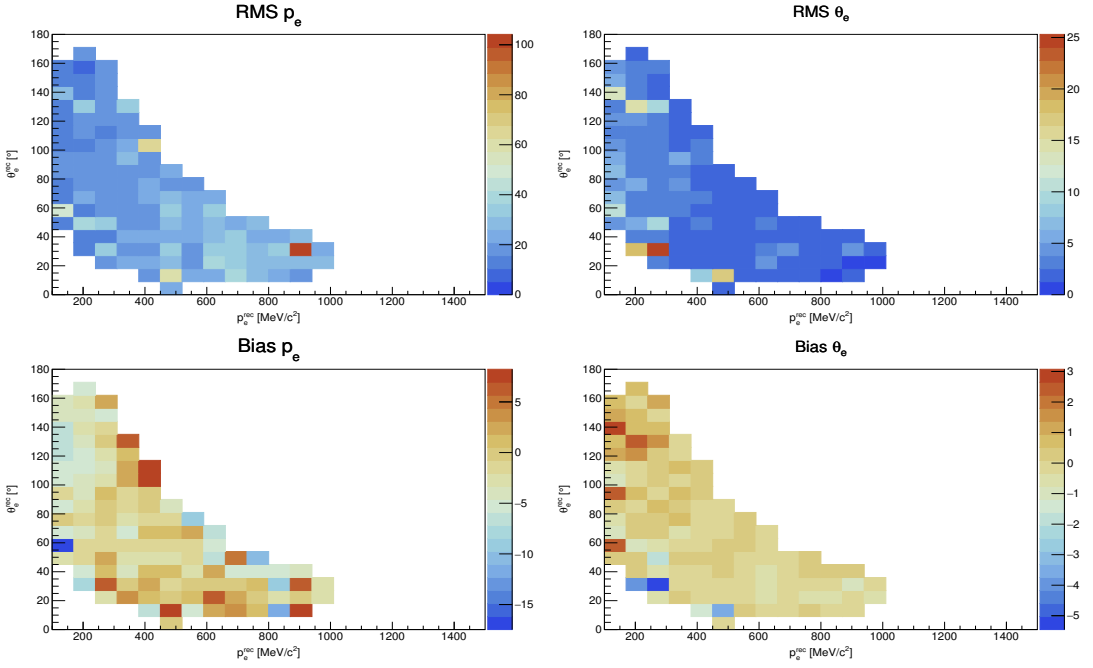

Figure 4.15: The dispersions (RMSs), and the biases for the lepton momenta and angle obtained with the 20×20 grid.

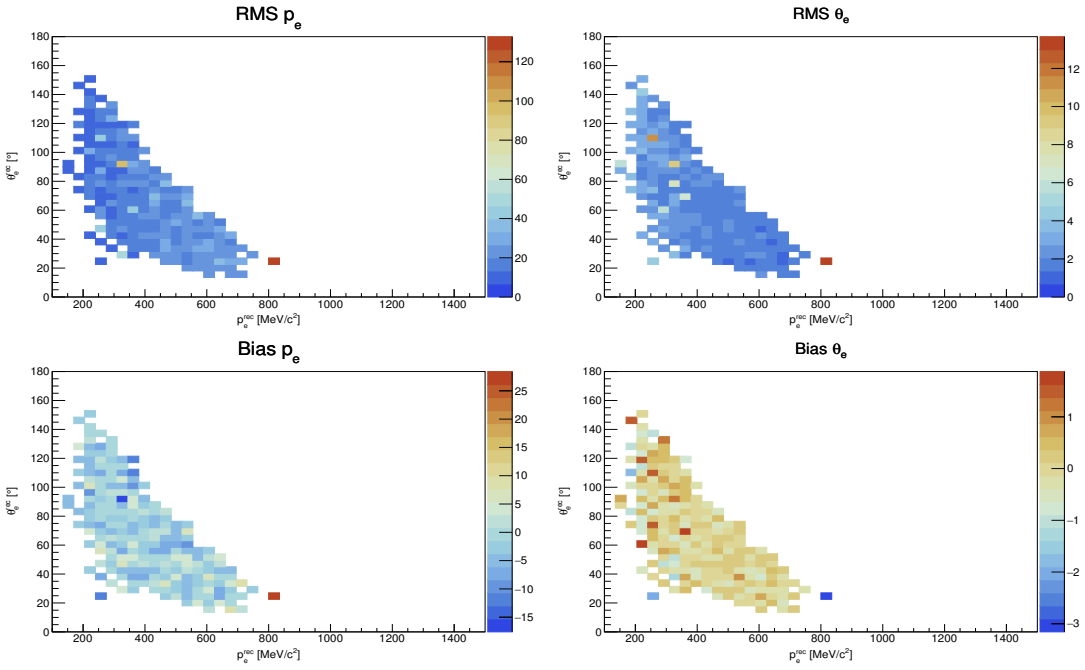

Figure 4.16: The RMS, representing the dispersion, and the bias for the lepton momenta and angle obtained with the 40×40 grid.

The choiche of the rectangle for the true level variables is a trade-off between the requirement of testing a "single point" in the true space and the need of sufficient number of simulated events.

Overall, no problematic regions are observed with the specific trend in the bias. The resolution is also relatively smooth and devoid of anomalous features.

4.5 E_ν^{rec} Resolution

Figures 4.17 and 4.18, show the scatter plot of E_ν^{true} vs E_ν^{rec} for each different sample. It is possible to observe that the majority of the samples align along the diagonal (in red) with a greater concentration near the peak of the beam energy (0.6 GeV), but there are also some evident spreads, extending more or less widely with respect to the different samples. For the CC0π samples (Figure 4.17), these spreads are due to the non-CCQE samples, such as 2p2h (see Section 1.4.3). From those samples the CCQE approximation does not hold. For CC1π^{++} samples (Figure 4.18), the spreads are due to the Δ^{++} resonance approximation, as explained in Section 4.2. These dispersions create tails in the histograms of the reconstructed energy resolution reported below each plot, which is computed as the difference between the true and the reconstructed energy, $\mathrm{E}_\nu^{true} - \mathrm{E}_\nu^{rec}$.

To estimate the resolution, Gaussian fits were applied to the resolution histograms. The fitting range was reduced to obtain a more accurate estimation of the peak, discarding the influence of tails in the distribution. Conversely, to account for the effect of tails, the Root Mean Square (RMS) was also computed.

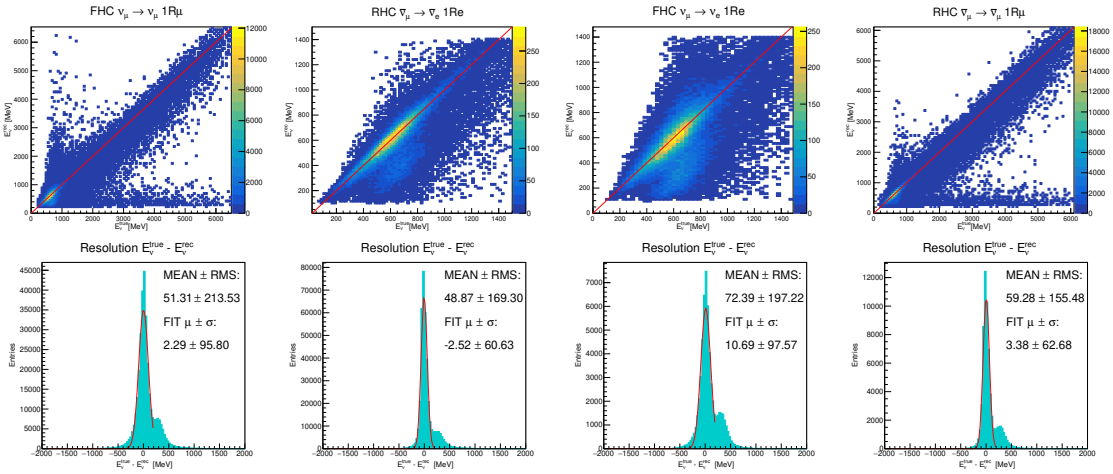

Figure 4.17: E_ν^{true} vs E_ν^{rec} scatter plot and resolution $E_\nu^{true} - \mathrm{E}_\nu^{rec}$ for CC0π samples. From left: FHC 1Rμ, RHC 1Rμ, FHC 1Re, RHC 1Re. For these samples, the CCQE approximation is utilized to compute E_ν^{rec}, therefore the tails on the right of the resolution histograms is due to the non-CCQE samples.

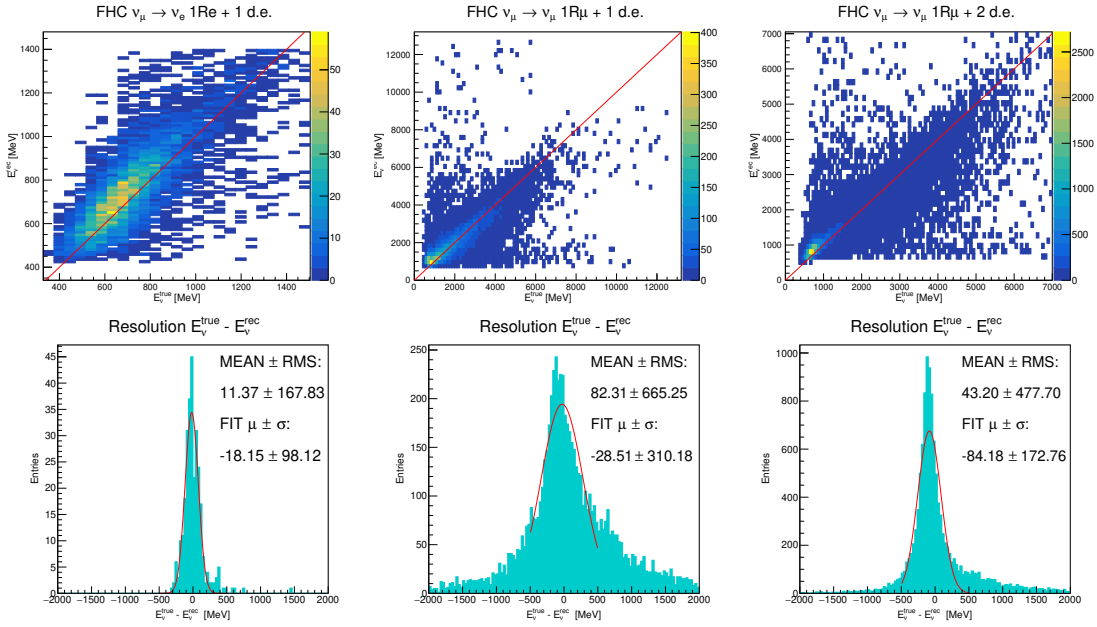

Figure 4.18: E_ν^{true} vs E_ν^{rec} scatter plot and resolution $E_\nu^{true} - E_\nu^{rec}$ for CC1π^{++} samples. From left: FHC 1Re + 1 de, FHC Multi-Rμ + 1 de, FHC Multi-Rμ + 2 de . For these samples the Δ^{++} approximation was performed to compute E_ν^{rec}.

The two estimations for the overall resolution for each sample category are reported in Table 4.6.

Table 4.6: Estimated resolution for each sample category, including both the RMS calculations and the Gaussian fit of the peak. The table summarizes the overall energy resolution for E_ν^{rec} based on the differences between the true and reconstructed neutrino energies for each sample category.

Sample	RMS (MeV)	σ (MeV)
FHC 1Rμ	213	96
RHC 1Rμ	169	61
FHC 1Re	197	98
RHC 1Re	155	63
FHC 1Re + 1 de	168	98
FHC Multi-Rμ + 1 de	665	310
FHC Multi-Rμ + 2 de	478	173

For CC0π samples, the overall resolution, expressed as the RMS, ranges from 150 to 200 MeV. This decreases to 60 to 100 MeV when the effect of tails is not taken into account, specifically in the σ estimations obtained from the Gaussian fits. The same considerations apply to the FHC 1Re + 1 de samples. In contrast, a wider spread is observed in the multi-ring muon samples. This is due to the increased complexity and higher energy of these events, which involve the production of more particles and present greater challenges for reconstruction.

4.5.1 E_ν^{rec} Resolution in bins of E_ν^{true}

The reconstructed energy resolution was studied by dividing the true energy E_ν^{true} into a given number of equal bins. This number was chosen according to [9]. Specifically:

- for muon rings events 30 bins were chosen in the range [0, 3000] MeV, each with a width of 100 MeV;
- for electron ring events, 10 bins were selected in the range [0, 1250] MeV, with each bin having a width of 125 MeV.

For each E_ν^{true} bin, the resolution was computed as the difference between E_ν^{true} and E_ν^{rec} as done before. For the Gaussian fit, the range was reduced to obtain a better estimation of the peak, while the RMS was computed to include the effect of tails.

Two examples are reported below in Figures 4.19 for the FHC 1Rμ samples and 4.20 for the FHC 1Re samples.

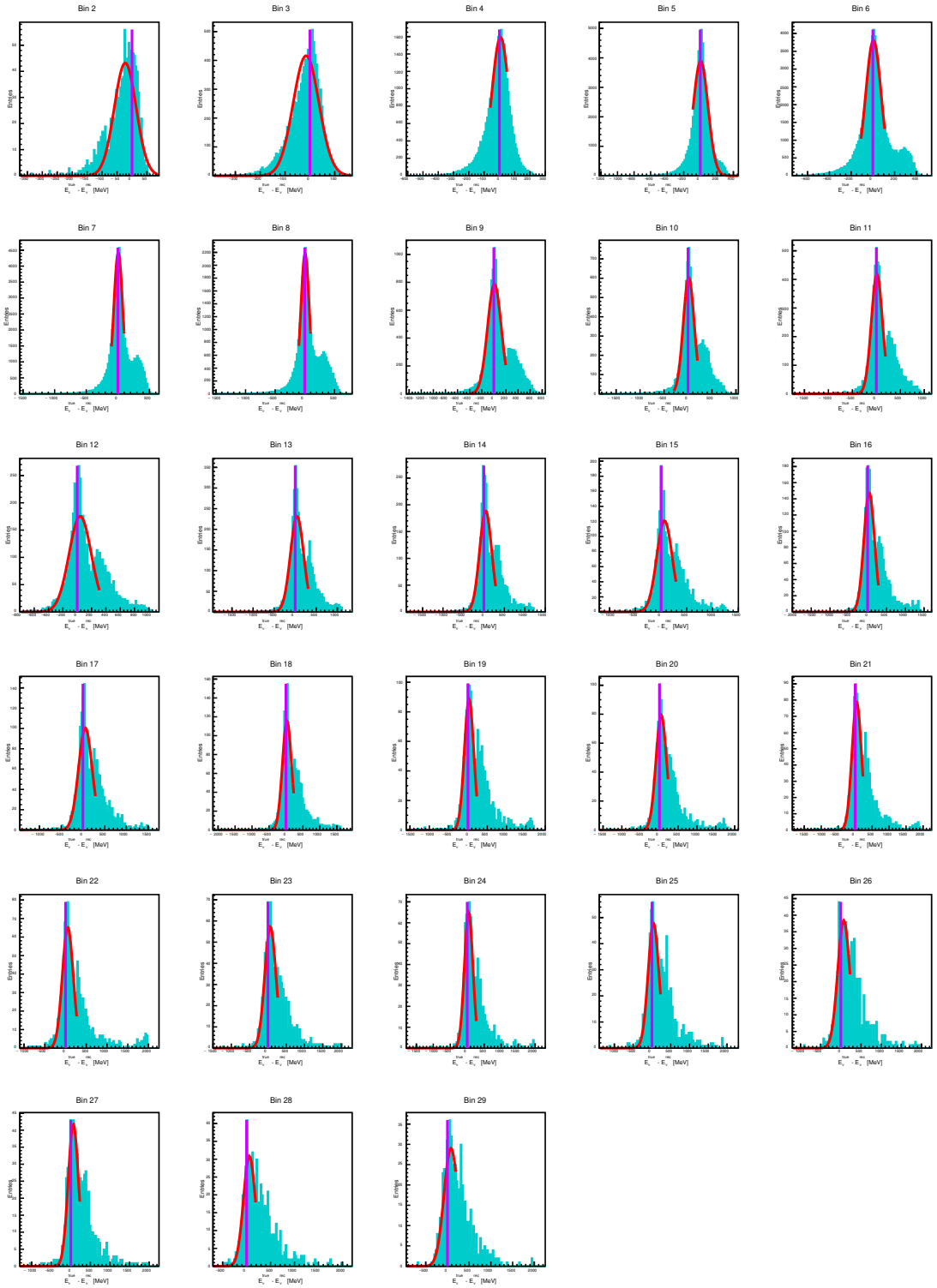

Figure 4.19: Resolution histograms obtained dividing the range [0, 3000] MeV of E_ν^{true} into 30 bins for the FHC 1Rμ samples. The Gaussian fits were performed to estimate the peak of the distribution. In each histogram, the vertical line indicates the zero.

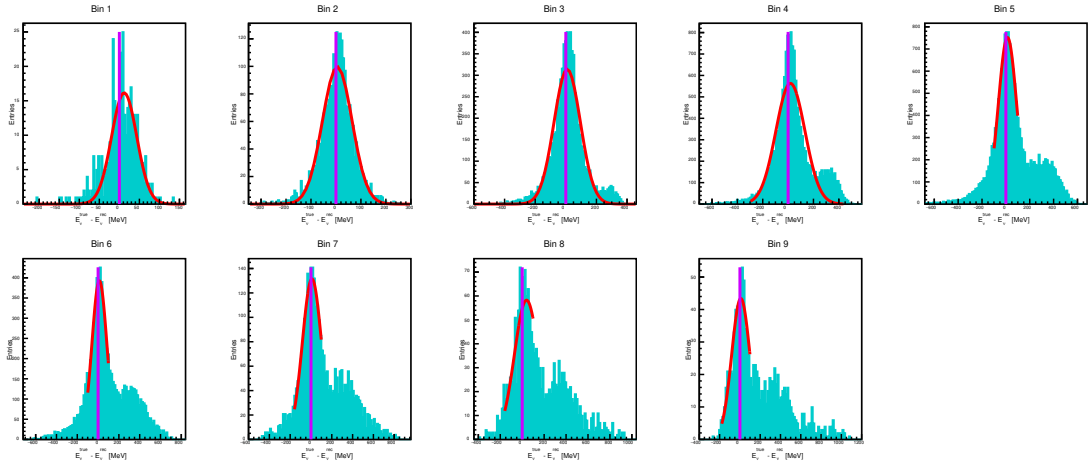

Figure 4.20: Resolution histograms obtained dividing the range [0, 1250] MeV of E_ν^{true} into 10 bins for the FHC 1Re samples. The Gaussian fits were performed to estimate the peak of the distribution. In each histogram, the vertical line indicates the zero.

For each sample taken into account in this analysis, the values of E_ν^{true} are plotted versus the parameters μ and σ obtained from Gaussian fits, along with the mean and RMS of each resolution histogram. The resulting plots are shown below in Figures 4.21 where the σ and RMS values are compared with the corresponding bin width, which was chosen in the T2K analysis. In these plots the error band represents the σ (in blue) or the RMS (in red) while the bullets are placed at the μ of the Gaussian or at the RMS of the distriibution. For an easier comparison, the binwidth used in the T2K analysis is overlayed as an horizontal band.

On the left, only the primary beam contribution is considered, while on the right, the background contributions are included.

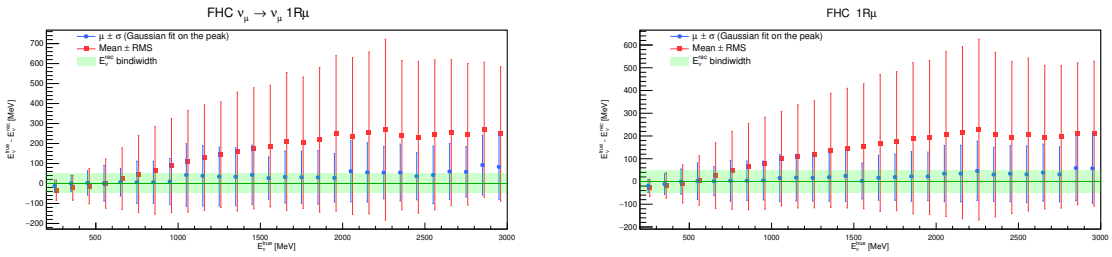

(a) **(b)**

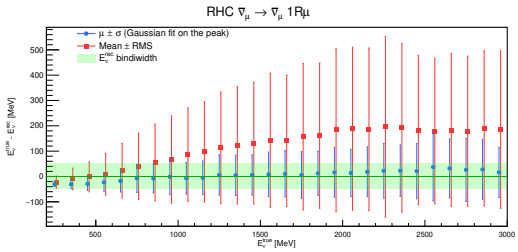
RHC $\bar{\nu}_\mu \rightarrow \bar{\nu}_\mu$ 1Rμ
$\mu \pm \sigma$ (Gaussian fit on the peak)
Mean ± RMS
E_ν^{bin} bindiwidth
$E_\nu^{true} - E_\nu^{rec}$ [MeV]
E_ν^{true} [MeV]

(c)

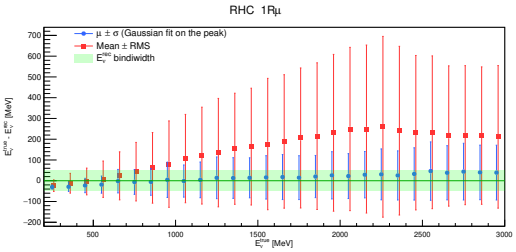
RHC 1Rμ
$\mu \pm \sigma$ (Gaussian fit on the peak)
Mean ± RMS
E_ν^{bin} bindiwidth
$E_\nu^{true} - E_\nu^{rec}$ [MeV]
E_ν^{true} [MeV]

(d)

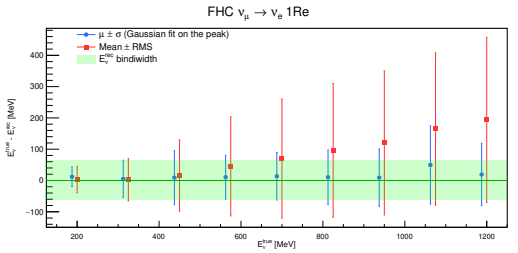
FHC $\nu_\mu \rightarrow \nu_e$ 1Re
$\mu \pm \sigma$ (Gaussian fit on the peak)
Mean ± RMS
E_ν^{bin} bindiwidth
$E_\nu^{true} - E_\nu^{rec}$ [MeV]
E_ν^{true} [MeV]

(e)

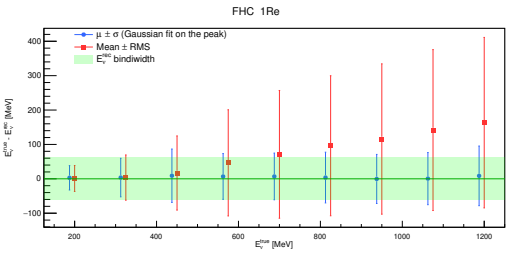
FHC 1Re
$\mu \pm \sigma$ (Gaussian fit on the peak)
Mean ± RMS
E_ν^{bin} bindiwidth
$E_\nu^{true} - E_\nu^{rec}$ [MeV]
E_ν^{true} [MeV]

(f)

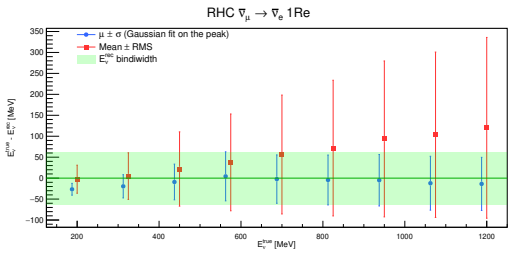
RHC $\bar{\nu}_\mu \rightarrow \bar{\nu}_e$ 1Re
$\mu \pm \sigma$ (Gaussian fit on the peak)
Mean ± RMS
E_ν^{bin} bindiwidth
$E_\nu^{true} - E_\nu^{rec}$ [MeV]
E_ν^{true} [MeV]

(g)

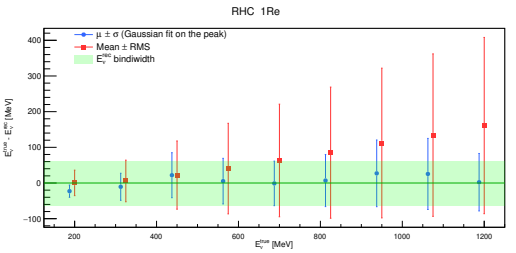
RHC 1Re
$\mu \pm \sigma$ (Gaussian fit on the peak)
Mean ± RMS
E_ν^{bin} bindiwidth
$E_\nu^{true} - E_\nu^{rec}$ [MeV]
E_ν^{true} [MeV]

(h)

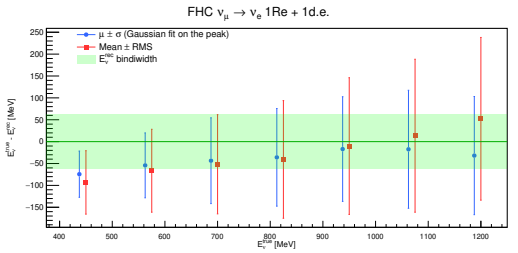
FHC $\nu_\mu \rightarrow \nu_e$ 1Re + 1d.e.
$\mu \pm \sigma$ (Gaussian fit on the peak)
Mean ± RMS
E_ν^{bin} bindiwidth
$E_\nu^{true} - E_\nu^{rec}$ [MeV]
E_ν^{true} [MeV]

(i)

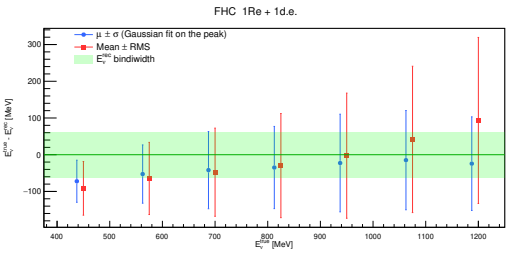
FHC 1Re + 1d.e.
$\mu \pm \sigma$ (Gaussian fit on the peak)
Mean ± RMS
E_ν^{bin} bindiwidth
$E_\nu^{true} - E_\nu^{rec}$ [MeV]
E_ν^{true} [MeV]

(j)

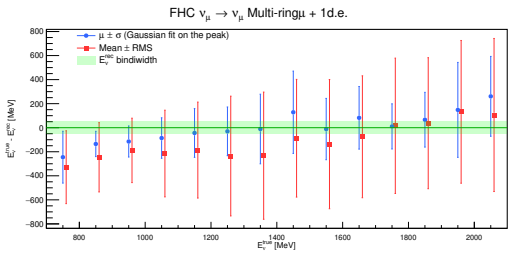
FHC $\nu_\mu \rightarrow \nu_\mu$ Multi-ringμ + 1d.e.
$\mu \pm \sigma$ (Gaussian fit on the peak)
Mean ± RMS
E_ν^{bin} bindiwidth
$E_\nu^{true} - E_\nu^{rec}$ [MeV]
E_ν^{true} [MeV]

(k)

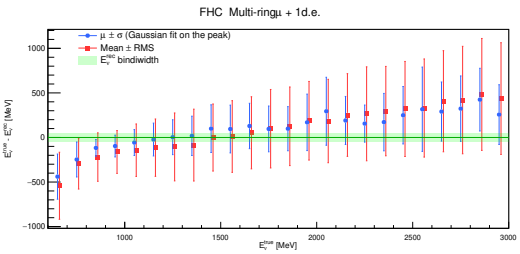
FHC Multi-ringμ + 1d.e.
$\mu \pm \sigma$ (Gaussian fit on the peak)
Mean ± RMS
E_ν^{bin} bindiwidth
$E_\nu^{true} - E_\nu^{rec}$ [MeV]
E_ν^{true} [MeV]

(l)

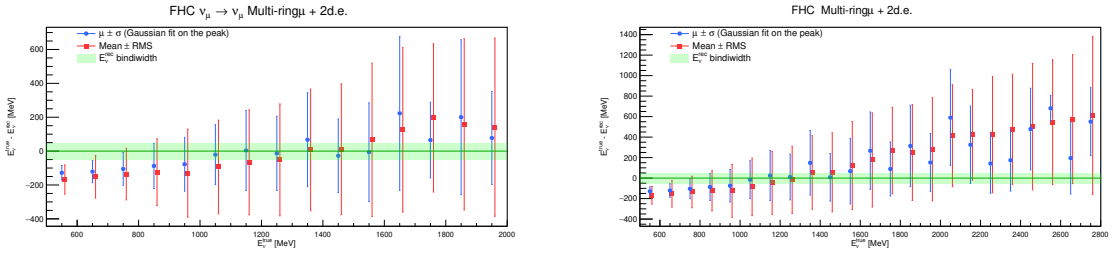

(m) **(n)**

Figure 4.21: E_ν^{rec} resolution plots for FHC and RHC 1Rμ, FHC and RHC 1Re, FHC 1Re + 1 de, FHC Multi-Rμ +1 de, FHC Multi-Rμ + 2 de. On the left the signal only, on the right, the background contributions are included.

As expected, the values of the σ are smaller than the corresponding RMS values, and analogously the values of μ are smaller than the corresponding mean values. This is because the former provide an estimation of the peak while discarding the tail, which is included in the latter and thus makes their value higher.

For all the samples, the resolution (in particular the RMS estimation) increases with the energy,

For both FHC and RHC 1Rμ samples (Figure 4.21 (a, b, c, d)), the resolution spread is around several hundred MeV, while the bin width used in the analysis is 100 MeV.

For FHC and RHC 1Re, and FHC 1Re + 1 de samples (Figure 4.21 (e, f, g, h, i, j)), there is a smaller resolution width and a bigger bin width, making the two more comparable.

For FHC multi ring μ samples (Figure 4.21 (k, l, m, n)) the σ is far more spread than the 100 MeV bin width, ranging from 400 MeV to 1000 MeV.

Finally, comparing the left plots with their corresponding ones on the right (with background contribution included), it can be observed that when background contributions are included, the resolution spread is slightly higher. In Table 4.4 the background contributions are listed with their percentage contribution, providing an overall contribution which ranges from 20 % for FHC Multi-Rμ + 2 de samples to around 50 % for FHC 1Re + 1 de.

4.6 Lepton angle resolution

Since the p-θ fitter uses 2D distributions in p_l-θ_l or E_ν^{rec}-θ_l, the resolution of the recontructed lepton angle θ_l^{rec} was studied analogously to what was done for the recontructed energy done in Section 4.5.

In Subsection 4.1.1 the steps for the true and reconstructed angle computation are reported.

Again, for the sake of an overall comparison, the reconstructed angle distribution are reported in Figure 4.22, which shows that the most probable polar angle is always between 20° and 40° for all the samples. In the plots, the background contributions are included.

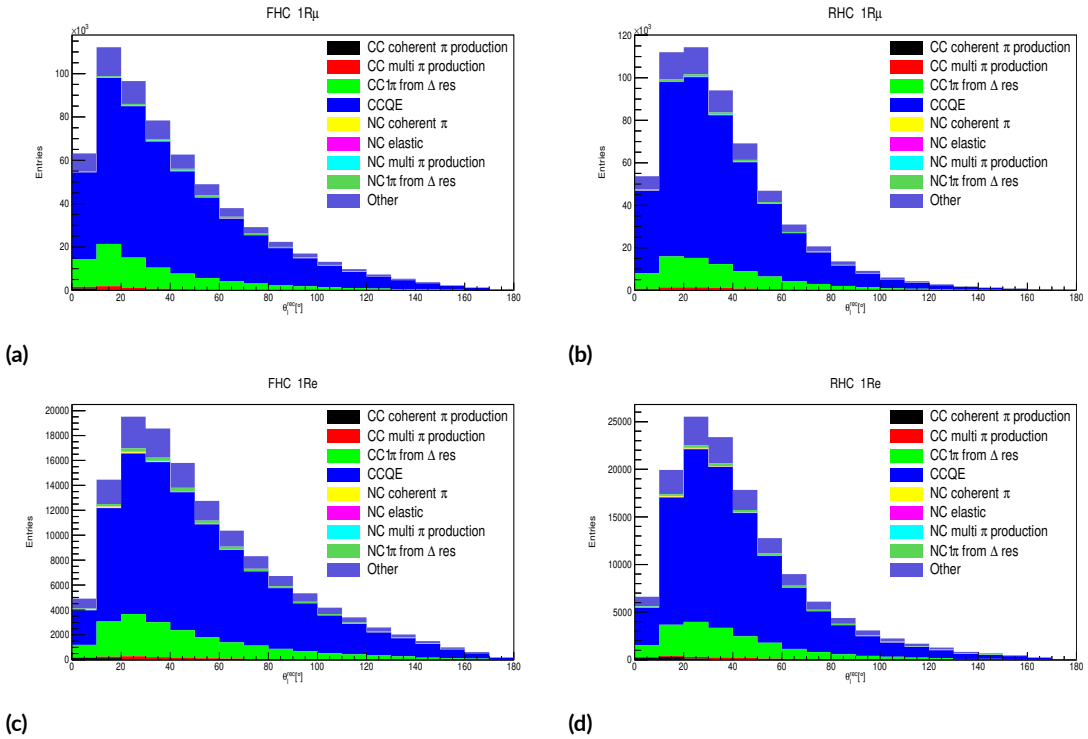

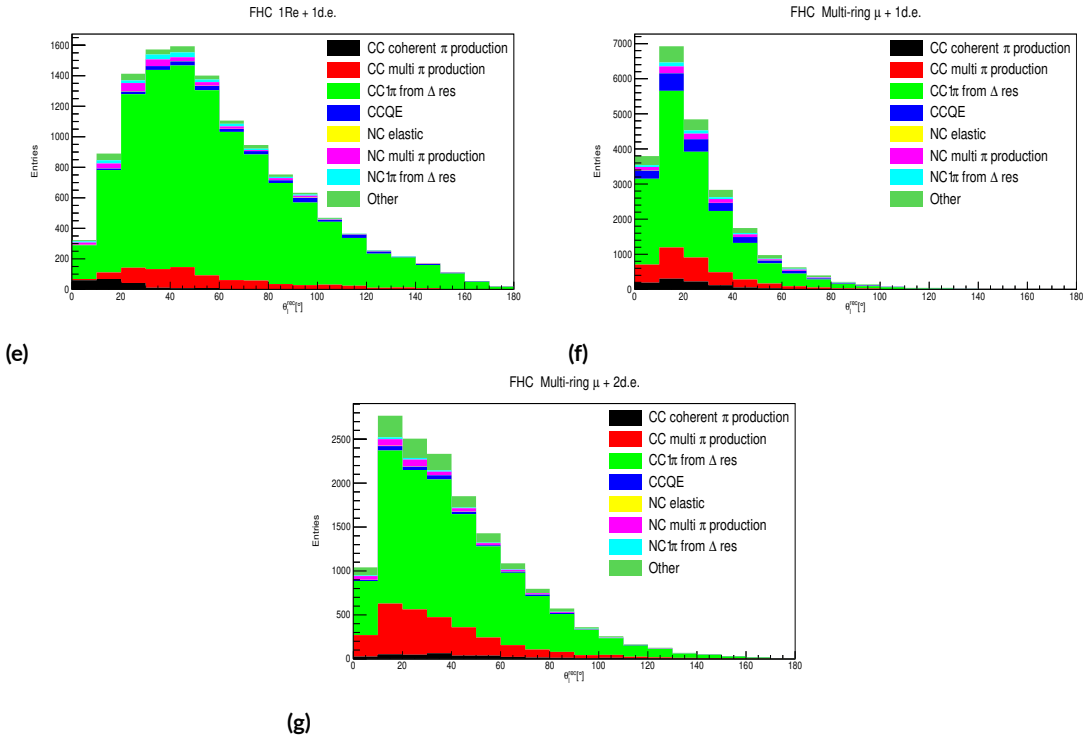

Figure 4.22: Stacked histograms of θ_l^{rec} spectra, where the contribution of different interaction modes has been highlighted. It is evident that for CC-0π samples (a, b, c, d), the main contribution is from the CCQE interaction, while for CC-0π+ samples, the main contribution is from the CC-0π from Δ^{++} interaction.

Figures 4.23 and 4.24, show the scatter plot of θ_l^{true} vs θ_l^{rec} for each different sample. It is possible to observe that the majority of the samples align along the diagonal which is highlighted in red, especially for the electron samples (FHC 1Re, RHC 1Re, FHC 1Re + 1 de), but there are also some evident spreads, extending more widely for the muon ring samples (FHC 1Rμ, RHC 1Rμ, FHC 1Rμ + 1 de , FHC 1Rμ + 2 de). These dispersions are shown below each plot, in the histograms of the reconstructed lepton angle resolution reported below each plot, which is computed as the difference between the true and the reconstructed θ_l, $\theta_l^{true} - \theta_l^{rec}$.

Analogously to what was done in Section 4.5, to estimate the resolution, Gaussian fits were applied to the resolution histograms. The fitting range was reduced to obtain a more accurate estimation of the peak, discarding the influence of the tails. Conversely, to account for them, the Root Mean Square (RMS) was also computed.

The results show perfectly zero-centered peaks indicating the absence of biases — unlike those observed in the energy resolution.

The standard deviations obtained from the Gaussian fits were consistently around 1°-2°.

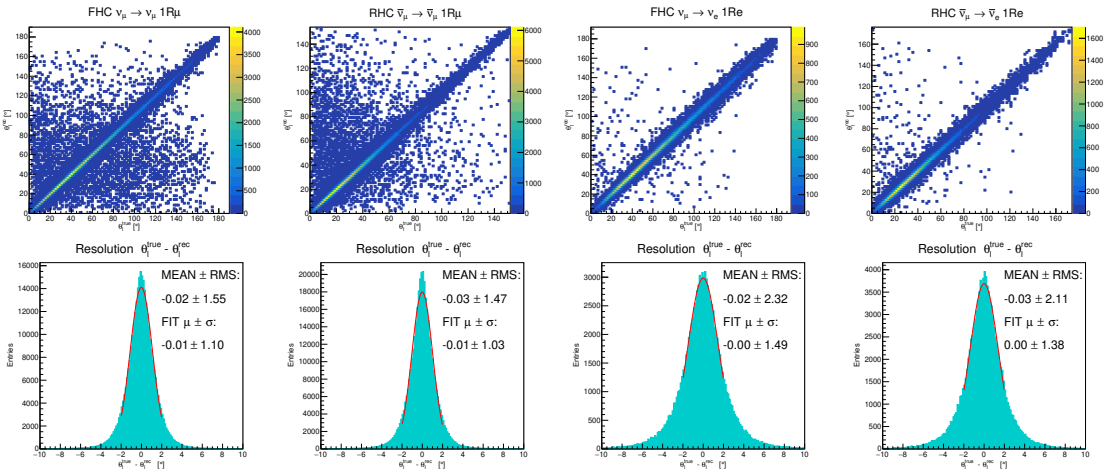

Figure 4.23: θ_l^{true} vs θ_l^{rec} scatter plot and resolution computed as $\theta_l^{true} - \theta_l^{rec}$ for CC0π samples. From left: FHC 1Rμ, RHC 1Rμ, FHC 1Re, RHC 1Re.

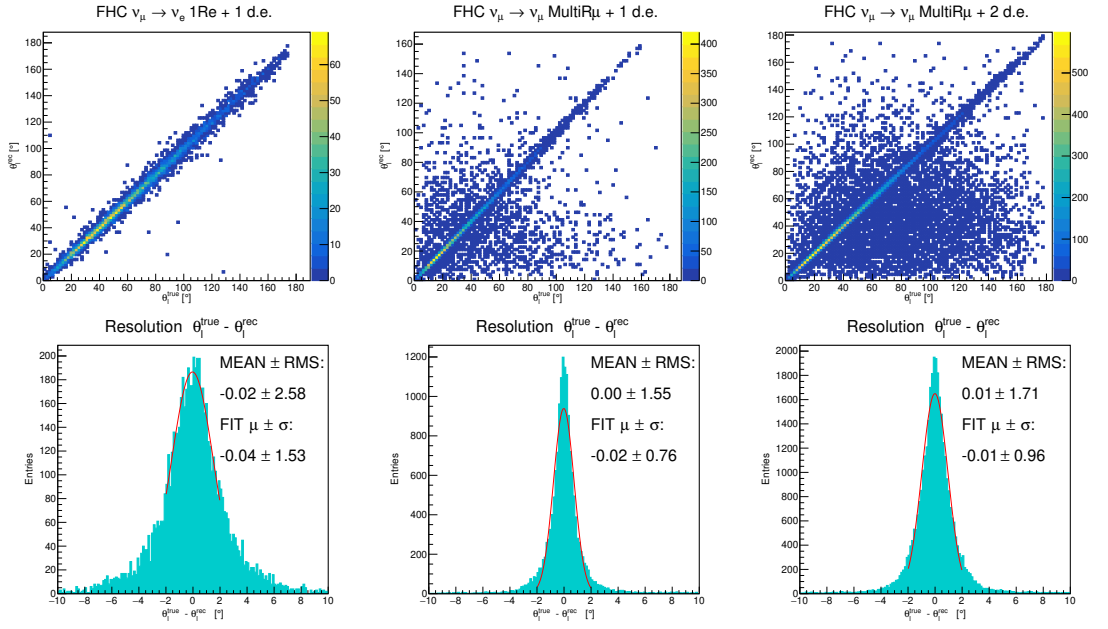

Figure 4.24: θ_l^{true} vs θ_l^{rec} scatter plot and resolution computed as θ_l^{true} - θ_l^{rec} for CC1π + + samples. From left: FHC 1Re + 1 de, FHC 1Rμ + 1 de , FHC 1Rμ + 2 de.

4.6.1 θ_l^{rec} resolution in bins of θ_l^{true}

Analogously to that was done in Subsection 4.5.1, the reconstructed lepton angle resolution was studied by dividing the true lepton angle θ_l^{true} into a given number of equal bins. According to the current binning choice, it was decided to divide the range of [0, 180]° into 18 bins, each with a width of 10°, for all samples.

For each θ_l^{true} bin, the resolution was computed as the difference between θ_l^{true} and θ_l^{rec} as done before. For the Gaussian fit, the range was reduced to obtain a better estimation of the peak, while the RMS was computed to include the effect of having different populations. An example is shown below in Figure 4.25 for the FHC 1Rμ samples.

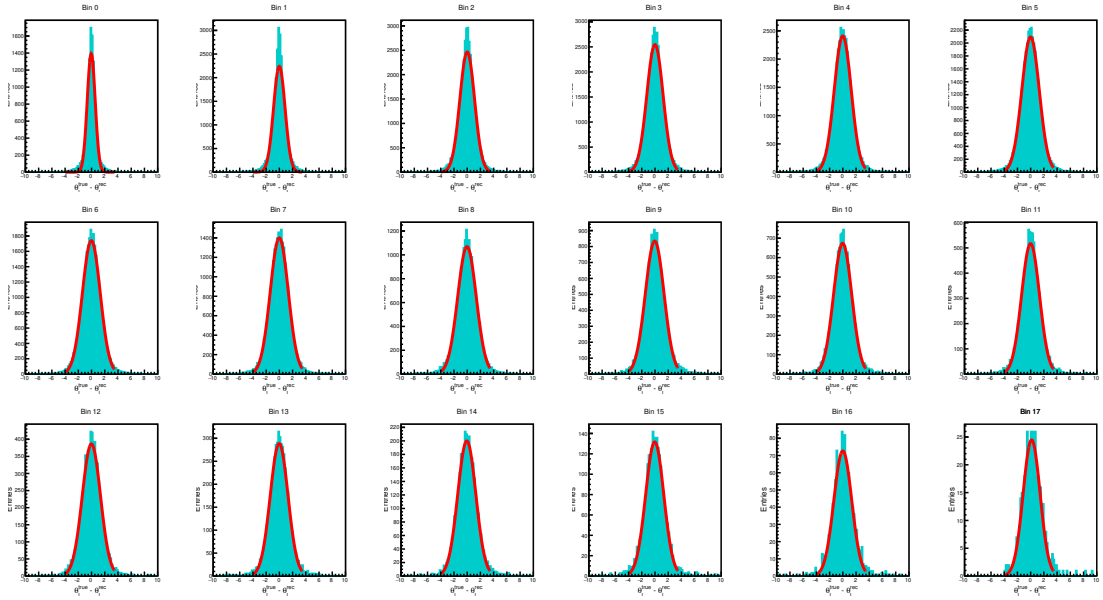

Figure 4.25: Resolution histograms obtained dividing the range [0, 180]° of θ_l^{true} into 18 bins for the FHC 1Rμ samples. The Gaussian fits were performed to estimate the peak of the distribution.

For each sample taken into account in this analysis, the values of θ_l^{true} are plotted againts the parameters μ and σ obtained from the Gaussian fits, along with the mean and RMS of each resolution histogram. The resulting plots are shown below in Figures 4.26. On the left, only the primary beam contribution is considered, while on the right, the background contributions are included.

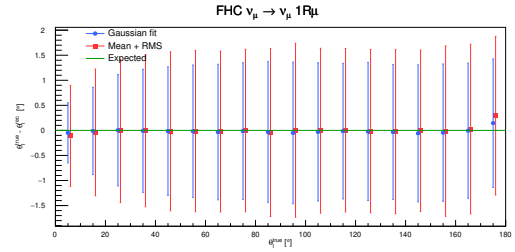
FHC $\nu_\mu \rightarrow \nu_\mu$ 1Rμ
Gaussian fit
Mean + RMS
Expected

(a)

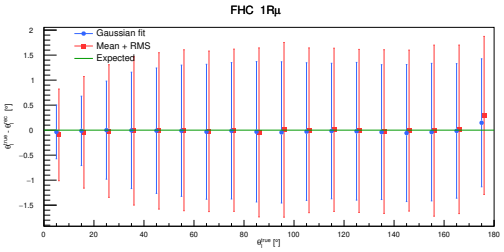
FHC 1Rμ
Gaussian fit
Mean + RMS
Expected

(b)

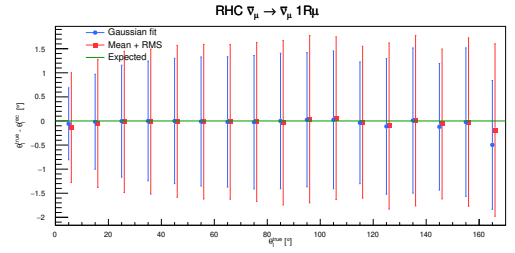
RHC $\bar{\nu}_\mu \rightarrow \bar{\nu}_\mu$ 1Rμ
Gaussian fit
Mean + RMS
Expected

(c)

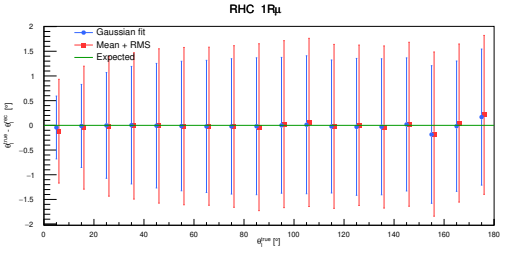
RHC 1Rμ
Gaussian fit
Mean + RMS
Expected

(d)

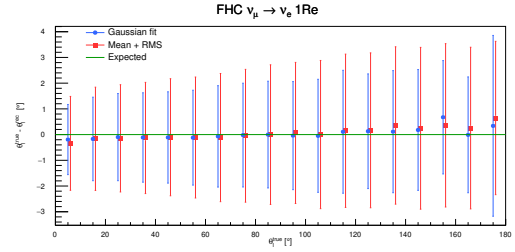
FHC $\nu_\mu \rightarrow \nu_e$ 1Re
Gaussian fit
Mean + RMS
Expected

(e)

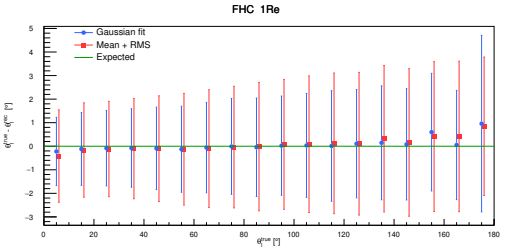
FHC 1Re
Gaussian fit
Mean + RMS
Expected

(f)

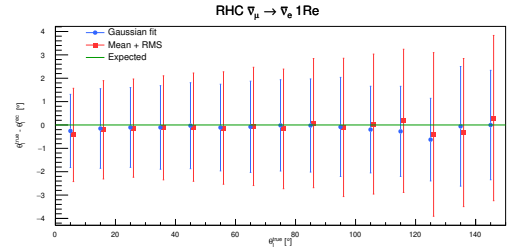
RHC $\bar{\nu}_\mu \rightarrow \bar{\nu}_e$ 1Re
Gaussian fit
Mean + RMS
Expected

(g)

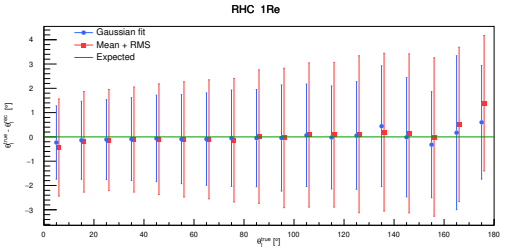
RHC 1Re
Gaussian fit
Mean + RMS
Expected

(h)

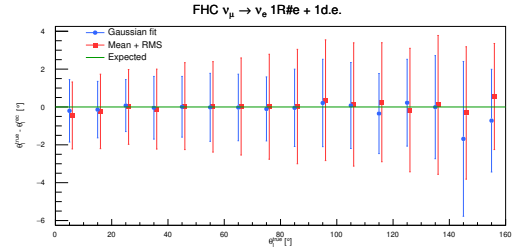
FHC $\nu_\mu \rightarrow \nu_e$ 1R#e + 1d.e.
Gaussian fit
Mean + RMS
Expected

(i)

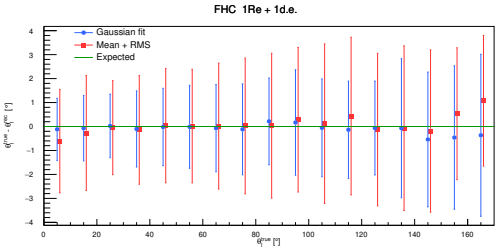
FHC 1Re + 1d.e.
Gaussian fit
Mean + RMS
Expected

(j)

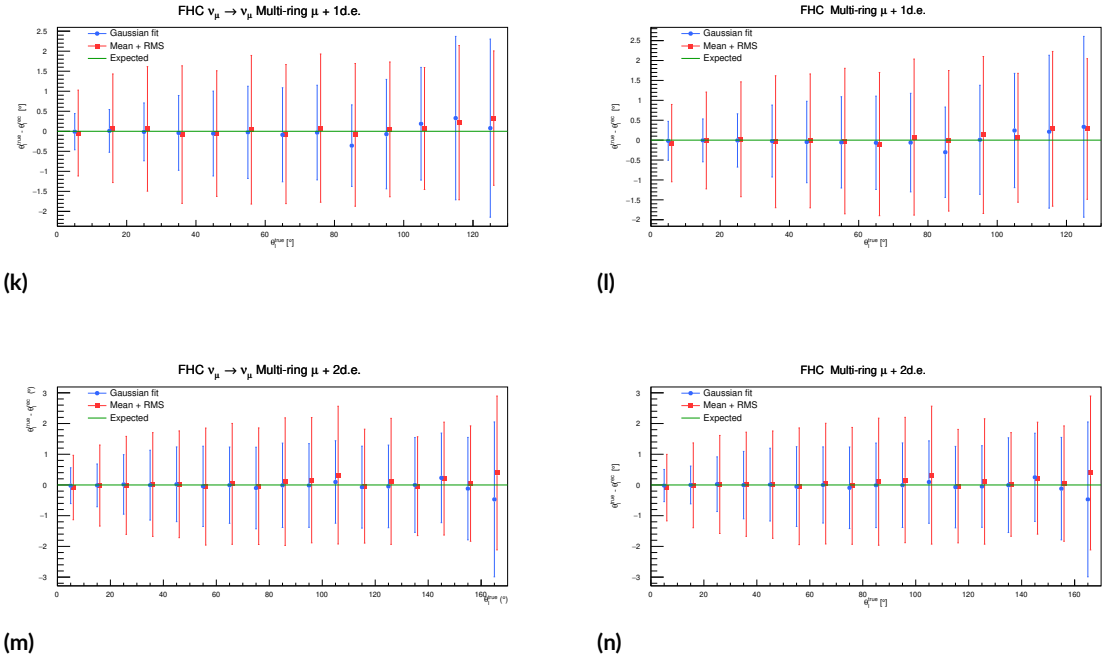

Figure 4.26: $\theta_{\nu}^{\text{rec}}$ resolution plots for FHC and RHC 1Rμ, FHC and RHC 1Re, FHC 1Re + 1 de, FHC Multi-Rμ +1 de, FHC Multi-Rμ + 2 de. On the left the signal only, on the right, the background contributions are included.

The plots above show that the angle resolution ranges between 1° and 3°. The comparison between the Gaussian fit parameters, namely the mean and standard deviation ($\mu \pm \sigma$) and the mean ± RMS, computed using the entire set of histogram entries, shows that the estimate obtained from the fit is only slightly smaller. The non gaussian tails are much less evident in the case of angles with respect to the reconstructed energy where they played a major role.

Finally, comparing the plots on the left, where only the primary beam contribution was considered, with their counterparts on the right, where background contributions were included, reveals that the background contributions slightly increased the spread of the resolution.

Overall, the resolutions are always largely smaller than the bin width adopeted in the analysis, which is 10 °.

4.7 Updating the Binning

Based on the resolution analysis performed for the reconstructed neutrino energy and the lepton angle, it was found that while the angle binning choice adequately

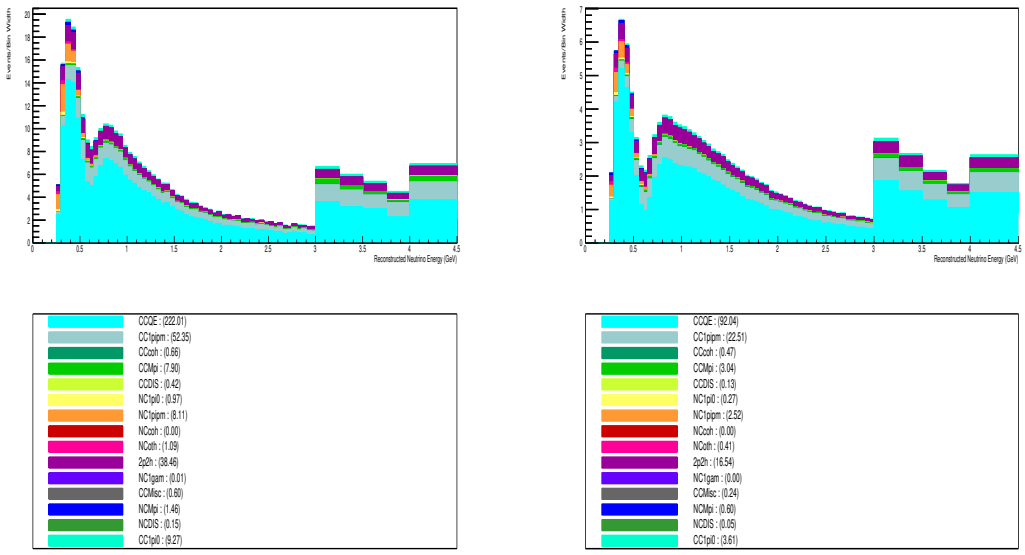

(a) (b)

Figure 4.27: Oscillated event rate spectra in reconstructed energy for FHC 1Rμ (a) and RHC 1Rμ (b) with 50 MeV binwidth.

covers the resolution range, the energy resolution is significantly more spread out compared to the bin width, especially for μ-like samples. A reasonable choice for the binning of the μ-like reconstructed energy spectrum could be to increase the binwidth in the [0, 3000] MeV region.

4.8 Effect of the optimized binning on oscillation parameters

In 4.5, the resolutions of the reconstructed neutrino energy were studied for the binning choice adopted in [9]. It was found that, while the resolution for e-like samples is comparable to the bin width used in [9], the resolution for μ-like samples is significantly larger, even when excluding the effect associated with the non-CCQE samples.

Reconstructed energy spectra at SK with different binning configurations were produced using MaCh3 for 1Rμ samples. The outputs for bin widths of 50 MeV in the range [0, 3000] MeV are presented in Figures 4.27.

The 100 MeV binwidth spectra are shown alongside the spectra presented in [9].

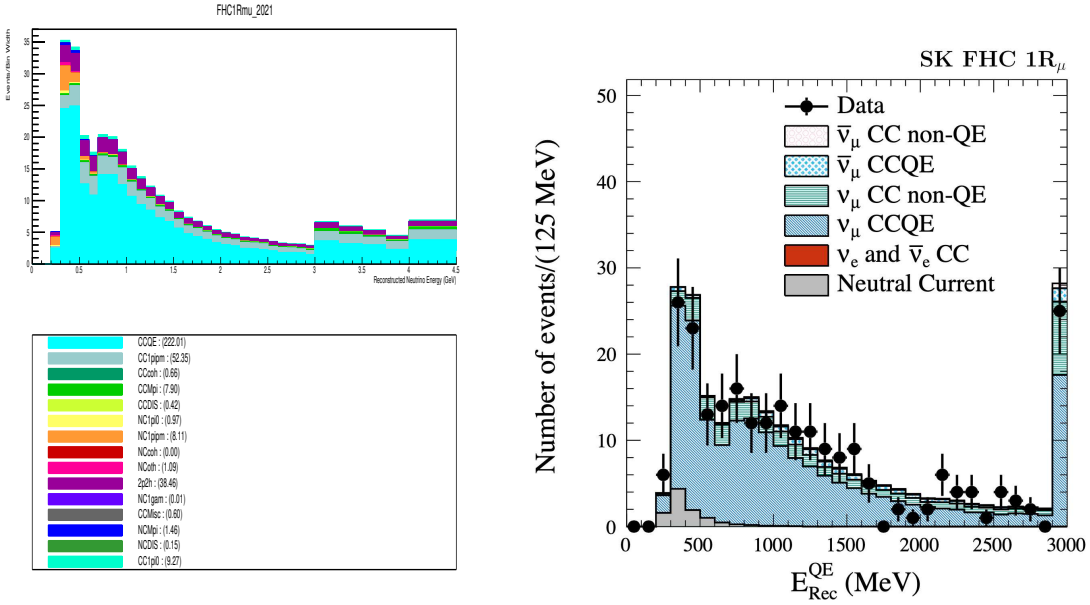

(a) (b)

Figure 4.28: Oscillated event rate spectra in reconstructed energy for FHC 1Rμ with 100 MeV binwidth. In (a) the result obtained with MaCh3, in (b) the result from [9].

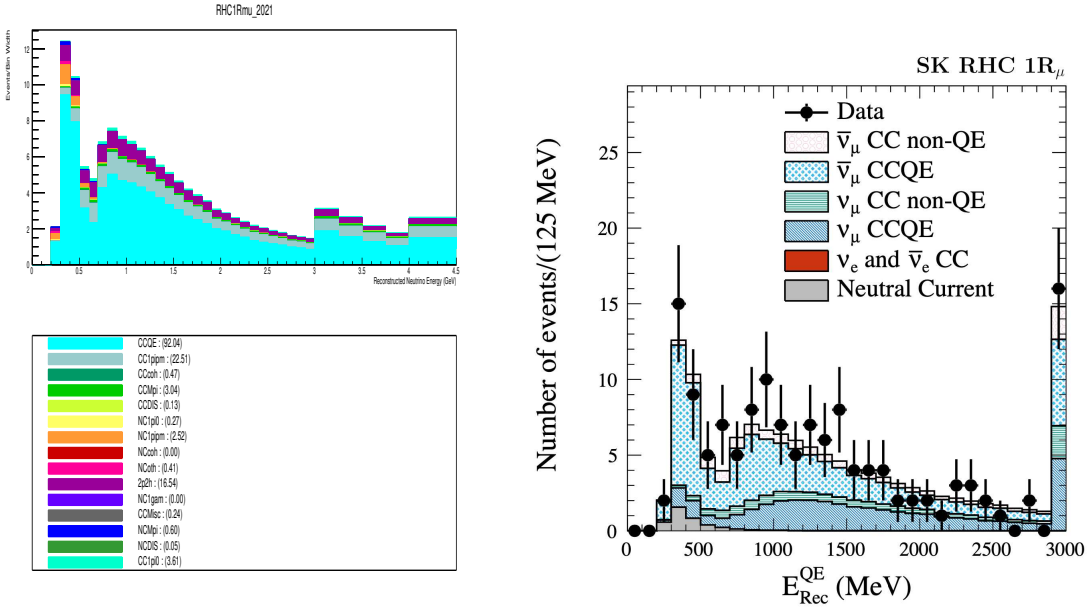

(a) (b)

Figure 4.29: Oscillated event rate spectra in reconstructed energy for RHC 1Rμ with 100 MeV binwidth. In (a) the result obtained with MaCh3, in (b) the result from [9].

Following the present, and similar, studies, the oscillation parameter fit output was studied with respect to changes in the reconstructed energy binning. Figure 4.30 shows the fit of the δ_{CP} parameter performed with three different binwidths [10]. In the plot, binv1 is the 50 MeV binwidth in the [0, 3000] MeV region, while in binv2 the binsize in the region [1500, 3000] MeV was changed from 50 MeV to 100 MeV, finally, in binv3 the binsize in the region [0, 1000] MeV was changed from 100 to 50 MeV with respect to the binv2 configuration.

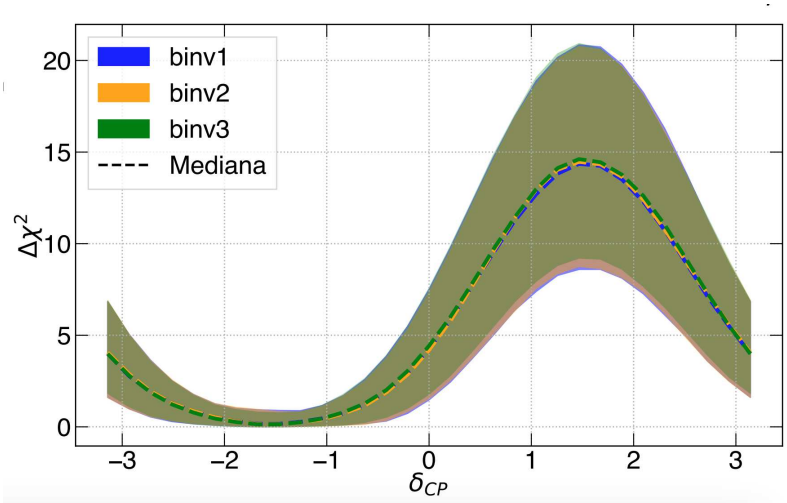

Figure 4.30: Comparison between δ_{CP} fits for different binwidths. Image taken from [10]

As it can be seen the three different binning choices provide very similar results especially compared to the band that represents the spread in the results due to the statistics. This indicates that for this parameter (but the conclusion also hold for the other ones) the optimization of the fitting is playing a subleading effect in the results. Nevertheless is it interesting to characterize the performance of the reconstruction in all the phase space as we have done, especially in view of larger statistical samples, for which these systematical effects could become more relevant.

5
Conclusions

A comprehensive study of the reconstructed neutrino energy resolution E_ν^{rec} (p_l^{rec}, θ_l^{rec}) was conducted with the aim of providing a guide in the choice of an optimized binning scheme for E_ν^{rec} and θ_l^{rec}.

First, it was observed how E_ν^{rec} varies across the (p_μ, θ_μ) plane, by superimposing the iso-E_ν^{rec} curves onto the (p_l^{rec}, θ_l^{rec}) distribution. In this way it is possible to visualize the relationship between lepton kinematics and reconstructed neutrino energy.

The distribution of p_l^{rec} and θ_l^{rec} was further examined by visualizing the samples for different intervals of true neutrino energy (E_ν^{true}). It was checked that the samples are aligned along the iso-E curves. In this way it is possible to gain insight into how the reconstructed kinematic variables behave across different energy bins. We have shown that the expected behaviour is respected by the results and explained the reason of deviations from the ideal case in which points should lie exactly on the iso-E lines (spread in the true values and the simulation of Fermi momentum of nucleons). This was a new plot that was not used before in other analyses.

The resolution of the (p_l, θ_l) was further examined by visualizing how the reconstructed points (p_l^{rec}, θ_l^{rec}) scatter relative to intervals centered on a grid of true values (p_l^{true}, θ_l^{true}). It was checked that no anomalies or evident biases affect the (p_l^{rec}, θ_l^{rec}) with respect to the true values.

Then, the study was extended to the resolution of reconstructed neutrino energy

(E_ν^{rec}) and reconstructed lepton angle (θ_l^{rec}). In particular the true neutrino energy and lepton angle have been divided into several equal bins in order to study the resolution of the reconstructed variable in the bins. To estimate the resolution, both the *sigma* of the Gaussian contribution (which excludes the effect of tails) and the root mean square (RMS) of the full distribution were calculated. The results show that the effect of tails, particularly visible in the reconstructed energy of the CC0π samples, significantly impacts the energy resolution, resulting in values that are larger than the bin width.

These findings provide valuable insights into the resolution of the reconstructed variables and offer a foundation for further refinement. In particular, necessary information to reconsider the current binning strategy have been provided in this study. They will turn useful especially with the increase in statistics that will become available in the next years.

A

Appendix

A.1 Minituples Run11 recap

The Minituples Run11 are

- FHC 1Rμ, `iclass` = 13 :
  - `t2ksk19b.fqv4r0b.21bv2_run11.fhc.numu_x_numu_numuselec.root`
  - `t2ksk19b.fqv4r0b.21bv2_run11.fhc.numu_x_nue_numuselec.root`
  - `t2ksk19b.fqv4r0b.21bv2_run11.fhc.nue_x_nue_numuselec.root`
  - `t2ksk19b.fqv4r0b.21bv2_run11.fhc.numubar_x_numubar_numuselec.root`
  - `t2ksk19b.fqv4r0b.21bv2_run11.fhc.numubar_x_nuebar_numuselec.root`
  - `t2ksk19b.fqv4r0b.21bv2_run11.fhc.nuebar_x_nuebar_numuselec.root`

- RHC 1Rμ, `iclass` = 13:
  - `t2ksk19b.fqv4r0b.21bv2_run11.fhc.numu_x_numu_numuselec.root`
  - `t2ksk19b.fqv4r0b.21bv2_run11.fhc.numu_x_nue_numuselec.root`
  - `t2ksk19b.fqv4r0b.21bv2_run11.fhc.nue_x_nue_numuselec.root`
  - `t2ksk19b.fqv4r0b.21bv2_run11.fhc.numubar_x_numubar_numuselec.root`
  - `t2ksk19b.fqv4r0b.21bv2_run11.fhc.numubar_x_nuebar_numuselec.root`
  - `t2ksk19b.fqv4r0b.21bv2_run11.fhc.nuebar_x_nuebar_numuselec.root`

- FHC 1Re, `iclass` = 11:
  - `t2ksk19b.fqv4r0b.21bv2_run11.fhc.numu_x_numu_nueselec.root`
  - `t2ksk19b.fqv4r0b.21bv2_run11.fhc.numu_x_nue_nueselec.root`
  - `t2ksk19b.fqv4r0b.21bv2_run11.fhc.nue_x_nue_nueselec.root`
  - `t2ksk19b.fqv4r0b.21bv2_run11.fhc.numubar_x_numubar_nueselec.root`
  - `t2ksk19b.fqv4r0b.21bv2_run11.fhc.numubar_x_nuebar_nueselec.root`
  - `t2ksk19b.fqv4r0b.21bv2_run11.fhc.nuebar_x_nuebar_nueselec.root`

- RHC 1Re, `iclass` = 11:
  - `t2ksk19b.fqv4r0b.21bv2_run11.fhc.numu_x_numu_nueselec.root`
  - `t2ksk19b.fqv4r0b.21bv2_run11.fhc.numu_x_nue_nueselec.root`
  - `t2ksk19b.fqv4r0b.21bv2_run11.fhc.nue_x_nue_nueselec.root`
  - `t2ksk19b.fqv4r0b.21bv2_run11.fhc.numubar_x_numubar_nueselec.root`
  - `t2ksk19b.fqv4r0b.21bv2_run11.fhc.numubar_x_nuebar_nueselec.root`
  - `t2ksk19b.fqv4r0b.21bv2_run11.fhc.nuebar_x_nuebar_nueselec.root`

- FHC 1Re + 1 de, `iclass` = 14:
  - `t2ksk19b.fqv4r0b.21bv2_run11.fhc.numu_x_numu_cc1piselec.root`
  - `t2ksk19b.fqv4r0b.21bv2_run11.fhc.numu_x_nue_cc1piselec.root`
  - `t2ksk19b.fqv4r0b.21bv2_run11.fhc.nue_x_nue_cc1piselec.root`
  - `t2ksk19b.fqv4r0b.21bv2_run11.fhc.numubar_x_numubar_cc1piselec.root`
  - `t2ksk19b.fqv4r0b.21bv2_run11.fhc.numubar_x_nuebar_cc1piselec.root`
  - `t2ksk19b.fqv4r0b.21bv2_run11.fhc.nuebar_x_nuebar_cc1piselec.root`

- FHC Multi-ring μ, `iclass` = $\{31, 32\}$:
  - `t2ksk19b.fqv4r0b.21bv2_run11.fhc.numu_x_numu_numucc1piselec.root`
  - `t2ksk19b.fqv4r0b.21bv2_run11.fhc.numu_x_nue_numucc1piselec.root`
  - `t2ksk19b.fqv4r0b.21bv2_run11.fhc.nue_x_nue_numucc1piselec.root`
  - `t2ksk19b.fqv4r0b.21bv2_run11.fhc.numubar_x_numubar_numucc1piselec.root`
  - `t2ksk19b.fqv4r0b.21bv2_run11.fhc.numubar_x_nuebar_numucc1piselec.root`
  - `t2ksk19b.fqv4r0b.21bv2_run11.fhc.nuebar_x_nuebar_numucc1piselec.root`

A.2 Momentum, Angle, and Energy Reconstruction for Minituples Run11

This appendix details the steps necessary for the computation of momentum, angle, and reconstructed energy for the Minituples Run11. Since calculations vary slightly across samples due to the parent neutrino and its interaction type, the procedure for each sample is outlined here.

A.2.1 Single-ring Events (iclass 11, 13, 14)

For single-ring events (interaction classes `iclass 11`, `13`, and `14`), the following variables from `fiTQun` are used to compute the reconstructed momentum and angle:

- `fq1rmom[0][particle_type]`: Provides the lepton momentum for a single-ring event.
- `fq1rdir[0][particle_type][3]`: Provides the lepton direction for a single-ring event.

The `particle_type` is equal to 1 for electrons and 2 for muons, therefore, the electron or muon momenta are:

- For electrons: `fq1rmom[0][1]`.
- For muons: `fq1rmom[0][2]`.

Similarly, the direction of the lepton for each particle type can be retrieved using `fq1rdir[0][particle_type]`.

A.2.2 Cosine of the Lepton Direction with Respect to the Neutrino Beam

The cosine of the lepton direction with respect to the neutrino beam direction can be calculated by taking the dot product of the lepton direction, `fq1rdir[0][particle_type]`, with the T2K beam direction vector:

$$\text{T2K Beam Direction} = \{0.669764, -0.742179, 0.024223\}$$

A.2.3 Energy Reconstruction

The momentum and cosine of the lepton direction are then used to compute the reconstructed neutrino energy.

- For `iclass 11` and `13`, the CCQE equation is used to calculate the reconstructed energy.
- For `iclass 14`, the Delta resonance approximation is employed.

A.2.4 Multi-ring Events (iclass 15, 31, 32)

For multi-ring events (interaction classes `iclass 15`, `31`, and `32`), you will need the `fiTQun` multi-ring variables as follows:

- `fqmrmom[fit_index][ith_ring]`: Provides the lepton momenta, assuming a particular multi-ring fit denoted by `fit_index` and assuming `ith_ring` is the lepton.
- `fqmrdir[fit_index][ith_ring][3]`: Provides the lepton direction, assuming a particular multi-ring fit denoted by `fit_index` and assuming `ith_ring` is the lepton.

OA2023 and OA2024 Minituples

- For `OA2023` minituples, `ipp` is used to tag multi-ring mu-like fits.
- For `OA2024` minituples, `iep` is used to tag multi-ring e-like fits.

Event Class Specific Calculations

In the case of multi-ring events, all three interaction classes (`iclass 15`, `31`, and `32`) utilize the Delta resonance equations for energy reconstruction.

iclass 15: For `iclass 15`, proceed by using the momentum and direction where `ith_ring == 0`, as we assume the first ring corresponds to the electron ring.

iclass 31 and 32: For `iclass 31` and `32`, the following procedure is used to identify the most energetic ring:

```
idx_mu = 0;
if (fqmrmom[ipp][0] < fqmrmom[ipp][1]) idx_mu = 1;
```

This selects the most energetic ring from the MRmu sample for kinematic calculations.

Visible Energy Variable

The variable `fqevis` provides the visible energy of the event, which can be used in further analyses.

A.2.5 True Variables

For the true event-level variables, the following variables provide the true neutrino energy, lepton momentum, and direction:

- `pnu[0]`: Provides the true neutrino energy.
- `pnu[LeptonIndex]`: Provides the true lepton momentum.
- `dirnu[LeptonIndex][3]`: Provides the true lepton direction.

Finding the Lepton Index

To identify the `LeptonIndex`, which is necessary to retrieve the true lepton information, the following code snippet can be used:

- `numnu`: Represents the total number of particles in the simulation.
- `ipnu[i]`: Provides the PDG code of the particle.

Neutrino Interaction Mode

The variable `mode` provides the true neutrino interaction mode, which can be used to classify the type of interaction (e.g., CCQE, resonance, DIS, etc.).

```
int LeptonIndex = -1;

for (int i=1;i<numnu;i++) {
    if ( (abs(ipnu[i])>=11) && (abs(ipnu[i])<=16) ) { //Check if
        outgoing lepton is electron/muon/tau
        if ( (abs(ipnu[0]) == abs(ipnu[i])) || (abs(ipnu[0]) ==
            abs(ipnu[i])+1) ) { //Check if outgoing lepton is same
            family as incoming neutrino
            if (ipnu[0]*ipnu[i] > 0) {//Check if outgoing outgoing
                lepton and incoming neutrinio are particle or
                antiparticle
                LeptonIndex = i;
                break;
            }
        }
    }
}

if (LeptonIndex == -1) {
    std::cout << "Lepton not found in following list - Quitting" <<
        std::endl;
    for (int i=1;i<numnu;i++) {
        std::cout << ipnu[i] << " ";
    }
    std::cout << std::endl;
    throw;
}
```

References

[1] M. Lubej. A pretty diagram of the standard model. [Online]. Available: https://www-f9.ijs.si/~lubej/

[2] Lancaster university particle physics package. [Online]. Available: http://lppp.lancs.ac.uk/neutrinos/en-GB/theory.html?LPPPSession=1566345600030

[3] M. Prado Rodriguez, "Neutrino mass ordering with icecube deepcore," *Physical Sciences Forum*, vol. 8, no. 1, 2023. [Online]. Available: https://www.mdpi.com/2673-9984/8/1/7

[4] K. Abe *et al.*, "The t2k experiment," *Nuclear Instruments and Methods in Physics Research Section A: Accelerators, Spectrometers, Detectors and Associated Equipment*, vol. 659, no. 1, pp. 106–135, 2011. [Online]. Available: https://www.sciencedirect.com/science/article/pii/S0168900211011910

[5] T. Koseki *et al.*, "Beam commissioning and operation of the J-PARC main ring synchrotron," *Progress of Theoretical and Experimental Physics*, vol. 2012, no. 1, p. 02B004, 12 2012. [Online]. Available: https://doi.org/10.1093/ptep/pts071

[6] *Accelerator technical design report for high-intensity proton accelerator facility project, J-PARC*, 2003. [Online]. Available: https://cds.cern.ch/record/747209

[7] K. Abe *et al.*, "Measurements of neutrino oscillation parameters from the t2k experiment using 3.6×10^{21} protons on target," *Eur. Phys. J. C*, vol. 83, p. 782, 2023. [Online]. Available: https://arxiv.org/pdf/2303.03222.pdf

[8] J. G. Walsh, "Constraining the t2k neutrino oscillation parameter results using data from the off-axis near detector, nd280," Ph.D. dissertation, Lancaster University, Lancaster, 2022.

[9] K. Abe *et al.*, "Improved constraints on neutrino mixing from the t2k experiment with $\mathbf{3.13 \times 10^{21}}$ protons on target," *Phys. Rev. D*, vol. 103, p. 112008, 2021. [Online]. Available: https://arxiv.org/pdf/2101.03779.pdf

[10] D. Carabadjac, "Fd samples binning optimisation," Presentation at the OA Meeting, December 2023, email: dcarabadjac@llr.in2p3.fr.

[11] Particle Data Group, "Summary tables: Leptons," 2024, accessed: 2024-09-12. [Online]. Available: https://pdg.lbl.gov/2024/tables/contents_tables.html

[12] K. Abe *et al.*, "T2k neutrino flux prediction," *Phys. Rev. D*, vol. 87, p. 012001, Jan 2013. [Online]. Available: https://link.aps.org/doi/10.1103/PhysRevD.87.012001

[13] W. Pauli, "Liebe radioaktive damen und herren," *Congrès des physiciens de Tübingen*, p. 4, 1930.

[14] P. Wolfgang, "Dear radioactive ladies and gentlemen," *Phys. Today*, vol. 31N9, p. 27, 1978.

[15] J. Chadwick, "Intensitätsverteilung im magnetischen Spectrum der β-Strahlen von radium B + C," *Verhandl. Dtsc. Phys. Ges.*, vol. 16, p. 383, 1914. [Online]. Available: https://cds.cern.ch/record/262756

[16] C. D. Ellis, W. A. Wooster, and E. Rutherford, "The average energy of disintegration of radium e," *Proceedings of the Royal Society of London. Series A, Containing Papers of a Mathematical and Physical Character*, vol. 117, no. 776, pp. 109–123, 1927. [Online]. Available: https://royalsocietypublishing.org/doi/abs/10.1098/rspa.1927.0168

[17] F. Reines and C. L. Cowan, "Detection of the free neutrino," *Phys. Rev.*, vol. 92, pp. 830–831, Nov 1953. [Online]. Available: https://link.aps.org/doi/10.1103/PhysRev.92.830

[18] G. Danby, J.-M. Gaillard, K. Goulianos, L. M. Lederman, N. Mistry, M. Schwartz, and J. Steinberger, "Observation of high-energy neutrino reactions and the existence of two kinds of neutrinos," *Phys. Rev. Lett.*, vol. 9, pp. 36–44, Jul 1962. [Online]. Available: https://link.aps.org/doi/10.1103/PhysRevLett.9.36

[19] M. Block, H. Burmeister, D. Cundy, B. Eiben, C. Franzinetti, J. Keren, R. Møllerud, G. Myatt, M. Nikolic, A. Orkin-Lecourtois, M. Paty, D. Perkins, C. Ramm, K. Schultze, H. Sletten, K. Soop, R. Stump, W. Venus, and H. Yoshiki, "Neutrino interactions in the cern heavy liquid bubble chamber," *Physics Letters*, vol. 12, no. 3, pp. 281–285, 1964. [Online]. Available: https://www.sciencedirect.com/science/article/pii/0031916364911047

[20] K. Kodama *et al.*, "Observation of tau neutrino interactions," *Physics Letters B*, vol. 504, no. 3, pp. 218–224, Apr. 2001. [Online]. Available: http://dx.doi.org/10.1016/S0370-2693(01)00307-0

[21] M. L. Perl *et al.*, "Evidence for Anomalous Lepton Production in e+ - e- Annihilation," *Phys. Rev. Lett.*, vol. 35, pp. 1489–1492, 1975.

[22] A. D. Sakharov, "Violation of CP Invariance, C asymmetry, and baryon asymmetry of the universe," *Pisma Zh. Eksp. Teor. Fiz.*, vol. 5, pp. 32–35, 1967.

[23] Y. Fukuda *et al.*, "Evidence for oscillation of atmospheric neutrinos," *Phys. Rev. Lett.*, vol. 81, pp. 1562–1567, Aug 1998. [Online]. Available: https://link.aps.org/doi/10.1103/PhysRevLett.81.1562

[24] S. Collaboration, "Direct evidence for neutrino flavor transformation from neutral-current interactions in the sudbury neutrino observatory," *Phys. Rev. Lett.*, vol. 89, p. 011301, Jun 2002. [Online]. Available: https://link.aps.org/doi/10.1103/PhysRevLett.89.011301

[25] K. Eguchi *et al.*, "First results from kamland: Evidence for reactor antineutrino disappearance," *Phys. Rev. Lett.*, vol. 90, p. 021802, Jan 2003. [Online]. Available: https://link.aps.org/doi/10.1103/PhysRevLett.90.021802

[26] M. H. Ahn *et al.*, "Measurement of neutrino oscillation by the k2k experiment," *Phys. Rev. D*, vol. 74, p. 072003, Oct 2006. [Online]. Available: https://link.aps.org/doi/10.1103/PhysRevD.74.072003

[27] P. Adamson *et al.*, "Combined analysis of ν_μ disappearance and $\nu_\mu \to \nu_e$ appearance in minos using accelerator and atmospheric neutrinos,"

Phys. Rev. Lett., vol. 112, p. 191801, May 2014. [Online]. Available: https://link.aps.org/doi/10.1103/PhysRevLett.112.191801

[28] K. Abe *et al.*, "Observation of electron neutrino appearance in a muon neutrino beam," *Phys. Rev. Lett.*, vol. 112, p. 061802, Feb 2014. [Online]. Available: https://link.aps.org/doi/10.1103/PhysRevLett.112.061802

[29] P. Adamson *et al.*, "First measurement of electron neutrino appearance in nova," *Phys. Rev. Lett.*, vol. 116, p. 151806, Apr 2016. [Online]. Available: https://link.aps.org/doi/10.1103/PhysRevLett.116.151806

[30] B. Pontecorvo, "Neutrino Experiments and the Problem of Conservation of Leptonic Charge," *Zh. Eksp. Teor. Fiz.*, vol. 53, pp. 1717–1725, 1967.

[31] Z. Maki, M. Nakagawa, and S. Sakata, "Remarks on the unified model of elementary particles," *Prog. Theor. Phys.*, vol. 28, pp. 870–880, 1962.

[32] T. Iwashita, T. Adachi, K. Takayama, K. W. Leo, T. Arai, Y. Arakida, M. Hashimoto, E. Kadokura, M. Kawai, T. Kawakubo, T. Kubo, K. Koyama, H. Nakanishi, K. Okazaki, K. Okamura, H. Someya, A. Takagi, A. Tokuchi, and M. Wake, "Kek digital accelerator," *Phys. Rev. ST Accel. Beams*, vol. 14, p. 071301, Jul 2011. [Online]. Available: https://link.aps.org/doi/10.1103/PhysRevSTAB.14.071301

[33] "Icrr - institute for cosmic ray research," accessed: 2024-10-06. [Online]. Available: https://www.icrr.u-tokyo.ac.jp/intro/intro_e.html

[34] M. Barranco Luque, M. Calvetti, L. Dumps, C. Girard, H. Hoffmann, G. Maurin, L. Naumann, J. Perez, G. Piano Mortari, A. Placci, P. Queru, M. Rijssenbeek, C. Rubbia, B. Sadoulet, and C. Tao, "The construction of the central detector for an experiment at the cern p-p collider," *Nuclear Instruments and Methods*, vol. 176, no. 1, pp. 175–180, 1980. [Online]. Available: https://www.sciencedirect.com/science/article/pii/0029554X80906990

[35] N. Abgrall *et al.*, "Measurements of differential yields from the surface of the t2k replica target for incoming 31 gev/c protons with the na61/shine spectrometer at the cern sps," *The European Physical Journal*

C, vol. 76, no. 617, 2016. [Online]. Available: https://doi.org/10.1140/epjc/s10052-016-4440-y

[36] A. Ferrari, P. R. Sala, M. /CERN /INFN, A. Fasso, /SLAC, J. Ranft, and S. U., "Fluka: A multi-particle transport code," 12 2005. [Online]. Available: https://www.osti.gov/biblio/877507

[37] K. Duffy, P. Dunne, L. Haegel, A. Kaboth, E. Pinzon, A. Sztuc, and C. Wret, "A joint nd280-sk 1rμ-sk 1re fit of neutrino and antineutrino-mode data using mcmc: A statistical update with run 1–9d sk data," December 2018, preprint.

[38] W. K. Hastings, "Monte Carlo sampling methods using Markov chains and their applications," *Biometrika*, vol. 57, no. 1, pp. 97–109, 04 1970. [Online]. Available: https://doi.org/10.1093/biomet/57.1.97

[39] ROOT Team, *ROOT: A Data Analysis Framework*, CERN, 1996–2024, version 6.28/02. [Online]. Available: https://root.cern/

Acknowledgments

The completion of this thesis marks the end of a challenging yet rewarding journey. First and foremost, I wish to express my deepest gratitude to my supervisor, Andrea Longhin, for his support, patience, kindness, expertise, and assistance throughout this process.

I am also deeply thankful to my friends, whose companionship and shared experiences have made these years truly memorable. Special thanks to Aidin, Alessandro, Andrea, Giuseppe, Lorenzo, and Samuele for the laughter, travels, and moments that have become an integral part of my university memories.

I am particularly grateful to my housemates: Amedeo and Francesco, who were always there whenever I needed help. My heartfelt thanks go to my sister, Ariana, for her constant support, as well as to Kitty, Anna and Beatrice, who, though not sisters by blood, feel just like family. I also want to thank Lorenzo for always being able to tolerate my erratic presence due to academic commitments, and Niccolò for being a steadfast friend over the years. To Calo, whose friendship, though recent, feels like it has always been there. And to my cat Lily, who kept me company day and night during the writing of this work, to whom it is dedicated.

Lastly, I want to express my gratitude to the city of Padova for welcoming me when I arrived feeling uncertain. I leave now, enriched by the opportunities and experiences it has offered me throughout these years, but over the most by the presence of the wonderful people mentioned here.